IU B International University Bremen

Molecular dynamics simulation of water near structured hydrophobic surfaces

by

Sandeep Pal

A thesis submitted in partial fulfilment

of the requirements for the degree of

Doctor of Philosophy

Approved, Thesis Committee

Prof. Dr. Florian Müller-Plathe
International University Bremen

Name and title of chair

Prof. Dr. Martin Zacharias
International University Bremen

Name and title of committee member

Prof. Dr. Kurt Kremer
Max Planck Institute for polymer Research

Name and title of committee member

Date of Defence: May 24, 2005

School of Engineering and Science

Abstract

The main focus of the thesis is to study the enhancement in the hydrophobicity of an already hydrophobic surface by creating surface structuring on the surface of the crystal. The local structuring and the free energy of interfacial water at the crystal/water interface is analysed by molecular dynamics simulation. An alkane crystal has been taken as the parent model for a hydrophobic surface. Surface structuring were created by either indenting pits on the surface of the crystal or by raising a protrusion on the surface of the crystal. Around all structures the water density was lower and the number of contacts between water and the surface of the crystal decreased due to surface structuring. The difference in the free energy of hydration between planar surface and the structured surface also revealed the increase in the hydrophobicity of the already hydrophobic crystal. Finally a study on the hydrophobicity of a perfluoro-n-alkane crystal is discussed in the final chapter. A qualitative comparison of the water structuring near an alkane and a perfluoro-n-alkane crystal show a higher htdrophobicity in case of a perfluoro-n-alkane crystal than an alkane crystal.

Contents

List of Tables

Chapter 1

Molecular dynamics simulation of water near structured hydrophobic surface

1 Introduction

The main focus of this thesis is to study the enhancement in the hydrophobicity of a hydrophobic surface by creating surface structuring on the surface of the crystal. A hydrophobic surface is nonwetting. A "super" hydrophobic surface is water repellent. Although the theory of surface wetting has been worked out since the nineteenth century, its details are still subject to intensive research today, the reason being the multifaceted nature of hydrophobic interactions. Macroscopically, the wettability of a material, with air and water as the surrounding media depends on the ratio of the interfacial tension between water/air, material/water and material/air. Interfacial tension or the surface tension is the reversible work required to change the surface area of the sample under consideration by unit surface area [1,2]. The ratio of the surface tensions determines the contact angle θ of a water droplet with the surface. Young's equation[1,2] quantitatively relates the surface tension to the contact angle

$$\cos\theta = (\gamma_{SV} - \gamma_{SL}) / \gamma_{LV},$$

where γ is the surface tension and S, L and V are the solid, liquid and vapour phases respectively. A contact angle of 0^0 indicates complete wetting, the water droplet spreading out into a liquid film on the surface. A contact angle of 180^0 means complete unwettability, the droplet making contact with the surface in only one point. Materials with a high interfacial tension γ_{SL} are more wettable than those with a low interfacial tension, such as teflon. A super-hydrophobic surface has very low interfacial tension with water [3-14].

1.1 Lotus effect

In order to see how structuring can increase the hydrophobicity of a surface, a view to the lotus effect is useful [3-10]. The sacred lotus flower is revered as a symbol of purity in Asian religions. Even emerging from muddy water it unfolds its leaves unblemished and untouched by pollution. The ability of these surfaces, Figure 1.1 and 1.2, to make water bead off completely and thereby wash off contamination very effectively has been termed the "Lotus effect", although it is observed not only on the leaves of the Lotus (Nelumbo nucifera) but also on many other species, such as Tropaeolum majus (Indian Cress/Nasturtium) or Alchemilla vulgaris (Lady's Mantle). Although this effect is very common among plants and is of great technological importance, as for example for the effective use of insecticides [3-10], its basic mechanisms is still under scrutiny. Since it is well known that plant surfaces are usually rough on the micrometer scale and covered with cuticular wax, many attempts have been made to manufacture industrially similar surfaces by introducing both hydrophobicity and roughness [11-14].

Barthlott and Neinhuis [3-5] collected experimental data by photographing the microstructure of rough water repellent leaves. Their seminal work revealed for the first time that the interdependence between surface roughness, reduced particle adhesion, and water repellence is necessary to understand the self-cleaning mechanism of many biological surfaces. In their experiments the plant leaves were artificially contaminated with various particles and subsequently subjected to artificial rinsing by sprinkler or fog generator. In the case of water repellent leaves, the particles were removed completely by water droplets that rolled off the surfaces, independent of their chemical nature or size.

Water repellent leaves exhibit various surface structures [14]. Of particular interest is the rough surface like that of the lotus leaf (Figure 1.3a). The fine scale rough structure (20 μm), visible as a "hairy" surface of the leaf, is made of epicuticular wax

crystals. The coarse scale rough structure (~2 μm) (Figure 1.3b) is visible as bigger protrusions on the surface. A water drop on lotus leaf type surfaces typically shows an apparent contact angle of about 160^0. The highest contact angle for water on smooth surfaces is 120^0 [15]. Beyond this angle, the fine surface roughness produced by a fractal structure can be a dominant factor in increasing the contact angle [15].

In the late 20^{th} century and the 21^{st} century there have been several theoretical and experimental groups (including physicists, chemists, biologists and mathematicians) have shown interest in this phenomenon. There have been several models proposed in the literature to understand the role of surface roughness/structuring on the superhydrophobcity. Interplay of chemistry (paraffinic surface), physics (surface roughness and structuring) and fine optimization of the chemistry and physics involved might be a solution to understand nature's super-hydrophobic phenomenon.

1.2 Enhancement of hydrophobicity by surface structuring

This section touches on the ongoing work on Lotus effect. Recently some of the theoretical and experimental studies were done in detail about the lotus effect. The problem of drop roll-off from the surface was dealt with a very simple theoretical model of the protrusions on a planar surface by Marmur [11]. According to Marmur et al. [11] two criteria define superhydrophobicity: a very high water contact angle (Figure 1.4a) and a very low roll-off angle, defined as the inclination angle at which a water drop rolls off the surface (Figure 1.4b). The wetting on rough surfaces was described by Marmur et al.[11] considering two regimes: homogeneous wetting (Figure 1.4c), where the liquid completely penetrates the roughness grooves, or heterogeneous wetting (Figure 1.4d), where air (or another fluid) is trapped underneath the liquid inside the roughness grooves. The transition between these regimes plays a major role in superhydrophobicity. The conditions for the existence of each regime was formulated by Marmur et al.[11], in terms of the geometrical features of the roughness. Marmur et al.[11] have claimed that the heterogenous

regime is practically preferred over homogenous regime as the superhydrophobic states on lotus leaves, for the reason that the contact area between the surface and the water is less in the case of heterogenous wetting than in the homogenous wetting case, leading to a lower surface tension and a higher contact angle between water droplet and the hydrophobic surface.

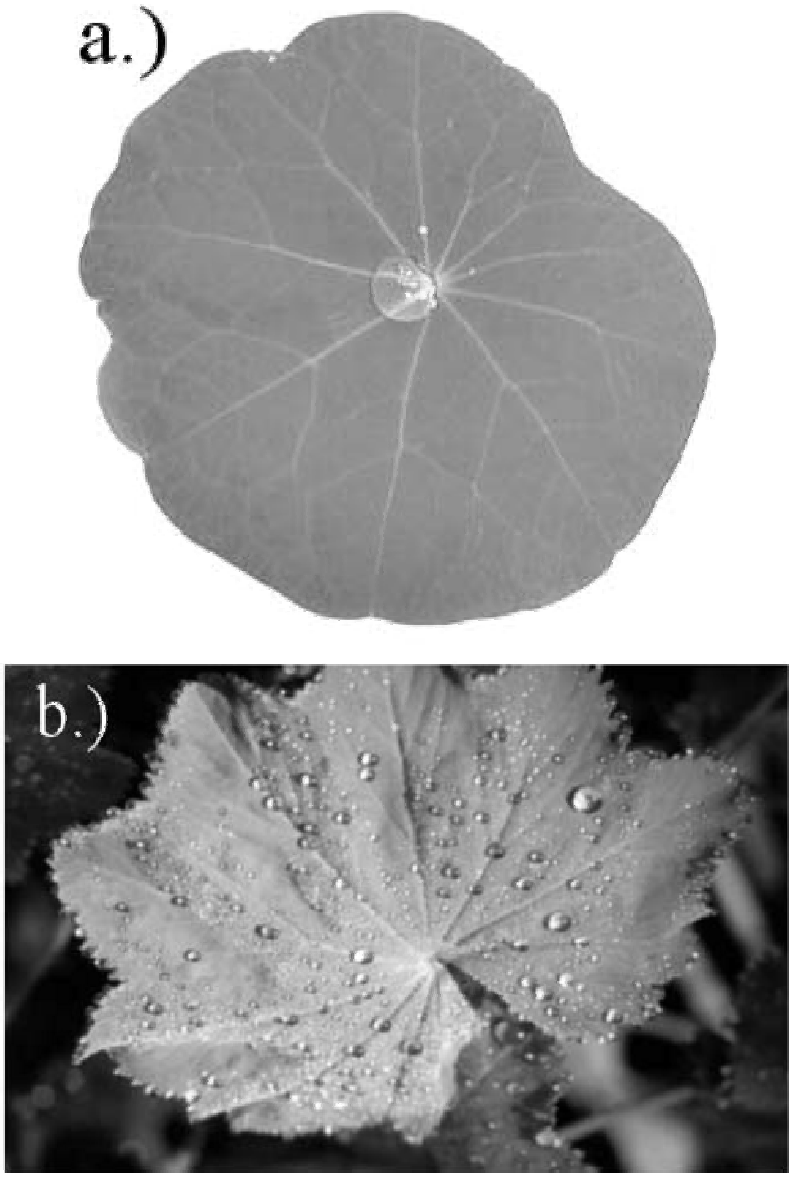

Figure 1.1 Water droplets on Indian Cress (a) and Lady's Mantle (b) [5].

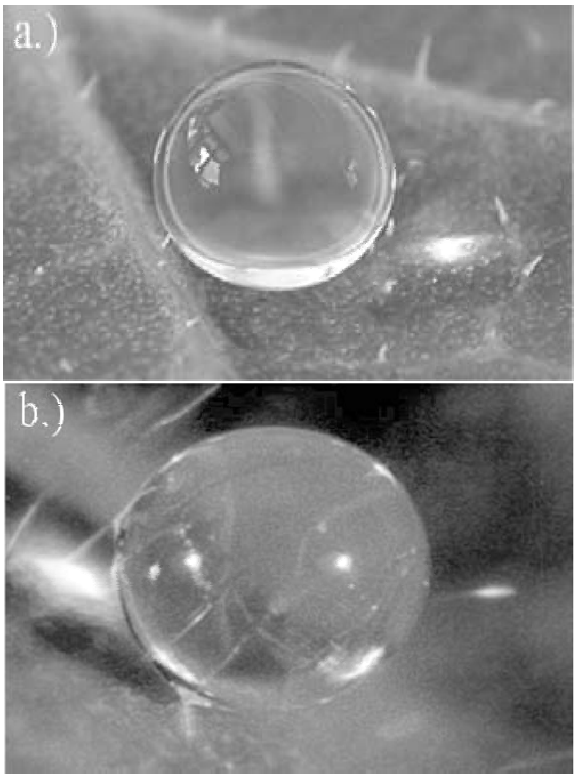

Figure 1.2 Water droplet on a lotus leaf [14]

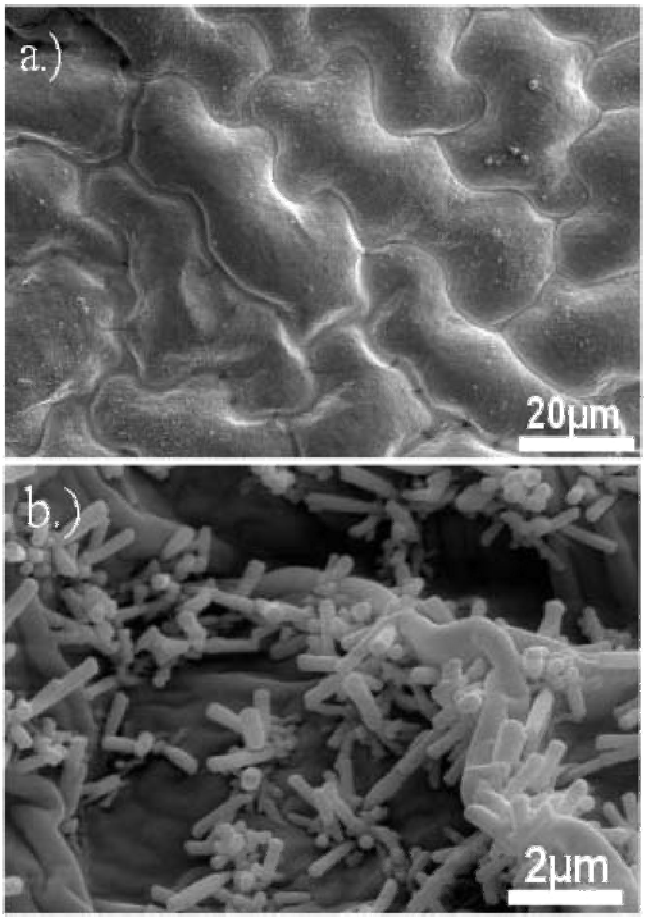

Figure 1.3 Microstructure on the lotus leaf [14].

An interesting explanation (theoretical and experimental) about "Lotus effect" was given by Otten et al [14]. Otten et al. have found experimentally that a dense brush of hydrophilic hairs can be effectively hydrophobic. They have performed the experiments on individual hairs of Lady's Mantle leaf. The contact angle, obtained by Otten et al. from the droplet meniscus at the hair, was found to be below 60^0 all along the hair, implying a hydrophilic hair. One expects a surface with a dense brush of hydrophilic hairs to be hydrophilic, with the liquid being sucked into the brush as into blotting paper. The small droplets nucleate on the ground (the cuticula of the leaf) with a contact angle well above 90^0, but as soon as they make contact with the hairs, they are lifted from the cuticula into the brush, stick to the hairs, as these are more hydrophilic than the cuticula, and are thus energetically preferred. The droplets sticking to the individual hairs coalesce when they get in contact with other droplets. Thus the water droplet is effectively supported on the tips of the fibres. This is an experimental evidence of heterogenous wetting.

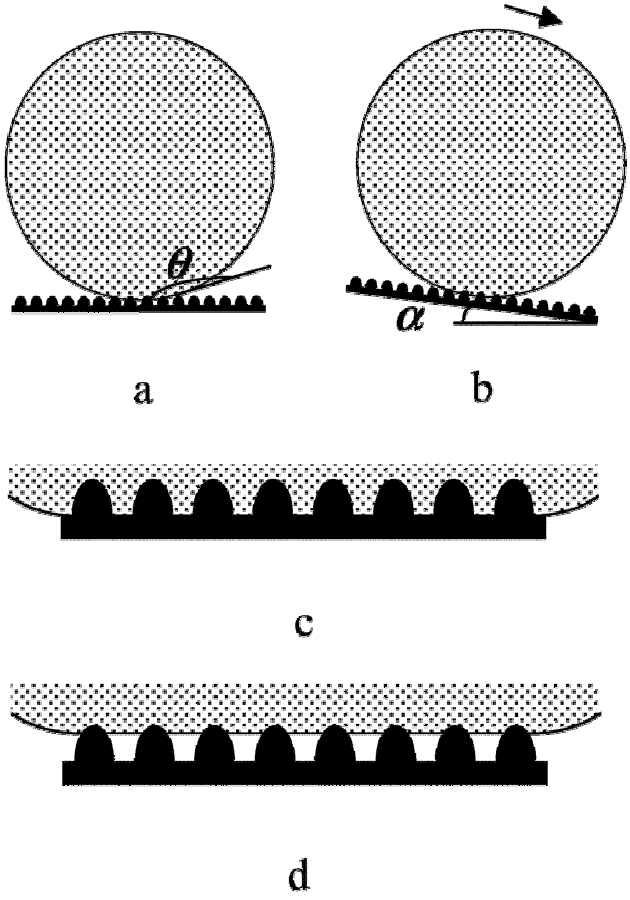

Figure 1.4 A drop on a rough surface: (a) the contact angle, θ (b) the roll-off angle, α (c) the homogeneous wetting regime; (d) the heterogeneous wetting regime [11].

To give a theoretical model for their experimental findings, Otten et al. [14] have described why a brush of hydrophilic hairs might be effectively hydrophobic, when a bundle of hairs stuck into a liquid-air interface are considered, Figure 1.5. The hydrophilic hairs had an elastic modulus. The article describes the condensation of hairs to individual bundles as the hairs meet the water-air interface. The interplay of the elastic energy of the hairs on the substrate surface and the water/water vapour surface tension were used as model parameters to depict the phenomenon of super-hydrophobicity. In essence the model shows that more the water/water vapour interface is near to the substrate, higher will be the bending energy of the elastic hairs resulting in the higher surface energy of the water/water vapour interface, as it will be corrugated. Thus in effect the water/water vapour interface is pushed away from the susbstrate.

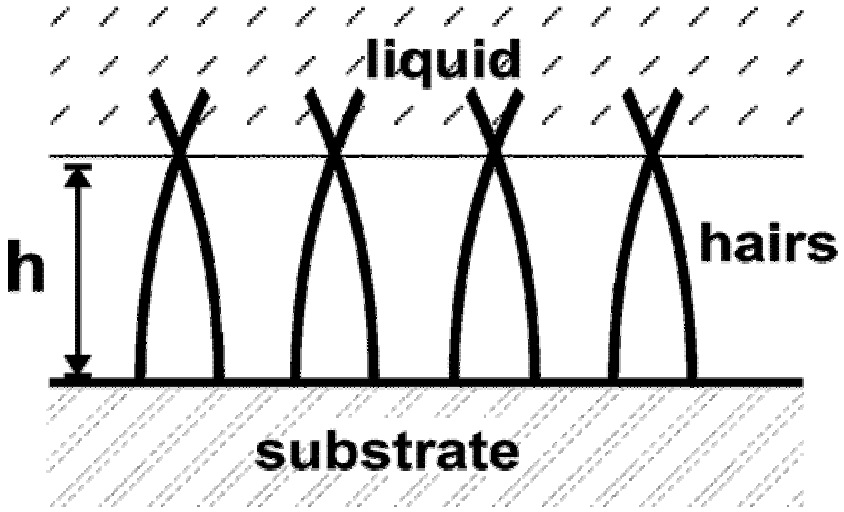

Figure 1.5 Model to describe super-hydrophobicity [14].

Although the lotus effect is of micrometer scale in nature, one of the important aims in this thesis is to see whether it can be repeated on a nanometer scale. This scale is

amenable to detailed investigations by molecular dynamics simulations. The hydrophobic surface in this thesis, as described in chapter 2, is made from atomistic alkane crystals. Alkane crystals are chemically similar to hydrophobic polymers or self assembled monolayers, which could be used to create technical surface coatings. At the same time, it is easy to construct different surface topographies with them. The results of the simulation are presented in chapter 2.

1.3 Effect of salts on the hydrophobicity of a hydrophobic crystal-water interface

The effect of alkali halide electrolytes at the water/water vapour interface is one of the very recent areas of research [16-18]. Molecular simulations [16-18] have challenged the traditional view [19] that there are no atomic ions at the air/solution interface of aqueous interface. The traditional view was based on measuring the enhancement of surface tension of water/water vapour interface on adding electrolytes. Surfactants or surface-active agents, which decrease the surface tension of the water/water vapour interface, are present at the interface of the water/water vapour. However based on this fact, it cannot be safely assumed that the enhancement on the surface tension of the water/water vapour interface necessarily means the absence of electrolytes from the interface. The traditional picture that the salts are depleted from the water/water vapour interface was based on the Gibbs adsorption equation [19].

It has been shown by the work of Jungwirth et al.[16-18], using molecular dynamics simulations of a series of sodium halide (NaF, NaCl, NaI, NaBr) solutions with water that an increase of surface tension does not necessarily imply negative adsorption (ions staying away from the interface) of ions. This is contrast to the traditional believe. In fact it was shown that, whereas the small, nonpolarizable fluoride anion is excluded from the interface, in accord with the traditional picture, all of the larger, polarizable halide anions are present at the interface, and bromide and iodide actually

exhibit surfactant activity (enhanced concentration at the interface relative to the bulk) without reducing the surface tension of the water/water vapour interface.

The presence of the heavier anions at the water/water vapour interface was also worth investigating for a water/hydrophobic surface interface. There exists a low water density region near the hydrophobic object, which is sometimes [20], considered like a thin film of vapour. The presence of the anions at the interface of the water/hydrophobic surface interface may also change the interfacial properties, like local water density and surface tension, near the water/hydrophobic surface interface. It has been found theoretically [20] and by molecular simulations of liquid alkane droplets in water that there is a low water density at the interface of water/hydrophobic object. To investigate whether the same effect can be achieved at the water/hydrophobic interface as was already investigated for water/water vapor interface; we have studied the behaviour of electrolytes at the water/hydrophobic surface interface by molecular dynamics simulations. We have found that, although the heavier iodide ions are present at the interface, the surface tension of the water/hydrophobic interface increases in accordance with the results of Jungwirth et al. Other interesting structural and dynamical properties of water and ions at the crystal/water interface are discussed in chapter 3.

1.4 Investigation of the water/perfluoro alkane interface

A hydrophobic surface can be produced mainly by two ways: One is to utilize a rough surface of materials. Fractal roughness [15] is reported to bring a contact angle of water of 160^0. Besides these physical methods, it is well known that fluorinated surfaces are effective for lowering the surface free energy. A variety of fluorine polymers, typically poly(tetrafluoroethylene) (PTFE), have been developed in many fields because of their high water and oil resistances, organic solvents resistance, and lubricity.

Nishino et al. [21] have studied the hydrophobicity of perfluoro-n-eicosane vapor deposited on glass surface by measuring the contact angles of water droplets. The

dynamic contact angle measurement of water on the surface of the fluorocarbon was found to have an advancing contact angle of 122^0 and a receding contact angle of 116^0, the average 119^0. The corresponding surface tension of the interface was calculated as 6.7 mJ/m^2, which was claimed by Nishino et al. [21] to be the lowest surface tension of any material with water. In chapter 5 the molecular dynamics simulation of water/perfluorinated crystal is presented. The direct calculation of surface tensions of the water/perfluorinated crystal is the best method to compare the hydrophobicity between an alkane crystal and perfluorinated alkane crystal, however we did not find surface tension of the crystal/water interface due to technical problems addressed in chapter 5. The pressure anisotropy method [2] to calculate the surface tension of liquid/gas and liquid/liquid interface cannot to applied to find the surface tension of solid/liquid interfaces because the pressure anisotropy in the solid is not only found at the interface but also inside the solid. In spite of this we have presented simple qualitative and quantitative arguments to show the difference in hydrophobicity between the alkane and perfluorinated alkane crystal.

1.5 Techniques and Methods

The computer simulations or computer experiments are done to study systems of interest to biologist, physicists and chemists alike. Molecular simulations, in a nutshell, are about solving the statistical mechanical equations by numerical techniques. The basic laws of nature are sometimes, if expressed in terms of equations, are too difficult to solve analytically. The motion of more than two interacting bodies is essentially unsolvable by pencil and paper. Computer simulations, as a tool, help us in this regard by solving the equations of motion of many particle systems over a time scale to give us information about the behaviour of a system.

Among the various types of computer simulations molecular simulations are used extensively to predict the thermodynamic properties of molecular systems. Computer

simulations provide a direct route from microscopic details in a system (for example the masses, charges and geometry) to the macroscopic properties for example structural parameters and transport properties. There are many kinds of molecular simulations, for example molecular dynamics simulation, Monte-Carlo simulation and Brownian dynamics simulations to name a few. There are some standard procedures and intelligent techniques, which constitute to form the art of computer simulations. The intelligent techniques primarily concern on reducing expensive calculations (with respect to CPU time) and only doing those calculations, which are essential to calculate the properties of a system. In the next section we deal with the basics of molecular simulations, which are in fact a backbone to all the molecular simulations.

1.5.1 Basics of interaction potentials (classical mechanics)

The Hamiltonian H of a system of N atoms/molecules is given as the sum of the kinetic and the potential energy functions. For representations we consider q_i as generalized coordinates and p_i as the momentum of each atom/molecule i. The following expressions, describe a classical system

$$\begin{aligned} q &= (q_1, q_2 ....., q_N) \\ p &= (p_1, p_2 ....., p_N) \\ H &= H(q,p) = \sum_i \frac{p_i^2}{2m_i} + V(q_i) \end{aligned} \qquad 1.1$$

The generalized coordinates q_i can be the Cartesian coordinates of atoms/molecules. In some cases the generalized coordinates for nonspherical atoms or molecules are the centre of mass and a set of orientation variables. The kinetic part of the Hamiltonian uses the particle masses and momenta of atom/molecule as parameters. The potential energy depends on the intermolecular interactions, which are position dependent. The intermolecular interactions are defined by various forcefields, designed to fit certain thermodynamic/transport properties of interest and are discussed in detail later. The

negative of the gradient of the potential energy $V(\mathbf{r})$ with respect to the Cartesian coordinates $\mathbf{r}_i$ equals the force $\mathbf{f}_i(\mathbf{r})$ acting on a particle i

$$\mathbf{f}_i(\mathbf{r}) = -\frac{\partial V(\mathbf{r})}{\partial \mathbf{r}_i}. \qquad 1.2$$

From Newton's classical equation of motion, the positions and time are related according to following equations

$$\mathbf{v}_i = \frac{\mathrm{d}\mathbf{r}_i}{\mathrm{d}t} \qquad \dot{\mathbf{v}}_i = \mathbf{a}_i = \frac{\mathrm{d}\mathbf{v}_i}{\mathrm{d}t}, \qquad 1.3$$

where $\mathbf{a}_i$ is the acceleration acting on the particle. Substituting equation 1.3 to equation 1.1 we obtain the following the following Newton's equation of motion

$$\mathbf{f}_i = m_i \mathbf{a}_i \qquad 1.4$$

Thus by calculating the potential energy function for a given function we can calculate the force on each atom/molecule inside the system.

The potential energy of a system is a sum of the intermolecular and the intra molecular contributions. To describe the two kind of interactions let us consider a molecular system, for example a system of n-alkanes. The interaction between atoms of different molecules of n-alkanes is the intermolecular interaction potential energy. The interaction within the atoms of a single molecule of n-alkane is called the intramolecular interaction energy. The intramolecular interaction energy is thus divided into bond angle energies, bond torsion energies, dihedral angle energy and the nonbonded interaction energy between atoms of a single molecule, torsion and dihedral interactions, Fig 1.6. In the next section we describe the various interactions.

1.5.2 Non Bonded Interaction (Intermolecular interactions)

The separation of force-fields into distinct mathematical terms in molecular simulations is done to satisfy computational convenience, although quantum mechanics is a better way to describe intermolecular interactions. Each site-site

interaction can be modelled using a Lennard-Jones potential and a Coulombic potential [22-25]. The nonbonded interactions or the site-site interactions have the following two contributions:

$$V_{\text{nonbonded}}(i,j) = V_{\text{Coulomb}}(i,j) + V_{\text{LJ}}(i,j) \qquad 1.5$$

$$\left.\begin{aligned} V_{\text{Coulomb}}(i,j) &= \frac{1}{4\pi\varepsilon_0}\frac{q_i q_j}{r_{ij}} \\ V_{\text{LJ}}(i,j) &= 4\varepsilon_{ij}\left(\left(\frac{\sigma_{ij}}{r_{ij}}\right)^{12} - \left(\frac{\sigma_{ij}}{r_{ij}}\right)^{6}\right) \end{aligned}\right\} \qquad 1.6$$

Where (partial) charges are q_i and q_j, ε_0 is the vacuum permittivity, the Lennard-Jones parameters are σ_{ij} (LJ-radius) and ε_{ij} (LJ-energy). The energy parameter ε_{ij} increases with atomic number and the σ_{ij} also increases down a group of the periodic table but decreases from left to right across a period with the increasing nuclear charge [23]. These values are a reasonable first guess to model inter atomic interactions and are more often than not made to fit general properties of liquids like heat of vaporization and density. In some cases the potentials are fitted to represent the correct transport properties of liquids. As a general recipe one should be extremely careful in considering nonbonded force field parameters while doing computer modelling of certain liquid mixtures. For the electrostatic part of the interaction in equation 1.6, one also needs to fit these charges to know properties of liquids. Once the interaction between the several sites is modelled we need computationally cheap methods (less CPU time), which gives correct structural (e.g density, heat of vaporization) and dynamical properties (e.g diffusion coefficient, viscosity) for the system under consideration. The number of interactions between N particles in a system with pairwise interactions is N^2, which is computationally expensive. To avoid the expensive calculation between all the particles a cutoff procedure is employed. Atoms or molecules, which are more than a certain cutoff distance, r_c, (usually 3 to 6 atomic diameters ~ 1.0 nm) are not considered for interactions. The interactions between a reference atom/molecule and all the neighbouring atoms/molecule with in this cutoff

distance are considered for interactions. This procedure is mathematically shown in the equations 1.7.

$$V_{\text{short-range}} = \begin{cases} V_{\text{LJ}}(r) - V_{\text{LJ}}(r_c) & r_{ij} \le r_c \\ 0 & r_{ij} > r_c \end{cases} \qquad 1.7$$

The shift $V_{\text{LJ}}(r_c)$ ensures that the energy vanishes at r_c. This algorithm is efficient and accurate, however completely ignoring the contribution of the interactions beyond a cutoff range is avoided. The two methods employed to deal with long range corrections, for the Lennard-Jones interactions, are the neighbour listing procedure and the long-range corrections. Verlet [23-24] suggested a technique for improving the speed of the program by maintaining a list of neighbours, at a distance of $r_c + \delta r$, of a particular atom/molecule which is updated at intervals. Between the updates of the neighbour list the molecular dynamics program does not check for interactions through all the molecules but only those appearing in the list.

If the intermolecular potential is not rigorously zero for $r \ge r_c$, the truncation of the intermolecular potential at r_c can result in systematic error in the total potential energy of the system. If the intermolecular interactions decay rapidly, for example in case of Lennard-Jones interactions, a correction for the systematic error is possible. For the case of Lennard-Jones interaction the long range correction is given by the following formula:

$$E_{Long\_range} = \frac{8}{3}\pi\rho\varepsilon\sigma^3\left[\frac{1}{3}\left(\frac{\sigma}{r_c}\right)^9 - \left(\frac{\sigma}{r_c}\right)^3\right] \qquad 1.8$$

where ρ is the number density of the liquid, ε is the well depth of the Lennard-Jones interaction and σ is the diameter of an atom or the molecule. The contribution for the long-range corrections can be as high as 10% of the total interactions, inside the cutoff range, at typical liquid densities ~ 0.8 g/cm^3. Thus this correction cannot be neglected. The long range correction in case of Lennard-Jones interaction turns out to be a very well defined formula because the Lennard-Jones interactions decay as r^{-12} ,

Any interaction which decays as r^{-n} where n > 3 can be analytically solved to provide the long range interaction. The Coulombic interaction decays as r^{-1}, thus there is no simple analytical expression possible for this case. A Coulombic interaction is long range and it decays over many simulation box lengths. The expression is shown below in equation 1.9.

$$E_{\text{Coulomb}} = \frac{1}{2}\sum_{i,j=1}^{N}\sum_{\mathbf{n}}\frac{q_i q_j}{\left|\mathbf{r}_{ij} + \mathbf{n}L\right|} \qquad 1.9$$

where **n** is the number of boxes and L is the box length. In this case a cutoff procedure would give an interaction energy, which can significantly differ from the real interaction energy. There are several methods available to deal with the long ranged Coulombic interaction [23-24]. The YASP simulation package [22] employs one of the several methods, the reaction field method, to calculate the long-range correction. Reaction field method is also a cutoff based method, however the long-range corrections are calculated in a different way.

The reaction field method [22-23] assumes a dielectric continuum outside the cutoff-sphere. Its dielectric constant (ε_{RF}) is an input parameter and has to be taken from experiment. The reaction field method comprises two contributions to the electrostatic energy: The interactions within the cutoff distance and the contribution outside the cutoff distance. All interactions within the cutoff sphere are calculated directly (as in case of the Lennard-Jones interaction), however, outside the cutoff a contribution due to the polarization energy has to be calculated. The final interaction for the electrostatic potential is given by

$$V_q(r_{ij}) = \frac{q_i q_j}{4\pi\varepsilon\varepsilon_0}\left(\frac{1}{r_{ij}} + \frac{\varepsilon_{\text{RF}} - 1}{2\varepsilon_{\text{RF}} + 1}\frac{r_{ij}^2}{r_{\text{C}}^3}\right) \qquad 1.10$$

where ε is the dielectric constant of a medium and ε_0 is the permittivity of vacuum. The implementation of these equations into a molecular dynamics program is straightforward and computationally cheap [22-23]. The effect of the reaction field is that the force is zero at the cutoff distance for infinite ε_{RF}, as can be shown by

differentiation of equation 1.10. This physically means that the presence of high dielectric constant screens the long-range interactions effectively. The reaction field technique works well with water simulations owing to the high dielectric constant of water, ε_{RF} = 78. Since we study hydrophobic effect and dealing primarily with structure and dynamic properties of water, the reaction field technique is a good approximation to calculate the long-range interactions. However, sometimes it is difficult to choose a value of dielectric constant while dealing with a multi-component system.

Thus the reaction field is a practical approach to deal with long range electrostatic. The advantages of this method over other long range methods [23] are mainly in saving CPU, time however one should be extremely careful while dealing with systems having small dielectric constant (ε_{RF} ~ 1-5) and one should take up more sophisticated methods like Particle mesh Ewald summation [23-24].

1.5.3 Bonded interaction (intra molecular interactions)

Molecular systems not only have interactions between different atoms of different molecules, they also have interactions between different atoms of the same molecule. The atoms of a molecule can have vibrations (between bonded atoms), angle bending and also twisting of bonds. Figure 1.6.

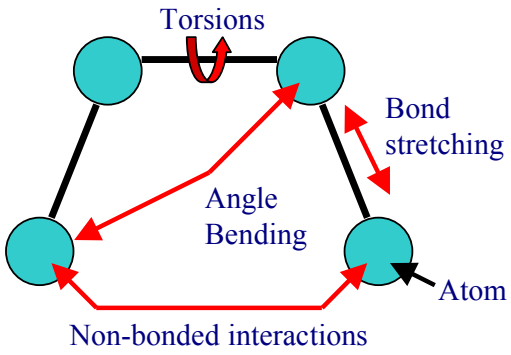

Figure 1.6 Intra molecular interactions

In principle, the bond vibrations and the angle vibrations are of harmonic characters. However, the bond vibrations have a very high frequency, which would mean that the time step chosen for our simulations have to extremely slow. Therefore the harmonic bond potentials is replaced with a rigid constraint bond, which on one hand introduces additional calculations into the molecular dynamics simulations, however allowing us to use bigger integrator's time step Δt [26]. The recipe to perform these calculations is discussed in the next section under constraint dynamics.

1.5.4 Constraint Dynamics

The constraint dynamics is handled by SHAKE algorithm [26]. A very comprehensive treatment of the algorithm can be found in the references 22-26. In constraint dynamics the equations of motion are solved while simultaneously satisfying the imposed constraints (e.g bond constraints). This method allows us to connect different atoms in the molecules without using harmonic bonds allowing us to use larger time steps (e.g. from 1 fs to 2 fs). Considering two atoms bonded to each other with a fixed distance, *a.* The equality is usually written down in the form of a holonomic constraint:

$$r_k^2 - a_k^2 = 0. \qquad 1.11$$

In a constrained system the coordinates of the particles are not independent and the equations of motion in each of the coordinate directions are related. The constraint forces lie along the bond in all times. For each constrained bond, there is an equal and opposite force on the two atoms that comprise the bond and therefore no energy being input in the system. Using SHAKE algorithm the true equation of motion is modified and a term, due to constraint forces, adds up to the total force described in equation 1.4.

$$\mathbf{f}_i + \mathbf{g}_i = m_i \mathbf{a}_i$$

where $\mathbf{g}_i$ is the constraint force. The equation of motion, of an atom, (described in the section 1.5.6) is also modified due to this correction and is given by

$$\mathbf{r}_i(t+\Delta t) = \mathbf{r}_i^{/}(t+\Delta t) + (\Delta t^2 / m_a)\mathbf{g}_i(t)$$

where $\mathbf{r}_i(t+\Delta t)$ and $\mathbf{r}_i^{/}(t+\Delta t)$ are the corrected coordinate by the bond constraints, and uncorrected coordinate of an atom. Satisfying one constraint may cause another constraint to be violated, therefore it is necessary to be iterate around the constraints until they are all satisfied to with in some tolerance. YASP uses a special flavor of SHAKE called as the multi color SHAKE or SHAVE algorithm. This algorithm performs very efficiently in vector machines.

1.5.5 Periodic boundary conditions

To study a bulk system or an infinite system with no walls one needs special techniques. The one and the only method used in molecular simulations are the periodic boundary conditions. The cubic simulation box is replicated in all the space to form an infinite lattice. During the simulation when a molecule goes out of the simulation box, its image enters the simulation box from the opposite side of the box, thus keeping the density in the box constant during the simulations. The simulation box simply forms a convenient axis system for measuring the coordinates of the *N* molecules. However, care has to be taken to take the cut off radius of an atom less than or equal to the reference atom so that the reference atom does not interact with its own periodic image. A very good pictorial description of the method can be found in the book by Allen and Tildesley [23].

1.5.6 Equation of Motion and Integrator

The motion of the atoms due to the forces acting on them follows by Newton's equation of motions. The integration of Newton's equations of motion is done

numerically and there several methods available, which vary according to the degree of accuracy [23-25]. YASP [22] uses leap-frog algorithm and is discussed here. The leap-frog method calculates velocities and positions with a shift of one half of a time step Δt :

$$\left.\begin{aligned}\mathbf{v}_i\left(t_n+\frac{1}{2}\Delta t\right)&=\mathbf{v}_i\left(t_n-\frac{1}{2}\Delta t\right)+\Delta t\frac{\mathbf{f}_i(t_n)}{m_i}+\mathrm{O}(\Delta t^3)\\ \mathbf{r}_i(t_n+\Delta t)&=\mathbf{r}_i+\mathbf{v}_i\left(t_n+\frac{1}{2}\Delta t\right)\Delta t+\mathrm{O}(\Delta t^4)\end{aligned}\right\} \quad 1.12$$

Here $\mathbf{r}_i$, $\mathbf{v}_i$ and $\mathbf{f}_i$ are position, velocities and force of one particle. The positions are accurate to an order of $\mathrm{O}(\Delta t^3)$ of the simulation time-step.

1.5.7 Pressure and temperature coupling

The best way to perform equilibrium molecular dynamics simulation would be to work in a constant energy ensemble (*NVE*) because this ensemble makes sure that the energy of the system is constant and there are no external forces acting in the system. However, molecular simulations are done to simulate real laboratory experiments. In laboratory conditions it is easier to control the temperature and pressure rather than the energy and the volume of the system. Therefore in molecular dynamics simulations one needs to implement a thermostat and a barostat. The thermodynamic variables temperature T from equation 1.13 and pressure p are calculated often at regular time intervals by molecular dynamic simulation. For determining the temperature, one must sum up the kinetic energy of all atoms/molecules divided by the number of degrees of freedom (equipartition theorem [22-23]):

$$T=\left\langle\frac{1}{3Nk}\sum_i^N m_i v_i^2\right\rangle, \quad 1.13$$

Where N is the number of sites, k the Boltzmann constant and the angle brackets $\langle\rangle$ denote ensemble averaging.

For the pressure p , two terms –A and B – contribute to the pressure:

$$p = \frac{1}{3V}\left(\underbrace{\left\langle \sum_i^N m_i v_i^2 \right\rangle}_{\text{Ideal part}} + \underbrace{\left\langle \sum_i^N \mathbf{f}_i \mathbf{r}_i \right\rangle}_{\text{Virial part}} \right) \qquad 1.14$$

where $\mathbf{f}_i$ is the total force acting on an atom or molecule and $\mathbf{r}_i$ is its position vector. The virial part extends over all site-site interactions. This virial part due to interatomic interactions, is the addition to the pressure over the ideal gas pressure.

$$p = \frac{NkT}{V} + \frac{\langle W \rangle}{V} \qquad 1.15$$

The virial part of equation 1.14 can also be transformed into pair interaction, $\sum_{i<j} \mathbf{r}_{ij}\mathbf{f}_{ij}$.

This treatment is better since it eliminates the unnecessary calculation of the total force on an atom. A very comprehensive treatment can be found in the book by Allen and Tildesley [23].

The temperature coupling is done by Berendsen weak coupling method [22] This method rescales particle velocities by a factor, s_T, to bring the temperature from the actual temperature T from equation 1.13 , to the set temperature T_0

$$s_T = \left(1 + \frac{\Delta t}{\tau_T}\left(\frac{T_0}{T} - 1 \right) \right)^{\frac{1}{2}} \qquad 1.16$$

The parameter τ_T (the relaxation time constant) is chosen significantly larger (~10 times) than the integration time step. If the time constant τ_T is chosen exactly equal to the integration time constant, then we would brute force the system to the fixed temperature causing a mistake in the dynamics. A time constant smaller than the integration time constant would make equation 1.16 imaginary. The Berendsen algorithm conserves total momentum and not total energy.

The pressure is controlled using an equivalent of equation 1.16, where the position vectors of particles and the box dimensions are scaled rather than particle velocities. We use isotropic scaling of the pressure p to target set pressure p_0:

$$s_p = \left(1 + \frac{\Delta t \kappa_p}{\tau_p}(p - p_0)\right)^{\frac{1}{3}} \qquad 1.17$$

Where τ_P as the pressure coupling constant and κ_p the system's compressibility, which is an experimental, input parameter. YASP [22] uses this temperature and the pressure coupling schemes to control the temperature and pressure of a simulation box.

1.5.8 Radial Distribution Functions

The structure of simple liquids is often described by the radial distribution functions *g(r)*. This function gives the probability of finding a pair of atoms at distance *r* apart, relative to the probability expected for a completely random distribution at the same density. The mathematical expression for the radial distribution function, considering *a* as the reference particle and *b* as another particle in the vicinity of *a*, is given in equation 1.19. The equation is defined as a Kronecker delta function where $\delta(r\text{-}r_{ij}) = 1$ if $r\text{-}r_{ij} = 0$ and vice versa.

$$g_{ab}(r) = \left\langle \frac{1}{N_a} \sum_{i=1}^{N_a} \frac{1}{4\pi r^2 \rho_b} \sum_{j=1}^{N_b} \delta(r - r_{ij}) \right\rangle \qquad 1.18$$

Where ρ_b is the particle density $< N/V >$ of particle *b*. The integral of *g(r)* over *r* defines the total number of neighbouring particles *b* surrounding *a* at certain distance r':

$$n_{ab}(r^{/}) = \rho_b \int_0^{r^{/}} g(r) dV \qquad 1.19$$

Where dV is the integration over a spherical volume with radius $r^{/}$ around a particle. The Fourier transform of the radial distribution function gives the structure factor of a liquid *S(k)* which can be found by Neutron scaterring experiments.

References

(1) Adamson, A. W. Physical Chemistry of Surfaces. London, Wiley, 1990.

(2) Israelachvili, J. N. *Intermolecular and surface forces*. Academic Press, San Diego, **1991**.

(3) Neinhuis, C.; Barthlott, W. *Annals of Botany.* **1997**, *79*, 667.

(4) Baker, E. A.; Parsons, E. *Journal of Microscopy.* **1971,** *9*4, 39.

(5) Barthlott, W. In: Claughter D, ed. *Scanning electron microscopy in taxonomy and functional morphology* Oxford: Clarendron Press, **1990**, 69.

(6) Baker, E. A.; Parsons, E. *Journal of Microscopy.* **1971,** 94, 31.

(7) Cassie, A. B. D.; Baxter, S. *Trans of Faraday Society.* **1944**, 40, 546.

(8) Adam, N. K.; In: Moilliet JL, ed. *Waterproofing and water-repellency*; **1963**, Elsevier, Amsterdam, 1.

(9) Linsken, H. F. *Planta.* **1950,** 38 , 591.

(10) Rentshler, I . *Planta.* **1971,** *96*, 119.

(11) Marmur, A. *Langmuir* **(Communication)**. **2004**, *20(9)*, 3517

(12) Wenzel, R.N. *Ind. Eng. Chem*. **1936**, 28, 988.

(13) Krupenkin, T. N.; Taylor, J. A.; Schneider, T. M.; Yang, S. *Langmuir* **(Communication). 2004,** *20(10),* 3824.

(14) Otten, A.; Herminghaus, S; *Langmuir* **(Communication). 2004**, *20(6)*, 2405.

(15) Hozumi, A.; Takai, O. Thin Solid Films 1997, 203, 222-225

(16) Jungwirth, P.; Tobias, D. J. *J. Phys. Chem. B* **2001**, *105*, 10468.

(17) Jungwirth, P.; Tobias, D. J. *J. Phys. Chem. B* **2002**, *106*, 6361.

(18) Tobias, D. J.; Jungwirth, P.; Parrinello, M. *J. Phys. Chem*. **2001**, *114*, 7036.

(19) Chattoraj, D. K.; Birdi, K. S. Adsorption and the Gibbs Surface Excess; Plenum: New York, **1984**.

(20) Huang, D. M.; Chandler, D. *J. Phys. Chem*. B **2002**, *106*, 2047.

(21) Nishino, T.; Meguro, M.; Nakamae, K.; Matsushita, M.; Ueda, Y. *Langmuir* **1999**, *15*, 4321.

(22) Müller-Plathe. F. *Comput. Phys. Commun*. **1993,** *78*, 77

(23) Allen, M. P.; Tildesly, D. J. *Computer simulation of liquids*; Clarendron Press: Oxford, **1987**.

(24) Frenkel, D.; Smit, B. *Understanding Molecular Simulation*; Academic Press, San Diego, **2002**.

(25) Jensen, F.; *Introduction to Computational Chemistry*, Wiley VCH, Chichester, **1998**.

(26) Ryckaert, J. P.; Ciccotti, G.; Berendsen, H. J. C. *J. Comp. Phys*. **1971**, *23*, 237.

Chapter 2

Effect of nano-structure on the properties of water at water-hydrophobic interface, a molecular dynamics simulation

ABSTRACT

The local structure of water near hydrophobic surfaces of different surface topographies has been analysed by molecular dynamics simulation. An alkane crystal has been taken as the parent model for a hydrophobic surface. Surface structures were created by placing pits into it, which were half a nanometer deep and several nanometers wide. Around all structures, the water has a lower density, less orientational ordering, fewer water-water hydrogen bonds, and fewer surface contacts than for a flat unstructured surface. This indicates that the structured surfaces are more hydrophobic than the flat surface. Of the structures investigated, pits with a diameter of approximately 2.5 nm were effective in increasing the hydrophobic character of the surface.

2.1. INTRODUCTION

A hydrophobic surface is nonwetting. A "super" hydrophobic surface is water repellent. Although the theory of surface wetting has been worked out since the nineteenth century, its details are still subject to intensive research today, the reason being the multifaceted nature of hydrophobic interactions. Macroscopically, the wettability of a material, with air and water as the surrounding media depends on the ratio of the interfacial tension between water/air, material/water and material/air. The ratio of the surface tensions determines the contact angle θ of a water droplet with the surface. Young's equation[1,2] quantitatively relates the surface tension to the contact angle

---

Pal, S.; Weiss, H.; Keller, H.; Muller-Plathe, F.;
Langmuir; **(Article); 2005**; *21*(8); 3699-3709

$$\cos \theta = (\gamma_{SV} - \gamma_{SL}) / \gamma_{LV},$$

where γ is the surface tension and S, L and V are the solid, liquid and vapour phases respectively. A contact angle of 0° indicates complete wetting, the water droplet spreading out into a liquid film on the surface. A contact angle of 180° means complete unwettability, the droplet making contact with the surface in only one point. Materials with a high interfacial tension γ_{SL} are more wettable than those with a low interfacial tension, such as teflon. A superhydrophobic surface has very small interfacial tension with water.

In order to see how the hydrophobicity of a surface can be increased by structuring it, a view to the lotus effect is useful.[3-8] Although the lotus flower grows in muddy areas, it always stands clean because the water on the surface of the lotus leaves is very unstable and rolling off it takes any dirt with it. This phenomenon is used by many plant leaves. Their superhydrophobicity has been studied in detail in the past ten years. Reduced wettability as a macroscopic effect caused by epicuticular waxes was recognized very early, but described only in general terms until the work of Cassie and Baxter[7] described the physical fundamentals of water repellency. The surface of the lotus leaf is covered by epicuticular wax crystals[9,10]. Additionally, the surface of the lotus leaf is structured on a micrometer length scale. While the wettability of *hydrophilic* surface would even be improved by roughening, a *hydrophobic* material is made superhydrophobic by microstructuring. As the water drop rests only on the tips of the peaked microstructures, the contact area between leaf and droplet is minimized. If technical surfaces could be microstructured in this way, they would also be cleansed by rain.

Although the lotus effect is of micrometer scale in nature, our aim is to see whether it can be repeated on a nanometer scale. This scale is amenable to detailed investigations by molecular dynamics simulations. In this contribution, we report molecular dynamics simulations studying the effect of surface structure on the static properties of interfacial water. Two main questions are of interest: Firstly, can the hydrophobicity and its dependence on the topography of the hydrophobic surface be

understood by considering simple interaction models between water and the hydrophobic material? Secondly, what is the length scale of the topography, which most influences the water near the hydrophobic interface? The hydrophobic surface of this work is made from atomistic alkane crystals. Alkane crystals are chemically similar to hydrophobic polymers or self assembled monolayers, which could be used to create technical surface coatings. At the same time, it is easy to construct different surface topographies with them. Note, however, that the alkane crystals are being used as a convenient model of a paraffinic surface. The work is limited to studying the water structure near the interface and results derived from it. It does not attempt to calculate the interfacial tension. There exist simulation and theoretical approaches for finding the free energy between water and a hydrophobic material interface. [11-18] They are, however, in the present form suitable only for interfaces between two isotropic phases (vacuum, fluid, structureless walls) and not for crystals[12]. The work done by the group of Chandler[11] is based on placing an unstructured repulsive or attractive sphere in the water and inflating it in a thermodynamic integration. Such a sphere can approximate a droplet of a liquid alkane, but not a crystal. Another thermodynamic-integration based method[12] is very specific to the interfacial tension of the crystal melt interface of the Lennard-Jones liquid. Cottin-Bizonne et al. have performed molecular dynamics simulation of LJ liquid confined between two corrugated repulsive surface.[19] The article reports a dewetting transition, leading to a super-repulsive state for pressures below capillary pressure for such hydrophobic surfaces. A very large slippage of the fluid at the interface was found in the superrepulsive state. While we are working on thermodynamic-integration methods for anisotropic surfaces, we study the structure (density, orientation, surface contacts) of water around hydrophobic surfaces of different topography as a first step towards understanding the influence of nanostructures on the hydrophobicity of a surface.

2.2 COMPUTATIONAL DETAILS

2.2.1 Details of the surface structure

A crystal of n-eicosane molecules ($C_{20}H_{42}$) (one layer of 7×12 molecules) serves as the model of our hydrophobic surface. Crystallography of n-eicosane shows that it has a triclinic crystal structure.[20-22] We used an idealized model surface for the n-eicosane crystal with no defects, Figure 2.1. Instead of non-bonded interactions between alkane molecules, harmonic distance restraints with a force constant k = 2000 kJ mol^{-1} $Å^{-2}$ were used between adjacent carbons of any chain and carbons of its six nearest neighbours taking into account periodic boundary conditions. More specifically, springs were used between carbons of the same index (i.e. C_i - $C_i^{/}$, length: 0.497 nm) and carbon one index apart (C_i - $C_{i+1}^{/}$, length: 0.89 nm). These lengths were chosen to maintain the crystal structure of n-eicosane[20-22] in constant pressure simulations. This rigidification was necessary not so much for the native planar alkane slab, but to prevent surface reconstruction of structured alkane surfaces, which contained also shorter alkane chains. Figure 2.2 shows how a structured surface can be generated from the $C_{20}H_{42}$ crystal by shortening selected chains. Several surface topographies were created in this way: big hexagonal hole (19 alkane chains shortenened by four carbons), stripes (7×2 chains shortened), hexagonal hole (7 alkane chains shortened), triangular holes (3 alkane chains shortened) and the present planar crystal, Figure. 2.3 and 2.4. Measuring between carbon chain positions flanking the holes, the big hexagonal hole has a diameter of approximately 2.5 nm, the hexagonal hole 1.75 nm, the triangular hole 1 nm, the stripes are infinitely long and have a width of approximately 1.2 nm. To convert to the inner widths, the diameter of a CH_3 group should be subtracted from these values. The total surface areas of the holes are approximately 3.8 nm^2 (1 big hexagonal hole), 2.7 nm^2 (2 hexagonal holes), 1.9 nm^2 (3 triangular holes) and 5.6 nm^2 (2 stripes). With the surface area of the crystal of $3.3 \times 5.3\,\mathrm{nm}$, we therefore have a percentage of indented surface of 21.8% (big hexagonal hole), 16.1% (hexagonal), 10.6% (triangular), 31.9% (stripes). In order to increase sampling, on both the upper and lower crystal surface indentations were used simultaneously, well separated from one another: 2 nm (hexagonal holes), 1.8 nm (triangular holes), 2 nm (stripes), only one big hexagonal hole is present per side, and

the one on the opposite sides is offset 2 nm in the y direction and 1 nm in the x direction (cf. Figure. 2.2). More complicated geometries would be possible by a mixture of these basic shapes. The different holes have different number of edges on the sides and, therefore, different edge-length-to-area ratios. These have an influence on the behaviour of water, as will be discussed.

2.2.2 Simulation model

Our periodic simulation box ($3.3 \times 5.3 \times 5.1\,\mathrm{nm}^3$) contained 1500 molecules of water and 84 n-eicosane molecules. The crystal was placed at the centre of the box as shown in Figure. 2.2. The crystal structure is triclinic ($\alpha = 67.6^0, \beta = 83.9^0, \mathrm{c} = 2.544\,\mathrm{nm}$) and close to the experimental crystal ($\alpha = 68.2^0, \beta = 85.7^0, \mathrm{c} = 2.743\,\mathrm{nm}$). The difference in c comes from c being the slab thickness (simulation) and unit cell length (experiment). The eicosane crystal (thickness 2.5 nm) was separated from its periodic image by a water layer (thickness 2.6 nm). We have verified that this thickness is enough for the water to reach bulk behaviour (density and orientational disorder) between the two surfaces in accordance with the earlier simulations.[23] The crystal plane was the xy plane with the inclination of the molecular axes in y direction. In all analyses, z = 0 refers to the surface of the planar crystal defined by the arithmetic mean of the z coordinates of all the unindented surface carbons, so all indentations carry a negative z (Fig. 2.5).

We used the YASP simulation package.[24] The system was weakly coupled to the desired temperature (298 K and 378 K) with a relaxation time of 0.2 ps.[25-27]. The Cartesian diagonal components of the pressure tensor were coupled separately to an external pressure of 0.1013 MPa with a relaxation time of 0.5 ps.[25-27] Since the alkane crystal is very stiff in the x and y directions, relaxations of the density took place practically exclusively by box length changes in the z direction. Bond lengths were constrained using the SHAKE algorithm.[29] The time step for the leapfrog integration scheme[25-26] was set to 0.002 ps and the trajectory frames were written to disk every 1

ps. Non-bonded interactions were evaluated at every time step with a cutoff radius of 0.9 nm using a neighbour list (update every 20 steps, neighbour list cutoff 1.0 nm). The simulations typically consist of 1 ns of equilibration and 1 ns of data collection. The topographies on the surface of the crystal were made by switching off the interactions between the first four carbons (depth ~ 0.5 nm) and the hydrogens connected to them and water. The n-eicosane is described by the all-atom OPLS model[30-31]. The OPLS-AA model has been chosen because it produces realistic interactions with the SPC/E[32] water model: As a test, we have calculated the free energy of hydration for octane (-9.2 kJ/mol, experimental -9.87 kJ/mol). Water is treated with the SPC/E model.[32] Lennard-Jones parameters for interactions between unlike atoms were evaluated using the Lorentz-Berthelot mixing rules,[25] electrostatic interactions were treated with the reaction field approximation,[25] using an effective dielectric constant of 72.

2.2.3 Analysis

The simulations were analysed in terms of the density of water at and near the interface. We have analysed the local densities by dividing the simulation box into cells ($0.4 \times 0.4 \times 0.2\,\mathrm{nm}^3$) and finding the density in each cell. Since the crystal is not space fixed and has the freedom to diffuse in x and y direction, the grid geometry is attached to the crystal in order to get consistent density distributions in the course of the MD simulations. This is done by fixing grid points to the surface carbon atoms of the crystal. The density distribution is evaluated using

$$\rho(\vec{r}) = \frac{< N[\vec{r}, (x - \frac{\Delta x}{2}, x + \frac{\Delta x}{2}), (y - \frac{\Delta y}{2}, y + \frac{\Delta y}{2}), (z - \frac{\Delta z}{2}, z + \frac{\Delta z}{2})] > \mathrm{M_W}}{\Delta x \Delta y \Delta z}.$$

where $\vec{r} = (x, y, z)$ is the centre of the cell, Δx, Δy, Δz are the length of the sides of the cell, M_w is the molecular weight of water and $< N[\vec{r}] >$, is the number of water

oxygens inside the cell at $\vec{r}$ averaged over the 10^3 trajectory frames. The density distributions were converted to local chemical potentials using Boltzmann inversion[33]

$$\Delta\mu(\vec{r}) = -RT \ln\left(\frac{\rho(\vec{r})}{\rho_{Bulk}}\right).$$

ρ_{Bulk} is the bulk density of water away from the surface calculated at the center of the water layer, $\Delta\mu(\vec{r})$ is the difference of the chemical potential between position $\vec{r}$ and the bulk water chemical potential. For $\Delta\mu(\vec{r}) < 0$, position $\vec{r}$ is hydrophilic, and if $\Delta\mu(\vec{r}) > 0$ it is hydrophobic.

2.3 RESULTS AND DISCUSSION

2.3.1 Density distribution of water near different surface structures

In order to understand the effect of the surface topography on the interfacial water, the water density inside and outside the holes is analysed. This is done in slabs (layers) of 0.2 nm thickness placed at different heights (z) above the surface. The water density inside the holes (z < 0) is summarily calculated and not subdivided further. The different slabs considered thus are –5 to 0 nm, 0 to 0.2 nm, 0.2 to 0.4 nm, 0.4 to 0.6 nm. Such an analysis has in the past been used to investigate the hydrophobicity of cellulose surfaces.[33]

The water density (Fig. 2.6) inside the holes (z = -0.5 to 0 nm) is of the order of 0.5 g/cm^3, which is about half the bulk water density at the temperature and pressure at which the simulations were performed. At this level, there is no water density away from the holes, which means the water does not penetrate the alkane slab. In all holes, the water density has a maximum at the centre and is lowest at the sides, which implies that the water avoids contact with the sides of the hydrophobic holes. The apparent seeping of water density into non-hole regions is an artefact due to the low resolution of the grid and the interpolation algorithm of the graphics program.

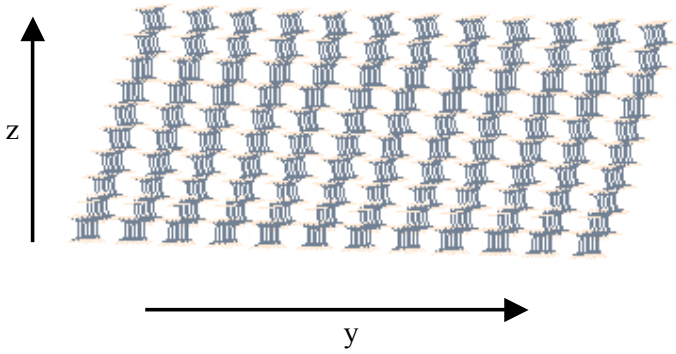

Figure 2.1: The planar n-eicosane crystal used in our simulations as a model for hydrophobic surface.

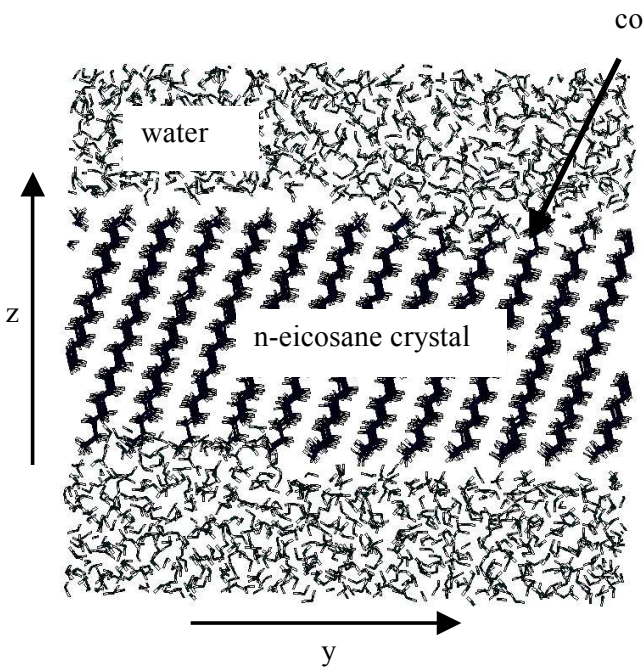

Figure 2.2: The system chosen for our MD simulation. One corrugation/hole is indicated in the figure.

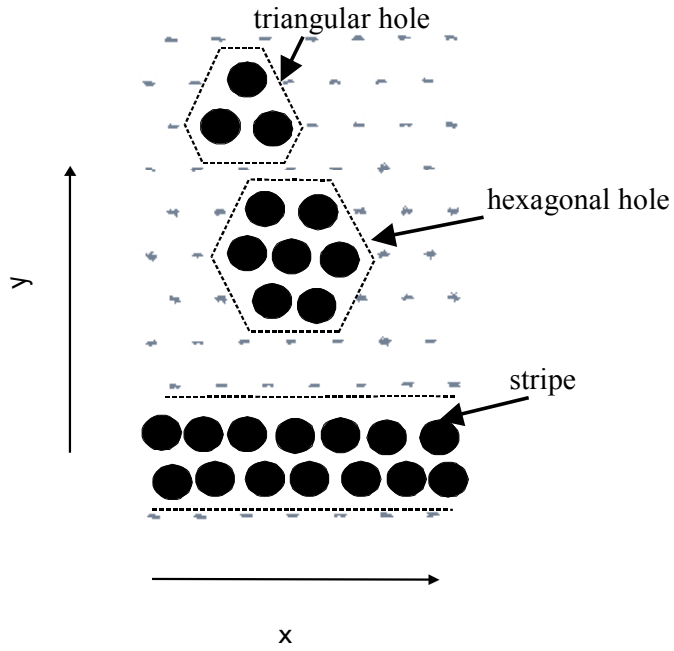

Figure 2.3: Schematic representation of the holes in our simulation. The dark spots indicate the alkane chains which have been shortened by 4 carbons.

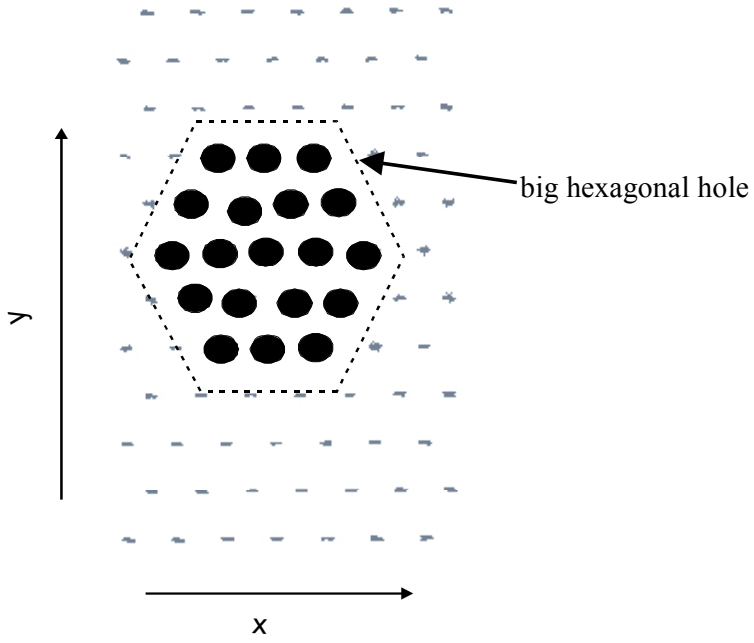

Figure 2.4: Schematic representation of a big hexagonal hole. The dark spots indicate the alkane chains which have been shortened by 4 carbons.

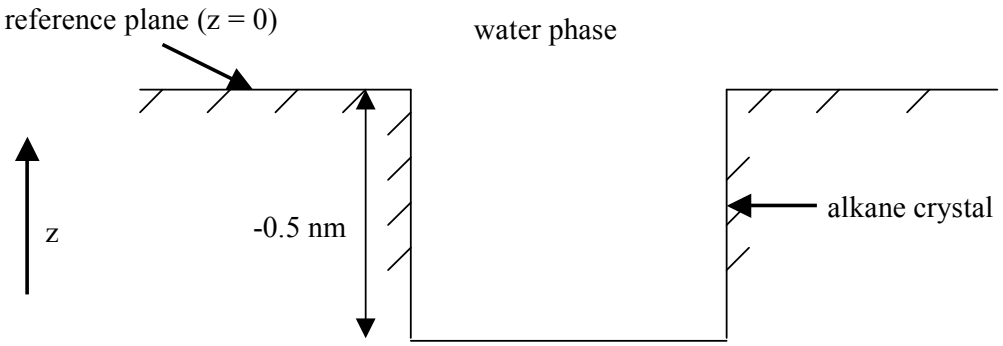

Figure 2.5: The schematic of the hole. The reference height (z = 0) is the average of the terminal methyl carbons. The depth of the hole is ~ 0.5 nm.

At 0-0.2 nm from the surface (Fig.2.7), there are only few water density spots on the surface of the planar crystal (Fig. 2.7e) and between the holes in the other surface structures as the slab thickness is too small to completely include the first layer of water molecules. The density of water is here around 0.2 g/cm^3. As a byline, we note that the underlying crystal structure is visible in the water density (with some artefacts due to interpolation of the graphics program): Water molecules can approach the surface between holes and the planar surface most closely at the small depressions between adjacent CH_3 head groups. Above the holes, the water density is larger, rising to 0.7-0.8 g/cm^3 above the centers of the holes. This is comparable to the densities inside the holes and still much below the bulk value. At this level, the hole geometry is very much visible in the water density.

In the layer between 0.2 and 0.4 nm (Fig. 2.8), the hole geometry is visible in the water density only for the large surface structures (big hexagon, stripes). The density is highest above the centres of the holes, reaching 0.8 g/cm^3 for the big hexagon and 0.9 g/cm^3 for the stripes. These densities are lower than that above the planar surface (Fig. 2.8e). Most surprising is, however, that in the same structured surfaces (Fig 2.8. a, b) also the density above the regions between holes is on average lower (0.5-0.6

g/cm^3) than above the planar surface (~ 0.8 g/cm^3 , Fig. 2.8e). This is an indication of the surface structure influencing the water distribution also away from the holes, leading effectively to a depletion of water from the first layer. Finally, the alkane crystal structure is still reflected in the water density at this height. For the smaller holes (hexagon, triangle), the water density above the hole is essentially the same between the holes.

At the level between 0.4-0.6 nm distance, the density above the planar slab seems to have reached the bulk value of 0.98 g/cm^3 (Fig. 2.9e). The 0.4-0.6 nm slab happens to enclose some of the second density peak at about 0.6 nm and some of the minimum at ~ 0.5 nm. The two average out to the bulk density. Similarly densities are reached for the surfaces containing small hexagonal and triangular holes (Fig. 2.9c, d). The small features no longer have very marked effect on the water density distribution at this distance. More interesting is the effect of the larger structures (Fig. 2.9a, b). The density above the big hexagonal holes is around 0.7 g/cm^3, whereas it is just below the bulk value elsewhere (Fig. 2.9a). This means the big hexagonal hole induces a zone which has a lower density and separates the bulk water and the water inside the holes. There is a similar density reduction above the stripes (Fig. 2.9b), which however is smaller in magnitude (ρ = 0.8 g/cm^3) and spatial extent. Moreover the water density reaches and exceeds bulk values between the stripes (Fig. 2.9b), while it is mostly below the bulk value between big hexagonal holes (Fig. 2.9a). From the discussion so far it can be concluded that surface structures of the size of this hole (diameter 2.5 nm) are most effective for reducing the water density in the interface region.

All structuring leads to a reduction of the water density compared to the planar slab. Using Boltzmann inversion, this information can be converted into a local chemical potential $\Delta\mu$ and, hence, a hydrophibicity. For the most effective structure, the big hexagonal hole, a $\Delta\mu \approx +0.8$ kJ/mol is found in the 0.4-0.6 nm level above the hole and $\Delta\mu \approx +0.4$ kJ/mol between the holes. These values must be compared with the equivalent chemical potential above the planar surface ($\Delta\mu \approx +0.4$ kJ/mol). It is then

evident that the surface structuring produces a water layer at 0.4-0.6 nm which is more hydrophobic than the corresponding layer above the flat surface. Similar considerations of the next lower layer (0.2–0.4 nm, Fig 2.8a), which comprises the water density maximum near the surface, show that $\Delta\mu \approx$ 0.9 kJ/mol above the big hexagonal holes and $\approx$ 1.9 kJ/mol between them, compared to $\Delta\mu \approx$ 0.64 kJ/mol above the flat surface. Therefore, also at close distance the structured surface is more hydrophobic than the flat one.

2.3.2 Water density normal to the surface

Figure 2.10 shows the density averaged in the x and y direction as a function of z. The same grid as before is used for the analysis. At $z < 0$, only those grid cells contribute, which have a non-zero water density. Recall that $z = 0$ corresponds to the height of the surface carbons. Thus, cells inside the alkane crystal are excluded. The first peak above $z = 0.35$ nm is sharpest for the planar crystal which corroborates our previous finding that the structuring of water near the planar crystal is higher. The lowest first peak above $z = 0.35$ nm is found for the stripes followed by the big hexagonal holes. Given the results of the last section, this finding might at first be surprising. However the total surface area of the two stripes (28 alkanes shortened) is larger than that of the big hexagonal hole (19 alkanes shortened). For the structured surfaces the density of water inside the stripes is by far the highest. (0.4 g/cm^3). For the other hole geometries the maximum density inside the holes is around 0.2 g/cm^3 or lower.

We have also converted the density distributions into chemical potential differences by Boltzmann inversion, (Figure 2.11). Above the surface ($z > 0$) the first chemical potential well is slightly deeper in case of the planar crystal (300 J/mol) than the structured surfaces. The chemical potential inside the stripes rises to 2 kJ/mol (0.8 kT), whereas for other structures it rises to 4 kJ/mol (1.6 kT). This clearly indicates that the holes are hydrophobic regions. The relatively low chemical potential inside a stripe is interesting: A possible explanation is that, water ordering is still possible in

the direction of the infinitely long grooves, whereas in all other hole geometries, the water structuring is perturbed from two directions.

To investigate the influence of temperature on hydrophobicity, we did an NPT simulation at 368 K on the big hexagonal hole system. At 368 K the overall density is lower than at 298 K and density variations with z are smaller (Fig 12). Also the density inside the hole is lower. The chemical potential difference obtained by Boltzmann inversion of the density (Fig. 13) automatically takes care of the overall thermal expansion. The chemical potential inside the hole with respect to the bulk at the same temperature increases with temperature, so the hole becomes more hydrophobic. Similarly, the well outside the hole ($z \approx 0.3$ nm) becomes shallower, so the surface as a whole becomes more repulsive towards water. This result shows that the side walls of the hole try to impose their ordering effect on the water molecules inside the hole as well. The overall increase of perpendicular orientation is a result of the competition between these vertical walls and the horizontal surface. Away from the holes, the correlation of the dipole moment vectors decays to zero, which means that water molecule share no preferred orientation with respect to the surface normal.

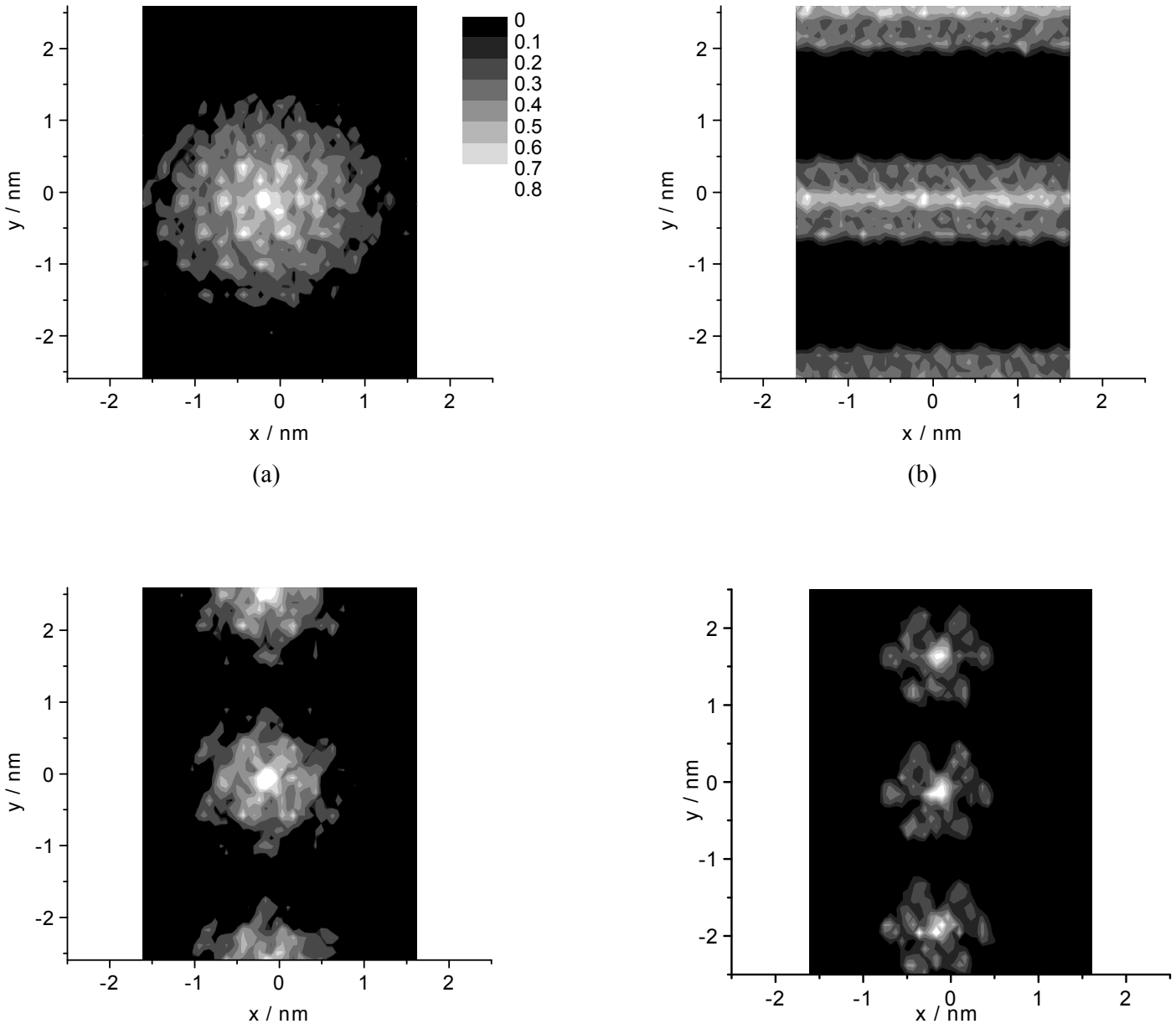

Figure 2.6 Density distribution of water inside different holes (z = -0.5 to 0 nm) (a) Big hexagonal holes (b) Stripes (c) Hexagonal holes (d) Triangular holes. The shape of the holes is clearly seen in the figure. The density inside the holes is around 0.5 g/cm^3 except for the triangular holes where the density is ~ 0.2 g/cm^3.

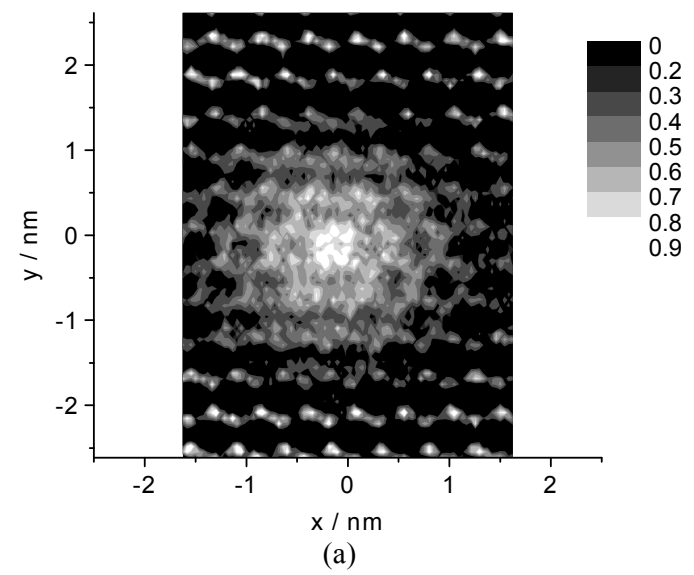

(a)

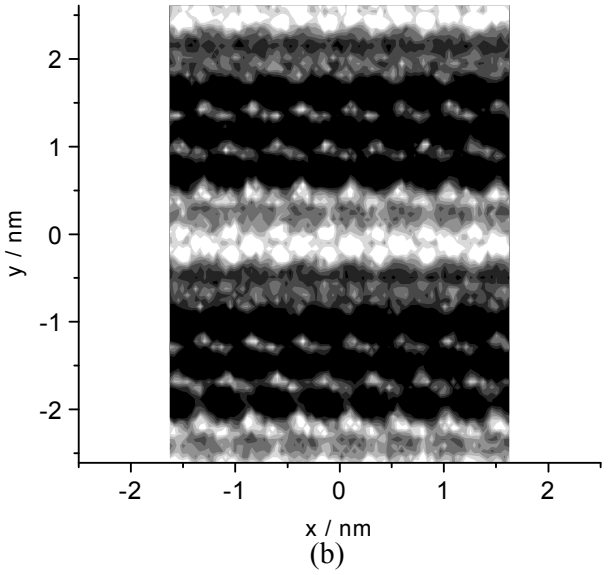

(b)

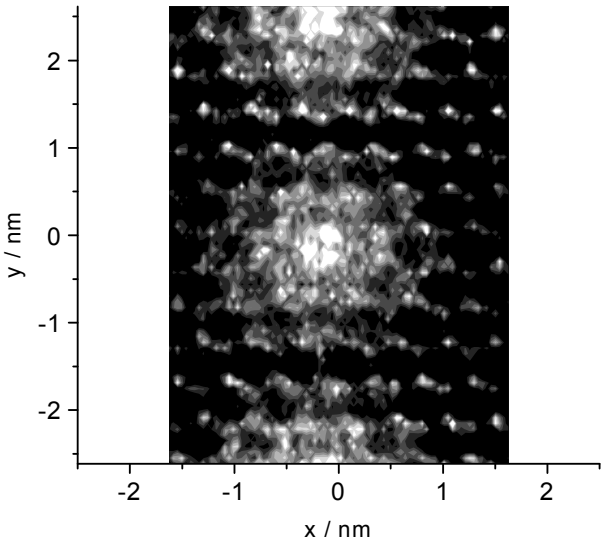

(c)

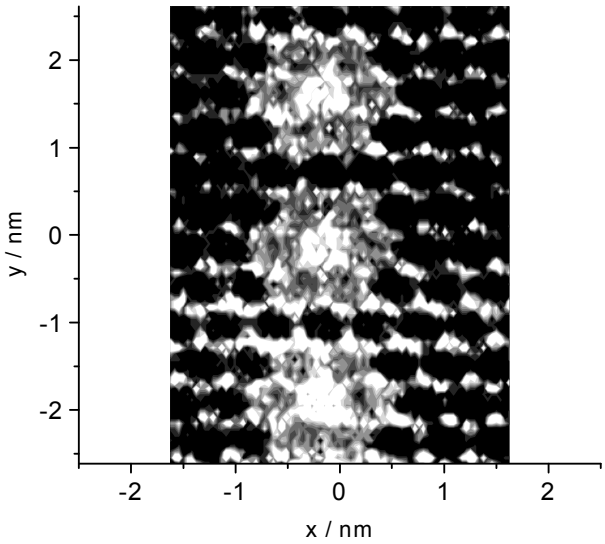

(d)

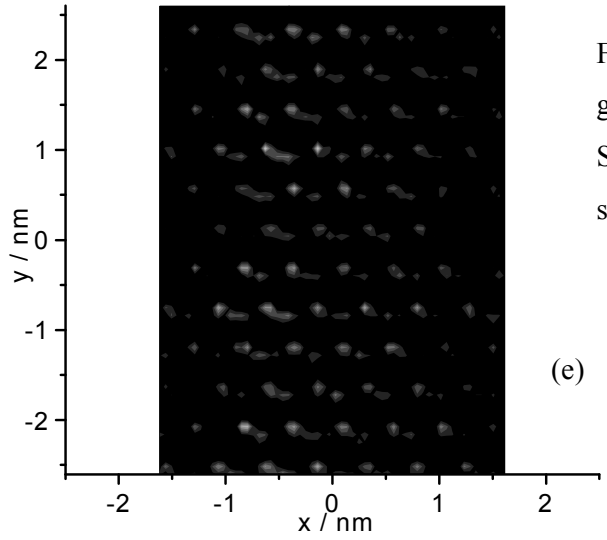

(e)

Figure 2.7 Density distribution of water for different hole geometries (z = 0-0.2 nm) (a) Big hexagonal holes (b) Stripes (c) Hexagonal holes (d) Triangular holes (e) Planar surface.

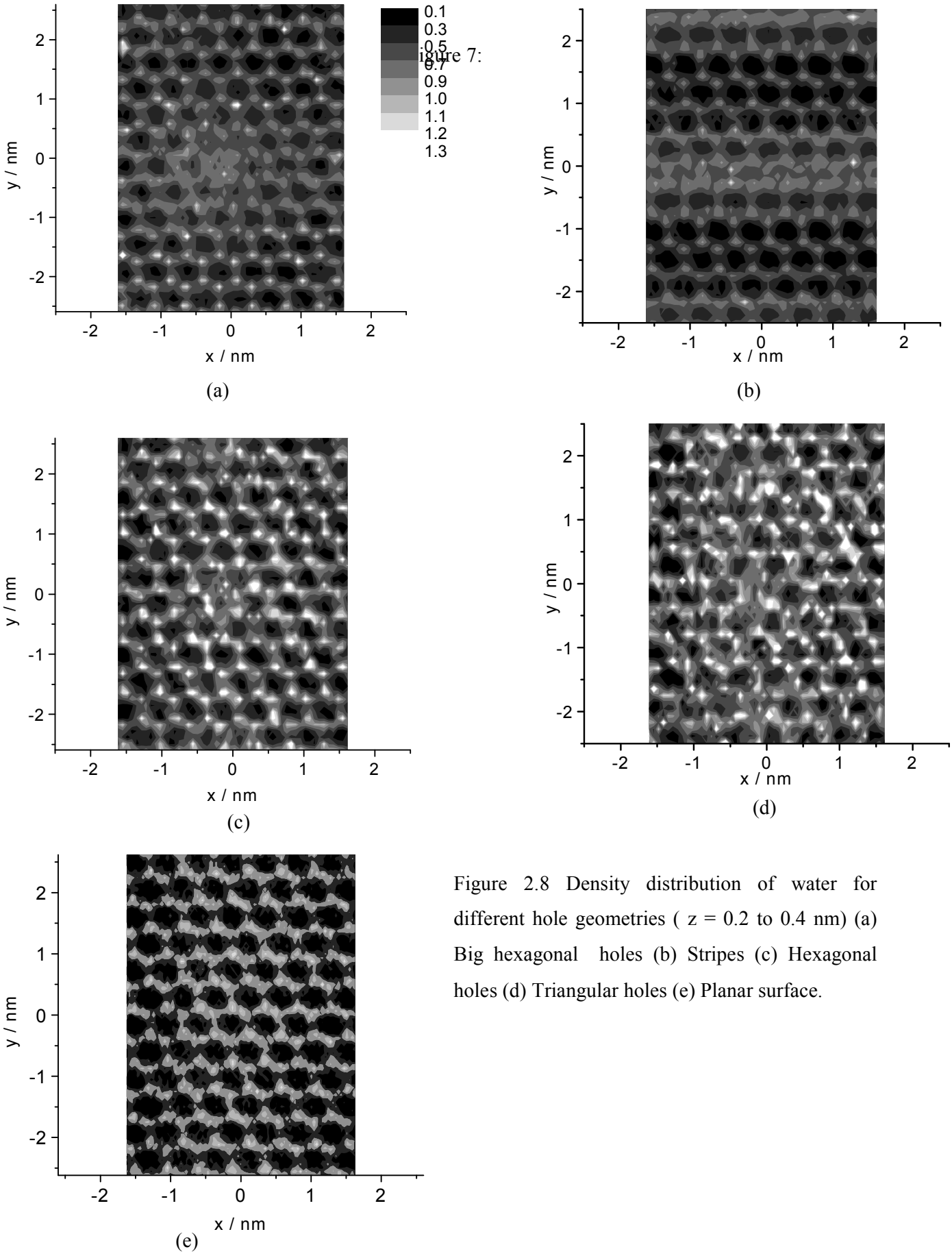

igure 7:

Figure 2.8 Density distribution of water for different hole geometries (z = 0.2 to 0.4 nm) (a) Big hexagonal holes (b) Stripes (c) Hexagonal holes (d) Triangular holes (e) Planar surface.

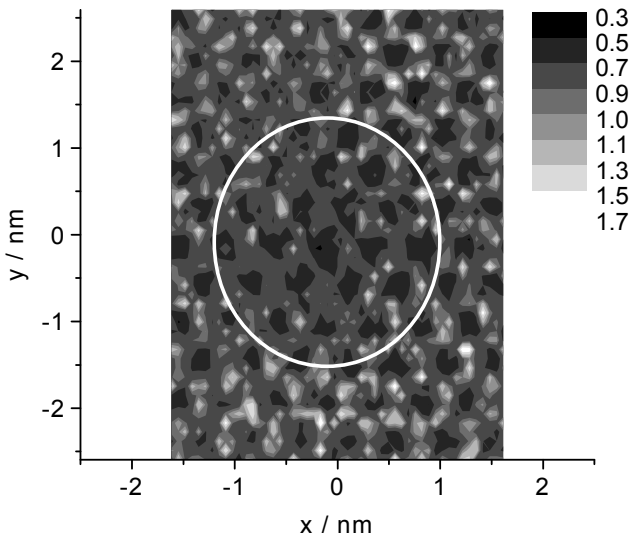

(a)

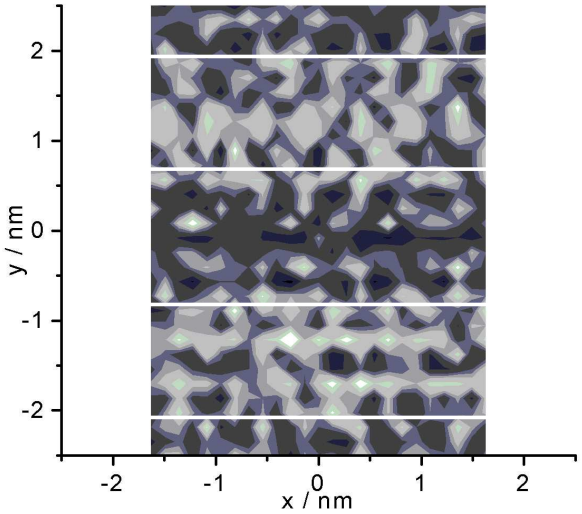

(b)

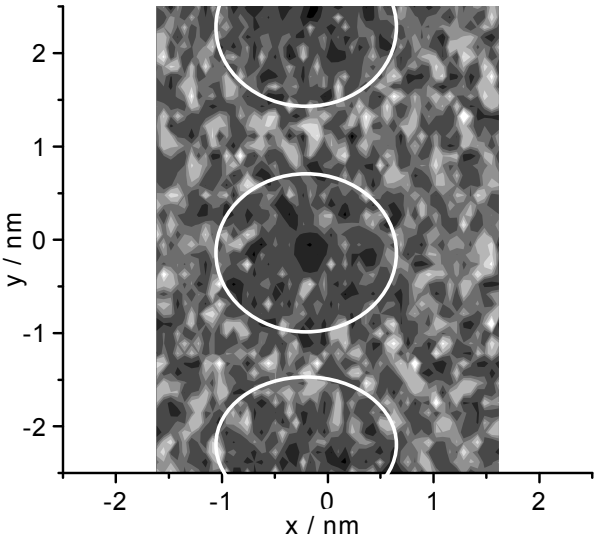

(c)

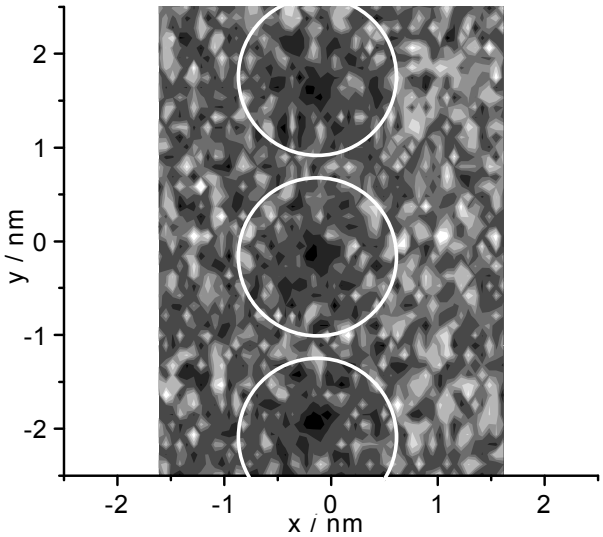

(d)

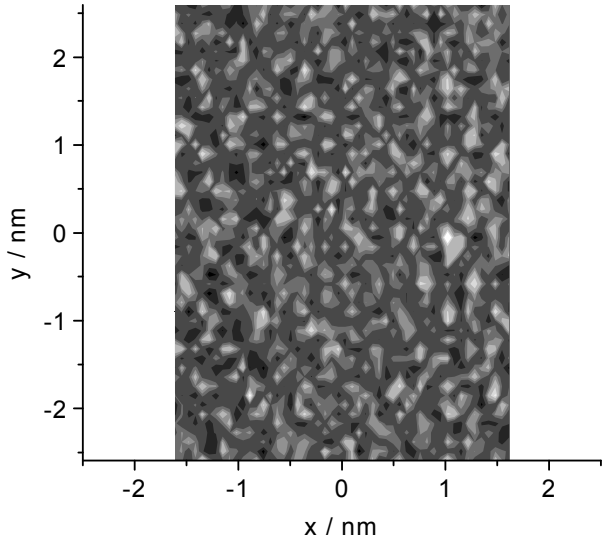

(e)

Figure 2.9 Density distribution of water for different hole geometries (z = 0.4 to 0.6 nm) (a) Big hexagonal holes (b) Stripes (c) Hexagonal holes (d) Triangular holes (e) Planar surface. The influence of surface structure on the water density is marked in the figures.

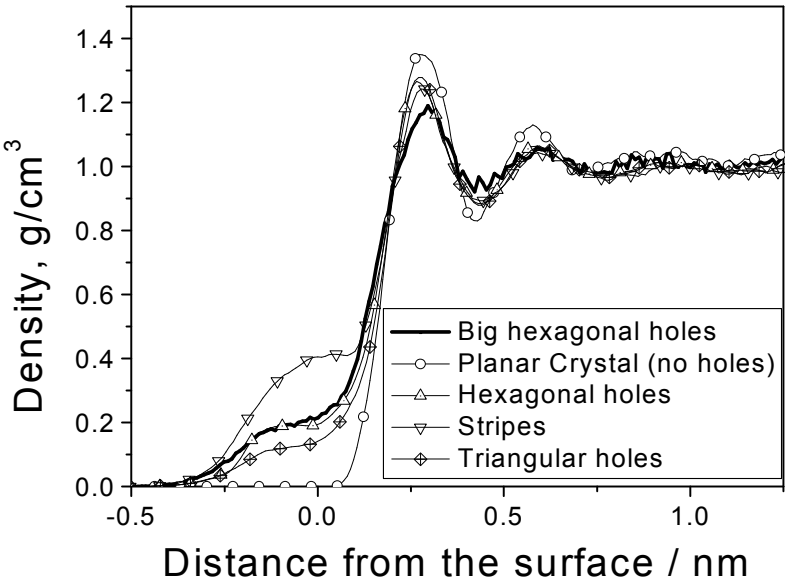

Figure 2.10 Density of water as a function of z, the distance from the surface.

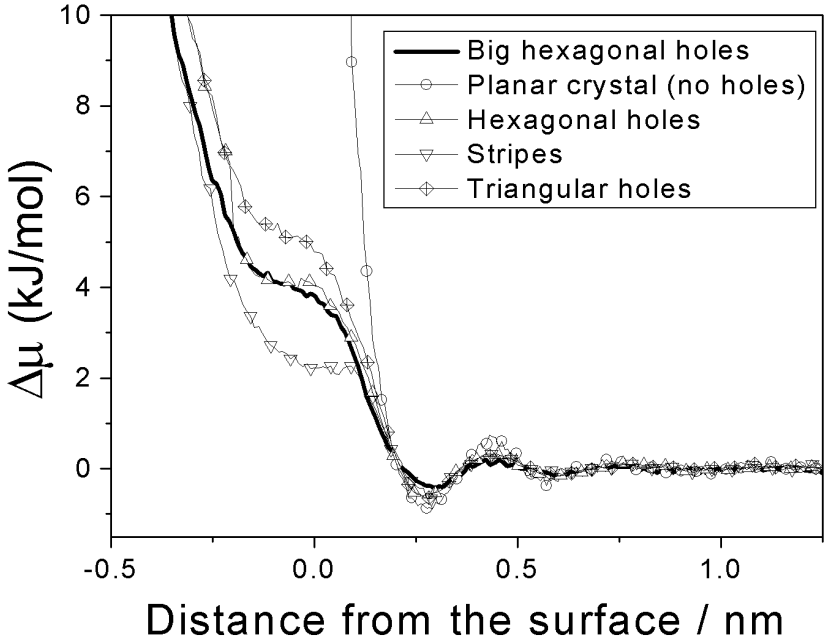

Figure 2.11 Difference of the water chemical potential at a height z and bulk water obtained by using Boltzmann inversion.

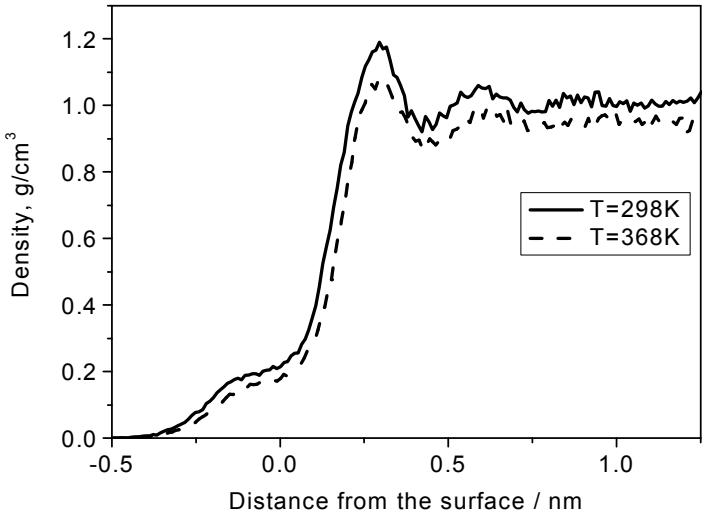

Figure 2.12 Density of water near the big hexagonal holes at two different temperatures.

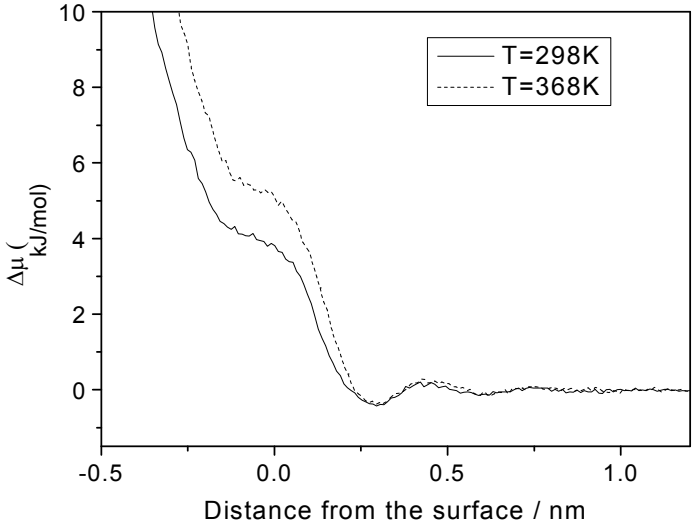

Figure 2.13 Chemical potential difference with respect to respective bulk value at 298 and 368 K.

2.3.3 Water density profiles inside the holes

The density distribution inside the holes has been shown in Figure 2.6. In figure 2.14, it is compared more quantitatively for the different geometries. The same grid geometry as before was chosen in this case as well, however the density was averaged in the x and z directions ($z < 0$) to have a density profile in y direction. We have also averaged the density in the y and z direction ($z < 0$) and obtained a profile in x. Figure 14a indicates which part of the hole was averaged over. In case of hexagonal and triangular hole: some parts of the hole has been excluded from analysis to avoid the angular edges of the hexagonal and triangular holes and to give the consistent density distributions.

Cutting through a hole in both y (Fig. 2.14 b) and x direction (Fig. 2.14c), the density increases from the edges of the hole toward the centre. This is qualitatively similar for all holes, except of course for the density profile along the stripe, which is flat (Fig 2.14 c). The densities at the hole centres reach 0.7-0.9 g/cm^3 for all hole types. The increase shows small differences between hole types and directions: For the big hexagonal hole it appears more or less consistent, whereas for the smaller holes, often a stepwise increase is found. The step length is often around 0.4 nm, the diameter of a water molecule, suggesting a layered build-up of the density. Due to the large statistical noise, however, this feature has not been further analysed.

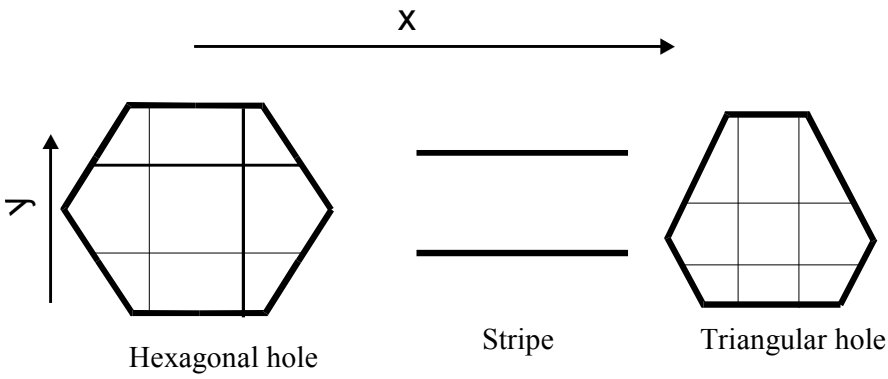

(a)

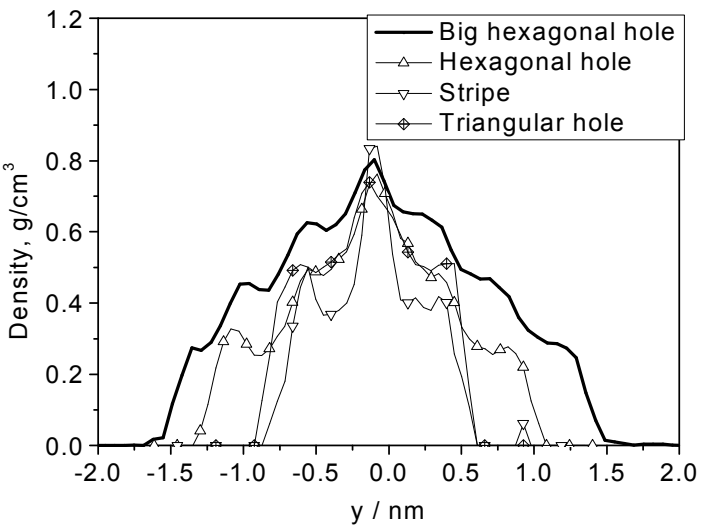

(b)

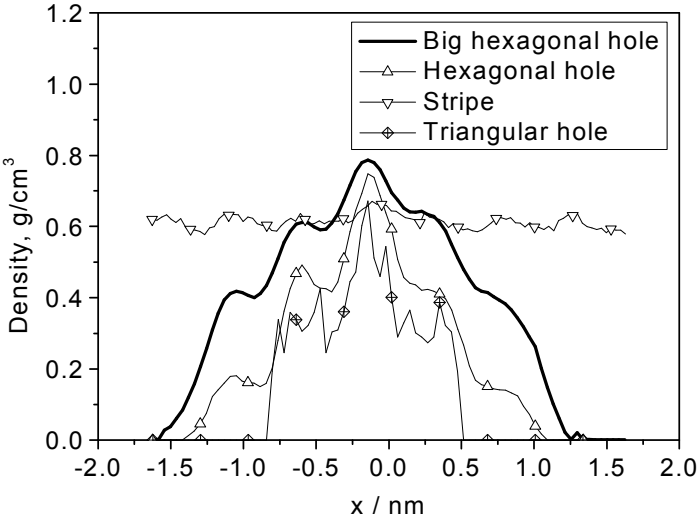

(c)

Figure 2.14 Density of water inside the holes in vertical slices for different holes (a) Schematic representation of the slices for different hole geometries. (b) The density of water inside the holes as function of y. (c) The density of water inside the holes as a function of x.

2.3.4 Orientation of water near a hydrophobic surface

From previous works,[23,34-36] we know that the dipole moment vector of the water molecule near a hydrophobic surface is preferentially parallel to the surface. The orientation was measured by an order parameter (S^2) of the angle θ_μ between the normalized water dipole vector $\vec{\mu}$ and the surface normal of the alkane crystal $\vec{u}$.

$$S^2 = 0.5 < 3\cos^2\theta_\mu - 1 > .$$

A positive value implies that the molecules prefer to align perpendicular to the surface, it is negative when the preferred alignment is parallel to the surface. It is zero for random orientations. We have investigated the orientation of water near all the crystal geometries as a function of z (Fig. 2.15 a). We can clearly see the parallel orientation of water near the planar crystal surface ($z \approx 0.2$ nm). For all hole geometries we see a second weaker parallel alignment inside the holes ($z < 0$). Towards the entry of all the holes ($z \approx 0$), the water is more disordered than either in the hole or immediately outside. Figure 2.15(b), shows a chart of the orientation S^2 of water molecule inside the big hexagonal hole averaged over (-0.5-0 nm). Near the edges of the hole the water orientation is preferentially parallel to the surface. At the hole centre the water orientation is perpendicular to the surface. The order parameter does not distinguish between the up and down orientations of water with respect to the surface. To investigate this, we have plotted the orientational distribution function (ODF) of water as a function of distance z from the surface for the big hexagonal hole Fig. 15(c). The ODF(z) is the dot product of the unit dipole moment vector of the water molecules and the surface normal $\vec{u}$,

$$\mathrm{ODF(z)} = \left\langle \cos(\theta_\mu(\mathrm{z})) \right\rangle = \left\langle \vec{\mu}_\mathrm{i}(\mathrm{z}).\vec{u} \right\rangle ,$$

where $\vec{\mu}(z)$ is the dipole moment vector of water molecules at z. Figure 2.15(c) shows that the dipole moment vectors of the water molecules are preferentially pointing towards the carbon atoms inside the hole, being anti parallel to the surface

normal. In other words, the oxygen atoms of the water molecules point away from the surface.

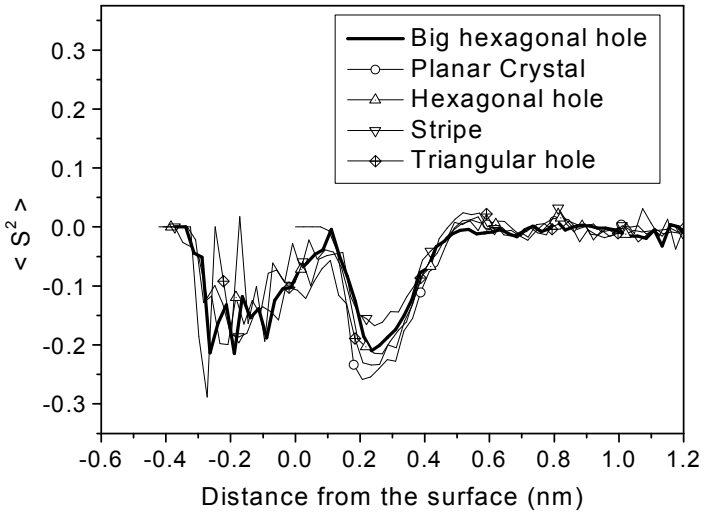

(a)

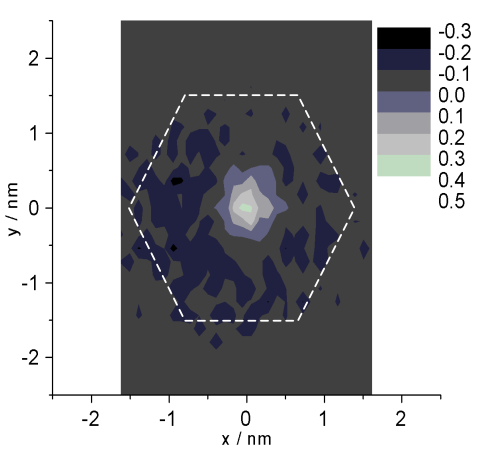

(b)

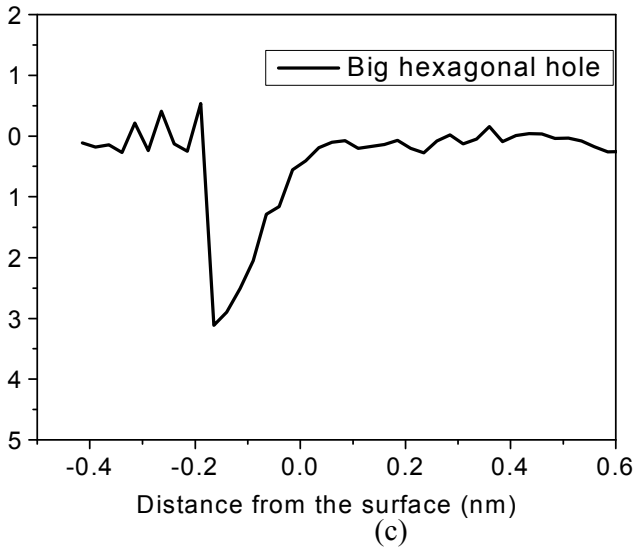

(c)

Figure 2.15 Orientation of water (section 3.4) in the vicinity of the big hexagonal holes. (a) The order parameter $S^2(z)$ of water as a function of the distance, z, from the surface of the slab. A negative S^2 signifies that water molecules lie flat on the surface (xy plane), a positive S^2 signifies that their dipole moment vector is perpendicular to the surface. (b) Water order parameter S^2 inside the hole. The orientation values are not considered outside the big hexagonal hole depicted. (c) The orientational distribution function ODF(z) as a function of the distance, z, from the surface of the slab. A positive value of the ODF signifies that the water hydrogens point away from the surface (xy plane), a negative value that the point towards the surface.

2.3.5 Hydrogen bonding

A pair of water molecules is defined to be hydrogen bonded if their oxygen atoms are within 0.35 nm and if the OOH angle at both oxygen atoms involved in the bonding is less than 30^0. The threshold OOH angle set by studying the average number of hydrogen bonds per water molecule as a function of the threshold angle.[34-37] With this definition, the average number of hydrogen bonds per water molecule is ≈ 2.0 in the bulk (Fig.2.16). To find the local number of hydrogen bonds we have calculated the number of hydrogen bonds in each slab of thickness 0.05 nm and divided by the number of molecules in the slab. Hydrogen bonds extending over two slabs were counted half for each slab. The number of hydrogen bonds per molecule of ≈ 2.0 in the bulk agrees with previous work[34-37], which found 1.94. The water inside the big hexagonal holes shows a significantly lower hydrogen bonding between 1.1 and 1.7 depending on the depth. A somewhat surprising feature is the peak at $z \approx$-0.15 nm followed by a minimum at $z \approx 0.1$ nm. This maximum-minimum structure occurs at the same range of $z \approx 0$ as the intervening maximum of the water order parameter $S^2(z)$ (Fig. 2.15a). At present, we do not know if this has a physical explanation or is merely a coincidence.

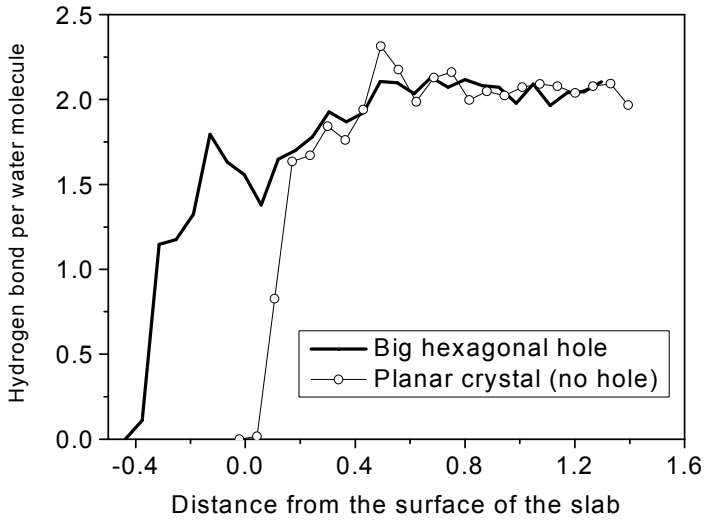

Figure 2.16 Average number of hydrogen bonds per water molecule as function of z.

2.3.6 Contacts of water and the surface carbon atoms of the crystal

The hydrophobicity of an interface can be judged by the number of contacts the water makes with the surface atoms. The more contacts there are, the larger is the residual dispersive attraction between water and surface, and the lower is the hydrophobicity. The contacts are calculated from the corresponding radial distribution function. Figure 17 shows the radial distribution functions between oxygen atoms of the water molecules and the surface carbons. As surface carbons we count all methyl carbons at chain ends, whether inside or outside the hole, as well as the three following methylene carbons of the chains forming the sides of the holes. The first peak, at r = 0.38 nm is lowest for the big hexagonal hole which clearly means fewer contacts between water and the alkane crystal in this case. All other surface structures lead to more contacts than the big hexagonal hole. The number of contacts is obtained by integrating the first peak of the radial distribution function (0 to 0.5 nm), see Table 1, and it is analysed both from the water side (number of contacts per water molecule) and the surface carbon side (number of contacts per surface carbon atom). At first we present the comparison of the number of contacts per water molecule. Table 1 shows that the number of contacts per water molecule is 1.5 times smaller for the big hexagonal hole than for the planar slab. The triangular and the hexagonal holes lead to more water contacts per water molecule than the big hexagonal hole, probably because they leave more of the planar surface intact. In contrast, the stripes lead to a number of water contacts per water molecule already close to the planar surface, confirming that this structure is not particularly hydrophobic. Secondly, we present the number of contacts between water and surface carbon atoms per surface carbon, Table. 1. The number of contacts per surface carbon in case of the planar surface is 4.0, whereas for the structured surfaces the total number of contacts per surface carbon is approximately 3.0, with the big hexagonal hole being the lowest (< 3).

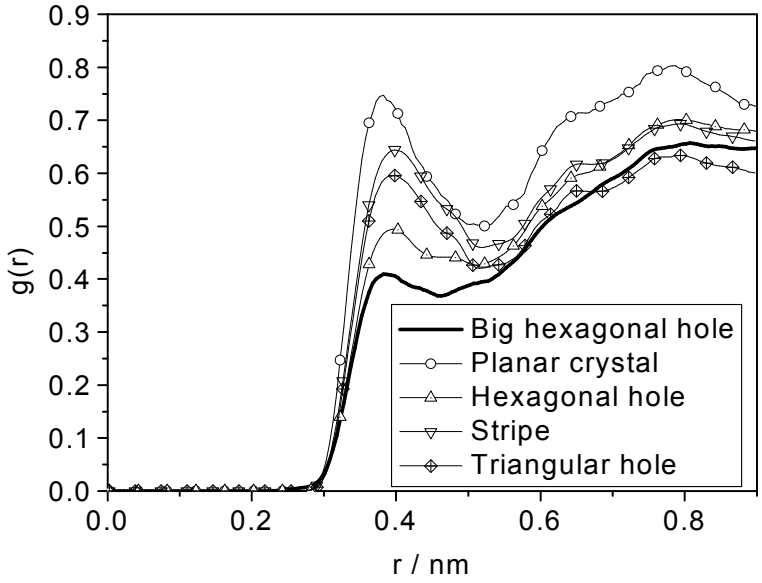

Figure 2.17 Radial distribution function between surface carbons and water oxygens.

Table 2.1: The number of contacts between water and the surface carbons for different geometries.

Surface topography	Number of contacts between water and surface carbons per water molecule (a)	Number of contacts between water and surface carbons per surface carbon (a)
(1) Big hexagonal hole	0.27	2.95
(2) Planar crystal	0.45	4.03
(3) Hexagonal holes	0.33	3.12
(4) Stripes	0.38	3.53
(5) Triangular holes	0.36	3.31

(a) Calculated by integrating the radial distribution function between 0 and 0.5 nm.

2.4 CONCLUSIONS

The calculations of this work show consistently that nanostructuring the surface of a hydrophobic material by placing indentations or holes into it makes it more water-repellent. This is demonstrated by the interfacial water density, which is lower in the vicinity of all surface structures than close to a planar hydrophobic surface. Lower water density is not only found inside the holes, but also above the holes and, for some hole geometries, between the holes. The corresponding local chemical potentials obtained from the density by Boltzmann inversion quantify the effect. The chemical potential for water is about 1 RT higher inside the holes than in bulk water. At the

height of the first complete water layer, the structured surfaces show also an overall increase of the chemical potential compared to a flat surface. It is, however, smaller and depends on the cumulative area of all holes. The chemical potential inside the holes, and consequently their hydrophobicity, increases with temperature.

The most effective structure for creating a water-repellent surface turned out to be the big hexagonal hole, which has a diameter of about 2.5 nm. The smaller holes occupy a lower fraction of the surface and their influence on the water structure is short-ranged. The long trenches, which cover a similar fraction of the area as the big hexagonal holes, contain water at a higher density and better order than any of the closed holes. This is explained by the influence of the vertical side walls of the holes. They are hydrophobic so the water tries to avoid them. In a long trench, the water is repelled by the two side walls north and south, whereas in the closed holes it feels the west and east walls as well. It is not clear whether the water density inside the hole is governed by the perimeter-to-area ratio of the hole or if this is an effect of the dimensionality of the hole. More experimentation with other hole shapes would be needed. Detailed analysis of the water density in big hexagonal holes also shows that it is approaching bulk values at the hole center. Therefore, it would make little sense to create hole structures significantly larger than the 2.5 nm. In the center there would be just another planar surface at a lower level and any water-density-reducing and hydrophobicity-increasing effects would be limited to the edges of the hole.

In agreement with previous results, we find that water molecules of the first layer on a planar hydrophobic surface preferentially lie flat on this surface. The presence of holes, however, perturbs this orientational ordering to some degree, firstly through the creation of low-density regions where orientation is less well defined, and secondly through the competing ordering influence of the vertical side walls of the holes.

Finally, all structured surfaces show a lower number of contacts between water molecules and surface methyl and methylene groups than the planar surface. As the number of contacts is a measure of the dispersive attraction between water molecules and surface atoms, a lower number is indicative of a lower enthalpic part of the

interfacial energy. The quantitative analysis in terms of the interfacial free energy will be the subject of future work**.** All nanostructures reduce the number of contacts compared to the planar crystal. Among the surface structures, the big hexagonal hole shows the lowest number of contacts and appears again as the strongest candidate for creating surfaces with increased hydrophobicity.

Can the lotus effect be recreated on the nanometer scale? This depends on what we call the lotus effect. The qualitative picture at the nanoscale differs from the micron scale: There is no macroscopic water surface tension acting and pulling the water completely out of the holes. The water phase does enter the holes. However, it does so with a much reduced density and an increased interfacial chemical potential. This leads to fewer water-surface contacts and a higher hydrophobicity. Therefore, creating structure at both the micrometer and the nanometer level makes an already hydrophobic surface even more hydrophobic.

References

(1) Adamson, A. W. *Physical Chemistry of Surfaces*. London**,** Wiley, **1990**.

(2) Israelachvili, J. N. *Intermolecular and surface forces*. Academic Press, San Diego, **1991**.

(3) Neinhuis, C.; Barthlott, W. *Annals of Botany.* **1997**, *79*, 667.

(4) Baker, E. A.; Parsons, E. *Journal of Microscopy.* **1971,** *9*4, 39.

(5) Barthlott, W. In: Claughter D, ed. *Scanning electron microscopy in taxonomy and functional morphology* Oxford: Clarendron Press, **1990**, 69.

(6) Baker, E. A.; Parsons, E. *Journal of Microscopy.* **1971,** 94, 31.

(7) Cassie, A. B. D.; Baxter, S. *Trans of Faraday Society.* **1944**, 40, 546.

(8) Adam, N. K.; In: Moilliet JL, ed. *Waterproofing and water-repellency*; **1963**, Elsevier, Amsterdam, 1.

(9) Linsken, H. F. *Planta.* **1950,** 38 , 591.

(10) Rentshler, I . *Planta.* **1971,** *96*, 119.

(11) Huang, D. M.; Chandler, D. *J. Phys. Chem*. B **2002**, *106*, 2047.

(12) Davidchack, R. L.; Laird, B. B. *J. Chem. Phys*. **2003**, *118*, 16.

(13) Kirkwood, J. G.; Buff, F. P. *J. Chem. Phys.* **1949**, *17*, 3.

(14) Blokhuis, E. M.; Bedaux, D.; Holcomb, C. D.; Zollweg, J. A. *Mol Phys.* **1995**. *85*, 3, 665.

(15) Marmur, A. *Langmuir* **(Communication)**. **2004**, *20(9)*, 3517

(16) Wenzel, R.N. *Ind. Eng. Chem*. **1936**, 28, 988.

(17) Krupenkin, T. N.; Taylor, J. A.; Schneider, T. M.; Yang, S. *Langmuir* **(Communication). 2004,** *20(10),* 3824.

(18) Otten, A.; Herminghaus, S; *Langmuir* **(Communication). 2004**, *20(6)*, 2405

(19) Cottin-Bizzonne, C.; Barentin C.; Charlaix, E.; Bocquet, L.; Barrat, J.; *Eur. Phys. J. E*, **2004**, *12*, 427.

(20) Nyburg, S. C.; Potworowski, J. K.; *Acta Cryst*. **1973**, *B29*, 347.

(21) Waheed, N.; Lavine, M. S.; Rutledge, G. C.; *J. Chem. Phys*, **2001**, *116*, 2301

(22) Small, D. M.; *The Physical Chemistry of Lipids: From Alkanes to Phospholipids.* Plenum, New York, **1986**, 183.

(23) Grigera, J. R.; Kalko, S. G.; Fischbarg, J. *Langmuir*. **1996**, *12*, 154.

(24) Müller-Plathe. F. *Comput. Phys. Commun*. **1993,** *78*, 77

(25) Allen, M. P.; Tildesly, D. J. *Computer simulation of liquids*; Clarendron Press: Oxford, **1987**.

(26) Frenkel, D.; Smit, B. *Understanding Molecular Simulation*; Academic Press, San Diego, **2002**.

(27) Jensen, F.; *Introduction to Computational Chemistry*, Wiley VCH, Chichester, **1998**.

(28)Berendsen, H. J. C.; Postma, J. P. M.; van Gunsteren, W. F.; DiNola, A.; Haak, J. R. *J. Chem. Phys*. **1984**, *81*, 3684.

(29) Ryckaert, J. P.; Ciccotti, G.; Berendsen, H. J. C. *J. Comp. Phys*. **1971**, *23*, 237.

(30) Duffy, E. M.; Jorgensen; W. L. *J. Am. Chem. Soc*. **2000**, *122*, 2878.

(31) Kaminski, G.; Duffy, E. M.; Matsui, T.; Jorgensen, W. L. *J. Phys. Chem*. **1994**, *98*, 13077.

(32) Berendsen, H. J. C.; Grigera, J. R.; Straatsma, T. P. *J. Phys.Chem*. **1987**, *91*, 6269.

(33)Biermann, O.; Hädicke, E.; Koltzenburg, S.; Müller-Plathe. F. *Angew. Chem. Ind. E.* **2001**, *113* , 3938.

(34) Pal, S.; Balasubramanian, S.; Bagchi, B. *Physical Review E*. **2003,** *67*, 65102.

(35) Forsman, J.; Jönsson, B.; Woodword, C. E. *J. Phys. Chem*. **1996**, *100*, 15005.

(36) Svishchev, I. M.; Kusalik, P. G. *J. Phys. Chem*. **1993**, *99*, 3049.

(37) Luzar, A.; Chandler, D. *J. Chem. Phys*. **1993**, *98*, 8160. (b) Luzar, A.; Chandler, D. *Phys. Rev. Lett*. **1996**, *76*, 928. (c) Luzar, A.; Chandler, D. *Nature*

Chapter 3

Molecular Dynamics Simulation of Aqueous NaF and NaI Solutions near a Hydrophobic Surface

ABSTRACT

We present results from molecular dynamics simulation of aqueous solutions of alkali halide salts (NaI and NaF) at the interface with hydrophobic objects. The primary objective of this study is to investigate the structural properties of the salt solutions at the hydrophobic surface. An alkane crystal has been taken as the parent model for a hydrophobic surface. A hexagonal hole was created on it, which was half a nanometer deep and 2.5 nanometers wide. The density distributions of different species (water, anions and cations) are studied as a function of distance from the surface. While iodide prefers the interface, the fluoride ions stay inside the bulk water region. The higher concentration of iodide ions at the interface drags sodium counterions to the interface. It also decreases the water density at the interface due to steric effects of the iodide ions. The number of contacts between the surface carbons and water decreases in case of the NaI solutions, but is unchanged for NaF solutions. The orientation of the water-ion and the water-water hydrogen bond vector orientations near the interface is discussed in detail.

3.1 INTRODUCTION

We investigate the structural and dynamical properties of water and ions near the water hydrophobic surface by molecular dynamics simulations. The electrolytes studied are NaF and NaI. The primary objective of this manuscript is to see the

---

Pal, S.; Muller-Plathe, F.;
J. Phys. Chem. B. ; **(Article); 2005**; *109*(13); 6405-6415.

structural properties in terms of density and concentration of water and ions, respectively. Two different topographies of hydrophobic surface have been studied to see whether surface structuring influences water and ion distributions. Another important aspect is the question whether the presence of anions at the interface changes the hydrophobic nature of the hydrophobic surface.

The related field of modelling the interface of the water/water vapour interface of an aqueous salt solution has been an active area of research. The traditional view that there are no atomic ions at the water/vapor interface has been challenged by molecular simulations.[1-9] The selective transfer of the salt anions to the water vapour interface on the basis of the atomic radius and the polarizability of the ions have been investigated by molecular dynamics simulations.[5-8] The traditional interpretation of this observation in terms of Gibbs adsorption equation[1-3] is that the alkali halide salts are repelled from the solution/air interface. Consequently, the generally accepted view has been for many decades that the interface of aqueous electrolyte solutions is devoid of ions, although there have been no direct measurements with molecular resolution to support this view. It has been shown by the work of Jungwirth et al,[6-7] using molecular dynamics simulations of a series of sodium halide solutions that an increase of surface tension does not necessarily imply ion depletion. In fact it was shown that, whereas the small, nonpolarizable fluoride anion is excluded from the interface, in accord with the traditional picture, all of the larger, polarizable halide anions are present at the interface, and bromide and iodide actually exhibit surfactant activity (enhanced concentration at the interface relative to the bulk).

Jungwirth et al[6-7] modelled the air/solution interface by performing 1 ns molecular dynamics simulations at 300 K of water slabs containing sodium halide (fluoride, chloride, bromide, or iodide) salts at 1.2 M concentration. The most important ingredient used in their simulations is a polarizable potential for both water and the ions.[8] In the NaF solution, both ions are strongly repelled from the surface, leaving an ion-free layer roughly 3.5 Å thick (i.e approximately the diameter of one water molecule). In contrast, iodide ions occupy a significant portion of the water/vapour

interface. The affinity of large anions for the interface was interpreted in terms of anisotropic solvation, which induces a substantial dipole on the ion. The resulting favourable dipole-dipole interactions compensate the loss of ion-dipole interactions that accompanies the transfer of an ion from the bulk solution to the interface. The simulations were analysed, in their article, by comparing with the measurements of differences in surface potentials between ionic solutions and pure water. Experiments[10-15] show a positive surface potential, which implies the presence of an ionic double layer near the surface with its positive side directed into the bulk solution.

It has been shown by molecular dynamics (MD) simulations of aqueous ionic solutions of different concentrations for two different salts of different anion size (NaCl and NaF at 300 K[16] in explicit water) that the larger anion Cl^- leads to a smaller increase in surface tension than the smaller F^- ion. The results presented in this simulation are in good agreement with the experimental data.[3]

A second area related to the present study is the solution behaviour of small hydrophobic solutes, and in particular, its variation with ion type and salt concentration. The thermodynamic and structural properties of the hydration of hydrophobic solute molecules in three tetramethylammonium [$N(CH_3)_4^+$] salt solutions at various concentrations obtained from molecular dynamics simulations have been studied in detail by Kalra et al.[17] The chemical potential of hard-spheres solutes was obtained using test-particle insertion to display both salting-in (increased solubility) and salting-out (decreased solubility) effects depending on the type of salt. Small and strongly hydrated fluoride ions are excluded from the vicinity of the hydrophobic solutes, leading to an increase of the local water density near the hydrophobic solute, which leads to salting-out. Opposite behaviour has been observed for large, less favourably hydrated bigger ions, which associate strongly with hydrophobic solutes.

Molecular dynamics simulations were performed by van der Vegt et al.[18,19] to study the hydration thermodynamics of methane infinitely diluted in binary cosolvent/water

mixtures. The additives sodium chloride (NaCl), dimethyl sulfoxide (DMSO), and acetone were studied at various additive/water ratios and analyzed in terms of solute-solvent energy and entropy changes upon solute insertion. The salting-in and salting-out behaviour of the co-solutes was analyzed in terms of the solvation free energy as well as the liquid structure in the vicinity of the methane molecule. NaCl is shown to salt out methane as the result of an unfavourable solute-solvent entropy change. Acetone and DMSO salt in non-polar solutes. Addition of acetone to water facilitates formation of empty molecular-sized cavities causing the salting-in process to be largely entropy driven.

Molecular dynamics simulations were performed on our system containing one n-eicosane ($C_{20}H_{42}$) crystal in contact with aqueous sodium iodide and sodium fluoride solutions. Two surface topographies were considered: (a) Planar crystal without any surface structuring and (b) hexagonal holes on both sides of the crystal. Our previous[20] simulations showed an enhancement in the hydrophobicity due to surface structuring. This result was obtained for a pure water phase. In the present contribution we investigate if this effect is also present for salt solutions, or if the holes trap ions and a charged surface is formed.

The alkali salts chosen for our simulations are NaF and NaI. Of the common halide anions, F^- is the smallest and I^- is the largest. Hence, any effect of ion diameter should be most pronounced between these two. The steric effects should also dominate over polarizability effects so that a non-polarizable force field is sufficient.

The main objective of this work is the distribution of water and ions near the hydrophobic surface. Differences between the hydrophobic surface and the solution/vapour interfaces are of interest, as the difference between the flat and the structured surface. Finally we investigate differences in the wetting behaviour between pure water and the two salt solutions.

Table 3.1. Ion Lennard-Jones parameters (σ, ε) and charges used in the simulations.

Ion/water	σ_{io} (nm)	ε_{io} (kJ/mol)	Charge(e)	Reference
Fluoride	0.3143	0.6998	-1	33
Iodide	0.4168	0.5216	-1	33
Sodium	0.2876	0.5216	+1	33

3.2 COMPUTATIONAL DETAILS

3.2.1 Details of the surface structure

A crystal of n-eicosane molecules ($C_{20}H_{42}$) (one layer of 7×12 molecules) serves as the model of the hydrophobic surface. n-eicosane has a triclinic crystal structure.[21-23] We used an idealized model surface for the n-eicosane crystal with no defects, Figure 2.2. Instead of non-bonded interactions between alkane molecules, springs were used between carbons of any chain and carbons of its six nearest neighbours taking into account periodic boundary conditions. More specifically, springs linked carbons of the same index (i.e. C_i - $C_i^{/}$, length: 0.497 nm) and carbons one index apart (C_i - $C_{i+1}^{/}$, length: 0.89 nm). These lengths were chosen to maintain the crystal structure of n-eicosane in constant pressure simulations. This rigidification was necessary not so much for the parent planar alkane slab, but to prevent surface reconstruction of structured alkane surfaces, which contained also shorter alkane chains.

Figure 2.4 shows how a structured surface is generated from the $C_{20}H_{42}$ crystal by shortening selected chains. We have tried two topographies: hexagonal hole (19 alkane molecules shortened by four carbons) and the parent planar crystal. The

schematic of the hole is shown in Figure 2.5. Measuring between carbon chain positions flanking the holes, the hexagonal hole has a diameter of approximately 2.5 nm. To convert to the inner widths, the diameter of a CH_3 group should be subtracted from these values. The total surface area of the hole is approximately 3.8 nm^2 (1 hexagonal hole). With the surface area of the crystal of $3.3 \times 5.3\,nm$, we therefore have a percentage of indented surface of 21.8% (hexagonal hole). In order to increase sampling, surface indentations were used simultaneously on both the upper and lower crystal separated from one another by 2 nm in the y direction and 1 nm in the x direction.

3.2.2 Simulation model

The periodic simulation box ($3.3 \times 5.3 \times 5.1\,nm^3$) contained 1500 molecules of water, 84 n-eicosane molecules and 90 cation–anion pairs. The corresponding molar concentration of the salts in solution is 3.12M (mol/L). For statistical accuracy the concentration chosen was ~3 times higher than in the article by Jungwirth et al.[6-7] For direct comparison, we have also performed a few simulations at 1.2 M concentration and they are discussed later in the manuscript. The sodium halide salts dissolved without precipitating at both concentrations. The crystal structure is triclinic ($\alpha = 67.6^0, \beta = 83.9^0, c = 2.544\,nm$) and close to the experimental one ($\alpha = 68.2^0, \beta = 85.7^0, c = 2.743\,nm$).[22,23] The difference in c comes from c being the slab thickness (simulation) and unit cell length (experiment). The eicosane crystal (thickness 2.5 nm) was separated from its periodic image by a water layer (thickness 2.6 nm). This thickness is enough for the water to reach bulk behaviour between the two surfaces. The crystal plane was the xy plane with the inclination of the molecular axes in y direction. In all analyses, z = 0 refers to the surface of the planar crystal defined by the arithmetic mean of the z coordinates of all the unindented surface carbons, so all indentations carry a negative z (Figure 2.5). The hexagonal hole topography on the surface of the crystal was made by switching off the interactions

between the first four carbons (depth ~ 0.5 nm) and the hydrogens connected to them and water.

We used the YASP simulation package.[24] The system was weakly coupled to the desired temperature (298 K) with a relaxation time of 0.2 ps.[25-27] The Cartesian diagonal components of the pressure tensor were coupled separately to an external pressure of 0.1013 MPa with a relaxation time of 0.5 ps.[25-27] Bond lengths were constrained using the SHAKE algorithm.[28] The time step for the leapfrog integration scheme[25-27] was set to 0.002 ps and trajectory frames were written to disk every 1 ps. Non-bonded interactions were evaluated at every time step with a cutoff radius of 0.9 nm using a neighbour list (update every 20 steps, neighbour list cutoff 1.0 nm). The simulations consisted of 1 ns of equilibration and 1 ns data collection. The salt ions have been placed in the bulk water region at random positions at least 1 nm from the interface. Molecular dynamics simulation with a reduced time step of 0.5 fs was performed for 100 ps to remove possible overlaps. The resulting configuration was used as a starting configuration for the equilibration run. After 1 ns of equilibration no drift or deviation of the densities and nonbonded energies were observed. The error bars in the densities and nonbonded energies were in the acceptable limit of ~1 %. The n-eicosane is described by the all-atom OPLS model.[29,30] The OPLS-AA model has been chosen because it produces realistic interactions with the SPC/E[31,32] water model. As a test, we have calculated the free energy of hydration for octane (-9.2 kJ/mol, experimental -9.87 kJ/mol). Water is treated with the SPC/E model.[32] The potential parameters of the electrolytes are shown in Table.1. They have been already shown to give good structural and dynamical properties in aqueous solutions. The article by Koneshan et al.[33] describes the modulation in the structure of the hydration shell around the alkali and the halide ions as a function of the charge and size of the corresponding ions (Table 3.1). Lennard-Jones parameters for interactions between unlike atoms were evaluated using the Lorentz-Berthelot mixing rules,[26] electrostatic interactions were treated with the reaction field approximation,[26] using an effective dielectric constant of 72.

3.2.3 Analysis

The simulations were analysed in terms of the density of water and the ions at and near the interface. We have analysed the local densities by dividing the simulation box into cells of size ($0.4 \times 0.4 \times 0.2\,\mathrm{nm}^3$) and finding the density in each cell. The absolute densities of all the species were normalized by the bulk density of the corresponding species from a separate bulk simulation of water and electrolytes at the same concentration. Since the crystal is not space fixed and has the freedom to diffuse in x and y direction, the analysis grid was attached to the crystal in order to get consistent density distributions over the course of the MD simulation. This was done by fixing grid points to the surface carbon atoms of the crystal. The density distribution (g/cm^3) was evaluated using

$$\rho(\vec{r}) = \frac{< N[\vec{r}, (x - \frac{\Delta x}{2}, x + \frac{\Delta x}{2}), (y - \frac{\Delta y}{2}, y + \frac{\Delta y}{2}), (z - \frac{\Delta z}{2}, z + \frac{\Delta z}{2})] > \mathrm{M_s}}{\Delta x \Delta y \Delta z}. \qquad (3.1)$$

where $\vec{r} = (x, y, z)$ is the centre of the cell, Δx, Δy, Δz are the length of the sides of the cell, $\mathrm{M_s}$ is the molecular weight of the species and $< N[\vec{r}] >$, is the number of water oxygens inside the cell at $\vec{r}$ averaged over the 10^3 trajectory frames.

The concentrations of species have been analysed in two different ways. Firstly they were analysed by cutting the simulation box in the x-z plane and finding the concentrations in the above mentioned grid cells. The concentration (in mol/L) in a grid cell is given by

$$C_1(\vec{r}) = \frac{\rho(\vec{r})}{M_S} \times 10^3 \qquad (3.2)$$

The ion concentrations were also analysed in the direction normal to the interface given by the following ratio

$$C_2(z) = \frac{\mathrm{n_X}(z)}{\mathrm{n_O}(z)} \qquad (3.3)$$

where $n_X(z)$ is the number of ions at a given z and $n_O(z)$ is the number of water oxygen atoms at a given z. This concentration gives the idea of the relative concentration of an ion at the interface and inside the bulk water region.

3.3 RESULTS AND DISCUSSION

3.3.1 Density of water and ions near the hydrophobic surface

Figure 3.1 shows the density profiles within the liquid phase obtained by averaging over the whole simulation. The absolute density of a given species is divided by the corresponding density in bulk solution. The bulk densities of Na^+ ion in NaF and NaI bulk solutions are 0.071 g/cm^3 and 0.061 g/cm^3, respectively. The bulk densities of F^- and I^- in NaF and NaI solutions are 0.062 g/cm^3 and 0.33 g/cm^3, respectively. This way of scaling is different form the scaling done by Jungwirth et al.[6,7] as they scale the absolute densities of all species by the bulk *water* density. A difference between the sodium cation and fluoride anion on one hand, and the heavier iodide anion on the other hand, is evident in the density profiles. In case of the NaF solution near the planar surface, Figure 3.1(a), both ions stay away from the surface, leaving an ion-free layer roughly 0.35 nm thick (i.e. approximately the diameter of one water molecule). Due to the presence of the ion-free layer, the fluoride and sodium ions are pushed into the bulk water region and, therefore, have $\rho(z)/\rho_b > 1$ at distances ≥ 0.8 nm. In contrast, iodide ions, (Figure 3.1(b)), occupy a significant portion of the interface. They also drag a certain fraction of sodium cations to the interface showing a formation of a double layer near the interface. The ratio of the densities of ions, in Figure 3.1(b), is below one in the bulk water region (0.8 nm) implying that the ions favour the interface. One of the interesting differences in case of NaI electrolyte, between our simulations and the one performed by Jungwirth et al.[6,7] is the presence of a double peak at the water/ hydrophobic surface interface rather than a single peak observed in the water/vapour interface by Jungwirth et al. This is not an effect of concentration: we have performed a simulation of a solution of 1.2 M NaI in water near the planar surface. It shows the same double-peak structure (data not shown).

However, a separate simulation of NaI solutions at water/vacuum interface does not show the double peak (data not shown). The peak splitting (~ 0.1 nm) of the iodine is possibly due to the corrugation of the hydrophobic surface, which leads to two iodine populations near the surface.

Figure 3.1(a) and 3.1(b) also show the density as a function of z of pure water without salt. Here it is evident, that in the NaF solution water wets the surface nearly like pure water (Figure 3.1(a)). In the NaI solution there is less water at the surface than in pure water, as it is being displaced by the iodide.

The density profiles of NaF and NaI electrolyte solutions near the surface with the hexagonal hole, Figure 3.1(c) and 3.1(d), show that fluoride ions stay primarily in the bulk water region, whereas iodide ions enter the hole. In case of the NaF electrolytes, the sodium and fluoride ions can come nearer to the corrugated surface ($z = 0$) than to the planar crystal, due to the presence of the hole. However their relative density at $z \sim 0$ nm is small, Figure 3.1(c). Iodide, on the other hand, enters the hole, albeit at a small concentration ($\rho(z)/\rho_b < 0.2$), Figure 3.1(d)), and it takes some Na^+ with it for electroneutrality. The water density profile for the NaF solution is almost unchanged compared to pure water (Figure 3.1(c)). For the NaI solution one notes a displacement of water above the surface ($z > 0.1$ nm) similar to the behaviour at the planar surface (Figure 3.1(b)). The amount of water entering the hole is however, unchanged also for NaI solutions. The low ion content in the hole cannot displace much water.

3.3.2 Preferential interaction coefficients calculated from the density profiles

We convert the density profiles from the previous section to preferential interaction coefficients and we estimate the infinitesimal free energy changes of the hydrophobic surface up on addition of solute (NaF or NaI) at the concentration of 3.12 M for the NaI and NaF salts. This is not a calculation of the free energy change due to a finite concentration of salt, which would require work beyond the scope of this contribution. Still these results show trends in the hydrophobicity of both the surfaces which su The

depletion or enhancement in the concentration of a salt (*X*) near a macromolecule in general or a hydrophobic surface (*S*, in this contribution) can be quantified by the preferential interaction coefficients Γ.[34] They[34] relate the change of the excess chemical potentials of the macromolecule/surface to changes in the chemical potentials of water(*W*) and salts through the Gibbs Duhem like relationships.[34]

$$\begin{aligned} d\mu_S &= -\Gamma_{SX} d\mu_X \\ d\mu_S &= -\Gamma_{SW} d\mu_W \end{aligned} \tag{3.4}$$

where μ refers to the chemical potential. If the preferential interaction coefficient is positive the salt accumulates at the surface. Conversely, if the preferential interaction coefficient is negative the ions are excluded from the surface.[34]

For an infinite planar surface in contact with a solution of water and salt, the relation between the changes in the free energy of the surface dG_S and the changes in the salt and water chemical potentials is given by[34]

$$\begin{aligned} dG_S &= -\int_0^\infty [N_X(z) d\mu_X + N_W(z) d\mu_W] dz \\ &= -\Gamma_{SX} d\mu_X . \\ \Gamma_{SX} &= \int_0^\infty \left(N_X(z) - N_W(z) \frac{N_X(\infty)}{N_W(\infty)} \right) dz \\ &= \int_0^\infty \Gamma_{SX}(z) dz \end{aligned} \tag{3.5}$$

N(z) denotes the number density of particles as a function of *z* from the surface (∞ denotes the bulk region away from the interface). The preferential interaction coefficient Γ_{SX} for an electrolyte is calculated as the arithmetic mean of the contributions from both ions. The variation in the $\Gamma_{SX}(z)$ as a function of distance pport our previous findings. from the surface(z) is shown in Figure 3.2(a-d) for all cases. $N(\infty)$ is calculated by averaging the number density of species (water/salt) for z > 1.2 nm. The integral in equation.3.5 was calculated between the limits z = 0 and z = 1.8 nm using the trapezoidal rule and 500 meshpoints.

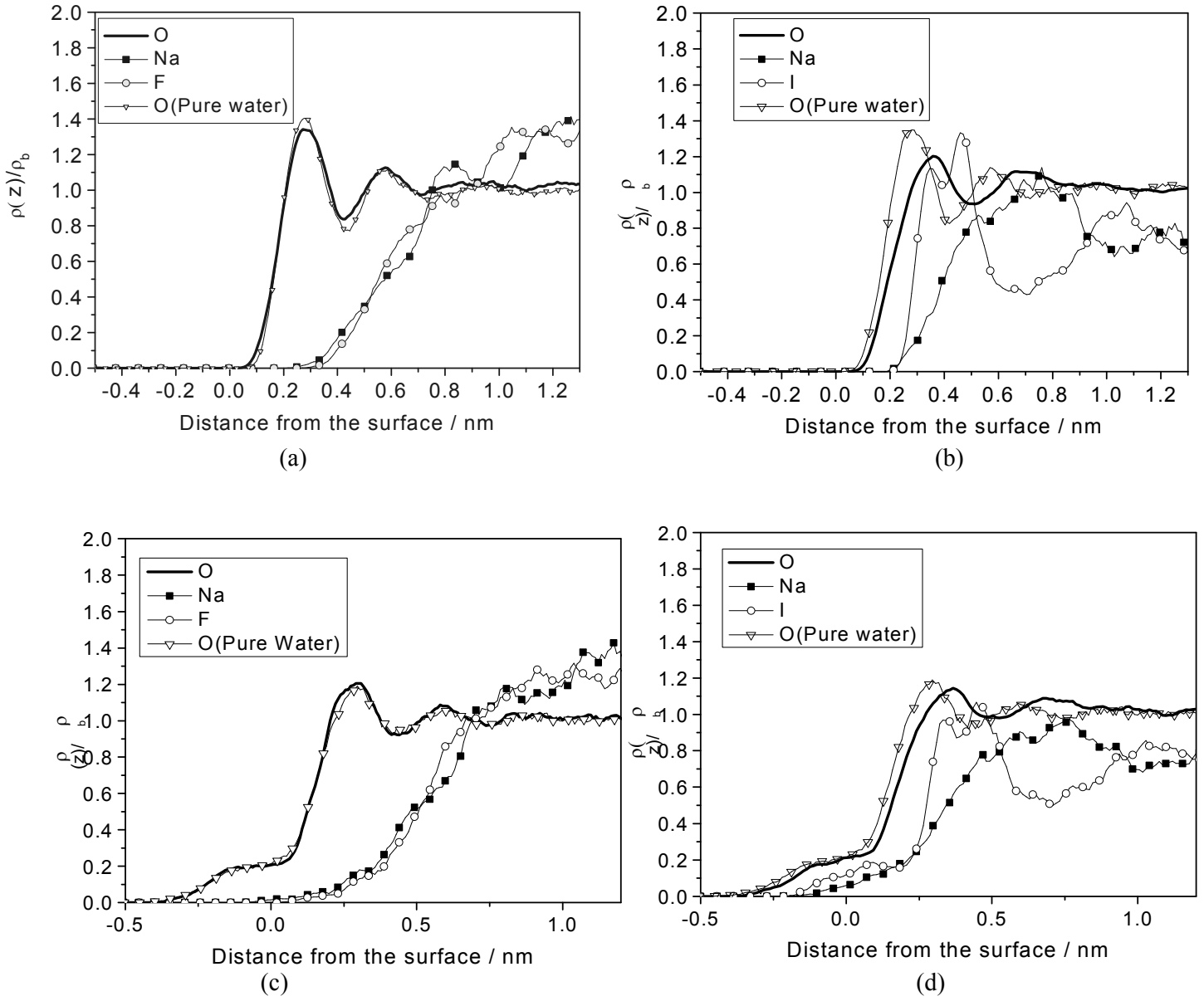

Figure 3.1 Number densities, ρ(z), of water oxygen atoms and ions plotted v/s distance from the surface in the direction normal to the interface (z), normalized by the densities of species in bulk solution at the same concentration ρ_b. (a) NaF solution near the planar surface, (b) NaI solution near the planar surface, (c) NaF solution near the surface with the hole, (d) NaI solution near the surface with the hole. For comparision the water densities of pure water also shown.

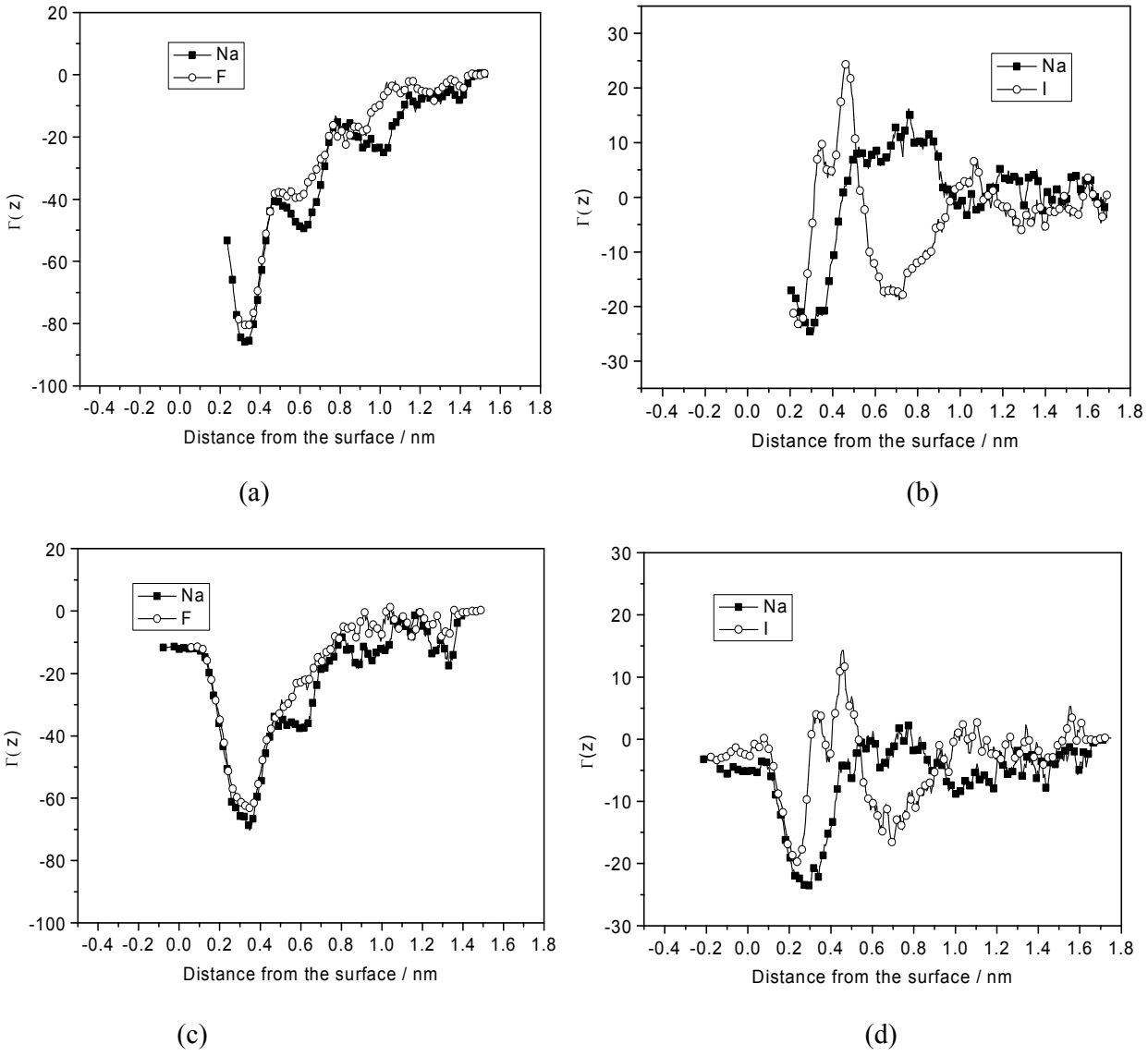

Figure 3.2. *Γ(z)* (defined in eq.1) as a function of z. a) NaF solution near the planar surface, (b) NaI solution near the planar surface, (c) NaF solution near the surface with the hole, (d) NaI solution near the surface with the hole.

The preferential interaction coefficients, Γ, calculated from equation (3.5), are –32.6 and the –2.15 for the NaF and NaI solutions in contact with a planar surface and –30.1 and –9.14 for the for NaF and NaI solutions, respectively, for the surface with the hole.

To calculate the infinitesimal change in the free energy of the surface due to the addition of salt from equation.(3.5), we need the change in the chemical potential of the solute. The following Gibbs-Duhem equation applies

$$d\mu_X = -\frac{x_W}{x_X} d\mu_W \tag{3.6}$$

where x denotes the mole fraction. The change in the chemical potential of water $d\mu_W$ in the solution, upon adding a solute, is approximated by

$$\Delta\mu_W = k_B T \ln(a_W) \tag{3.7}$$

where a_W is the activity of water. If the mole fraction of water is high, the activity is approximately equal to the mole fraction of water x_W. In our case, the mole fraction of water, considering the ions separately is ~ 0.9 (1500/1680). Therefore the change in the chemical potential for water upon adding salt can be approximated as

$$\Delta\mu_W \approx k_B T \ln(x_W) \tag{3.8}$$

Substituting equation (3.8) in equation (3.4) we can calculate the changes in chemical potential of the salt. Therefore from equation (3.5) and using the values of the preferential interaction coefficients, previously calculated, the changes in the surface free energy ΔG_s per unit area of the hydrophobic surface $(2 \times 3.3 \times 5.3\,\mathrm{nm}^2)$ are (1) 6.93 mN/m and 0.45 mN/m for NaF and the NaI solution at the planar surface and 6.40 mN/m and 1.94 mN/m for NaF and NaI solution at the surface with the hole. The changes in the surface tension of the water/water vapor interface due to addition of NaF and NaI in water at 1.2 M concentration have been calculated to be 3.6 mN/m and 1.2 mN/m, respectively.[35]

The values of all Γ_{SX} are negative, indicating a net depletion of both salts near both surfaces and leading to an increase of surface free energy (and hence hydrophobicity)

upon further addition of salt. This is at first surprising, since ion densities show an accumulation of iodide ions at hydrophobic interfaces (Figure 3.3(b) and 3.3(d)). A look at the integrands $\Gamma_{SX}(z)$ of equation (3.5) for the individual ions helps understand the reasons (Figure 3.2). Figures 3.2a and 3.2c show that NaF is repelled from both surfaces and that Na^+ and F^- have similar density profiles. Both ions contribute to the negative integral in the same way. In contrast the behavior of Na^+ and I^- is very different (Figures 3.2b and 3.2d). Iodide has a strong $\Gamma_{SI}(z)$ maximum immediately at the planar surface ($z \leq 0.5$ nm) followed by a depletion layer (0.5 nm < z < 1.0 nm), Figure 3.2(b). Their contributions to the integral amount to a net depletion $\Gamma_{SI} = -4.74$. Sodium ions have a high density where the I^- density is low (0.5 nm < z < 1.0 nm). The enrichment region compensates the Na^+ depletion layer at the surface (z < 0.5 nm) and the Γ_{SNa} of the Na^+ has a small positive value. Comparing to the surface with the hole (Figure 3.2(d)) we note that for both ions, the region of negative $\Gamma_{SX}(z)$ are almost unchanged. The positive peaks of $\Gamma_{SNa}(z)$ have, however decreased in height. This leads to a reduction of Γ_{SNa} (z) to -11.65 and Γ_{SI} (z) to –6.64, respectively.

3.3.3 Density profiles, concentration profiles of water and ions and the radial distribution function of water near the interface.

Figure 3.3 shows the concentration plots, $C_I(\vec{r}\,)$, in a yz slab of thickness $\Delta x = 0.5$ nm positioned at $x_1 = -0.25$ nm and $x_2 = 0.25$ nm relative to the central reference carbon atom inside the hole. This slab cuts vertically through the surface and the hole if present. For the planar crystal the reference carbon is the central carbon at the surface of the slab. While Figure 3.3(a) shows that the fluoride ions stay away from the interface leaving a low density region near the hydrophobic surface, Figure 3.3(b) shows that the concentration of the iodide ions is higher at the interface than in the bulk. Figure 3.3(a) and (b) thus echos Figure 3.1(a) and 3.1(b).

The situation becomes more complex when going from the planar surface to the hole geometry [Figure 3.3(c) and 3.3(d)]. Fluoride still avoids the surface and iodide is still attracted to it. For fluoride, however the concentration is now highest at a distance from the surface ($z \approx 0.8$ nm) but above the hole, Figure 3.3(c). This is mirrored in the Na^+ concentration, which has a maximum in the same region (not shown), for reasons of electroneutrality. The diffusion coefficients of all species, which are discussed below in section 3.3.3 show that there is no amorphous aggregate of ions in this region, the solution still being a liquid. The region above the hole is simply the area furthest away from any surface, so fluoride ions congregate here trying to avoid surface.

For iodide, the hole has more obvious consequences. Iodide ions experience the bottom of the hole as just another hydrophobic surface to which they are attracted. They are found in the centre of the hole, whereas they avoid the corners and the vertical side walls. This is possible due to water structure at the edges or confinement effects. The concentration of iodide found in the hole is too low, however, for the hole to be viewed as an iodide trap.

Figure 3.4 shows the water density, $\rho(\vec{r})$, in the planar surface and the hexagonal hole case. For both surface geometries, the water density at the interface is higher for NaF, Figure 3.4(a) and (c), than for NaI Figure 3.4(b) and 3.4(d). The presence of the bulky iodide ions at the interface leads to a lower density of water at the interface and inside the hole. Fluoride, on the other hand avoids the surface. The interfacial water distribution is almost identical for the NaF solution, Figure 3.4(c), and pure water, Figure 3.4(e).

One technical difficulty in the density and concentration plots for ions should be mentioned is the usage of a coarser grid for the ion density (Figure 3.4) ($0.6 \times 0.6 \times 0.4\,\mathrm{nm}^3$) compared to that of water, Figure 3.5 ($0.2 \times 0.2 \times 0.1\,\mathrm{nm}^3$). The reason for using a coarser grid is purely statistical, as the number of ions is much lower than that of water molecules. Together with the interpolation scheme of the plot software this leads to an apparently larger hole sizes in the ion concentration plots

(Figure 3). In Figure 3.5, the ion concentrations are shown in a different normalization. They are divided by the local water concentration (i.e. $C_2(\vec{r}\,)$ = $n_X(\vec{r})/n_O(\vec{r})$) in order to highlight changes in the relative composition. Comparing the raw concentrations (Figure 3.3) and the renormalized composition (Figure 3.5), one notes the quantitative similarity of all ion concentrations near the planar interface (subfigures a and b). Apart from a prefactor, the profiles are similar, indicating a small change of the ion/water ratio as a function of z. The situation is different in the hole geometry (subfigures c and d): For NaI there is a significant enhancement of the ion/water ratio inside the hole (subfigures d), and even for NaF there is a small but visible increase (subfigures c). This indicates that while the concentration of ions inside the hole is reduced with respect to their bulk concentration (Figures 3.3 (c), (d)), the relative density of water is even more reduced.

This is also evident in the hydration number of iodide, Figure 3.6. We define the hydration number of an iodide ion as the number of oxygen atoms, which are within its first hydration shell defined by the first minimum of the iodine-oxygen radial distribution function (RDF). The RDF exhibits a maximum at 3.7-4.0 Å and a first minimum between 4.0-4.5 Å. The hydration number at a given z is found by integrating the RDF till r = 0.43 nm. In Figure 3.6, the mean iodide hydration numbers in 0.1 nm thick layers parallel to the interface are shown v/s the distance z from the closest surface. The iodide hydration number near the flat interface is between 3.6 and 3.8. In the bulk it is between 4.0 and 4.2. For the hexagonal hole case, the hydration number inside the holes is between 3.4-3.6. Iodide ions inside the holes have on average about half a water molecule less than in the bulk. At the bottom of the hole (~ 0.25 nm) the hydration number abruptly falls to below 3, so also here an iodide has approximately ½ water molecule less than an iodide immediately at the planar surface (+0.2 nm).

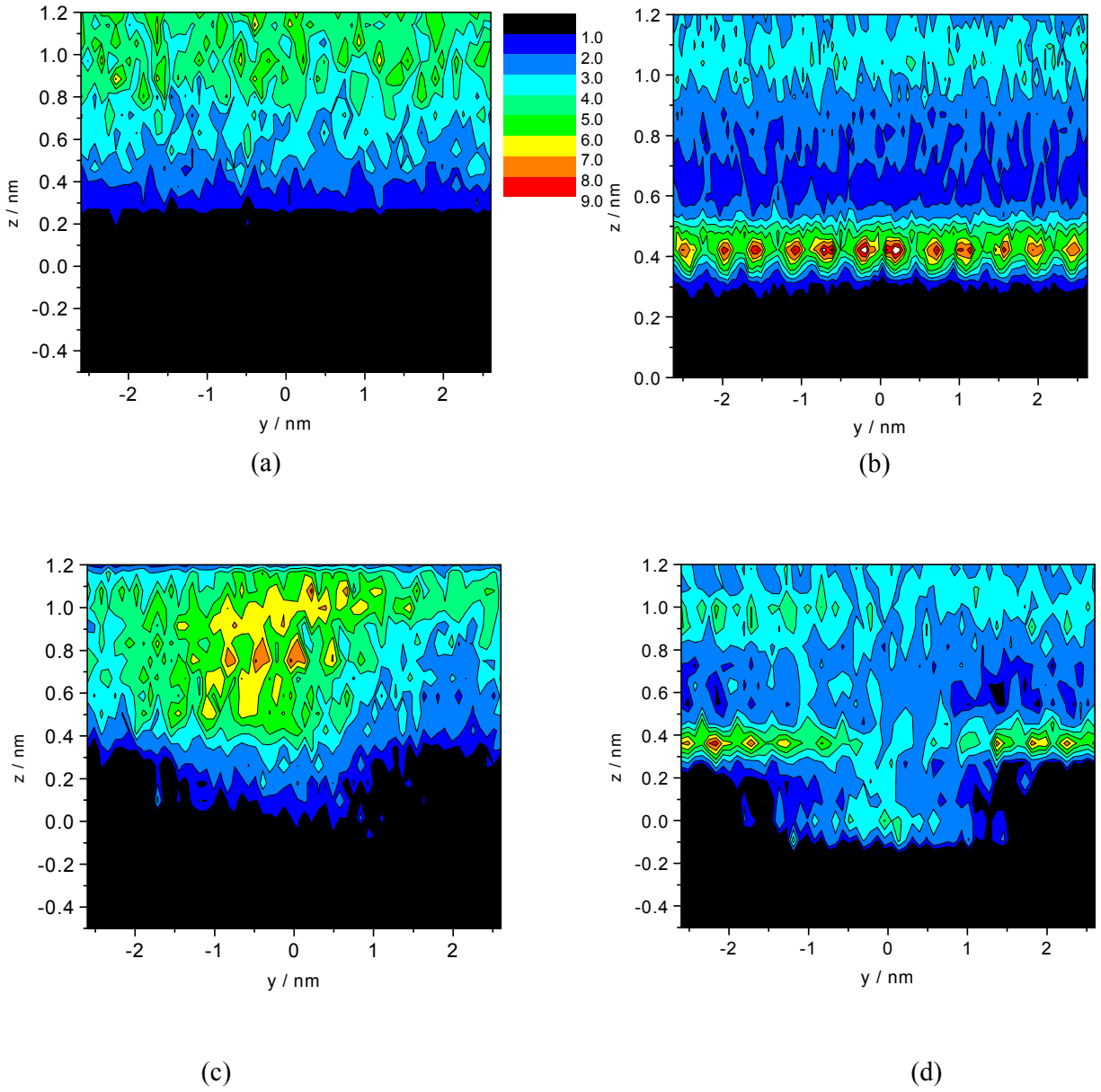

Figure 3.3 a-d Concentration $C_I(\vec{r})$, in mol/l of the anions in a vertical (yz) slab of thickness Δx = 0.5 nm cutting through the centre of the hole (surface with hole). (a) NaF solution near the planar surface, (b) NaI solution near the planar surface, (c) NaF solution near the surface with the hole, (d) NaI solution near the surface with the hole.

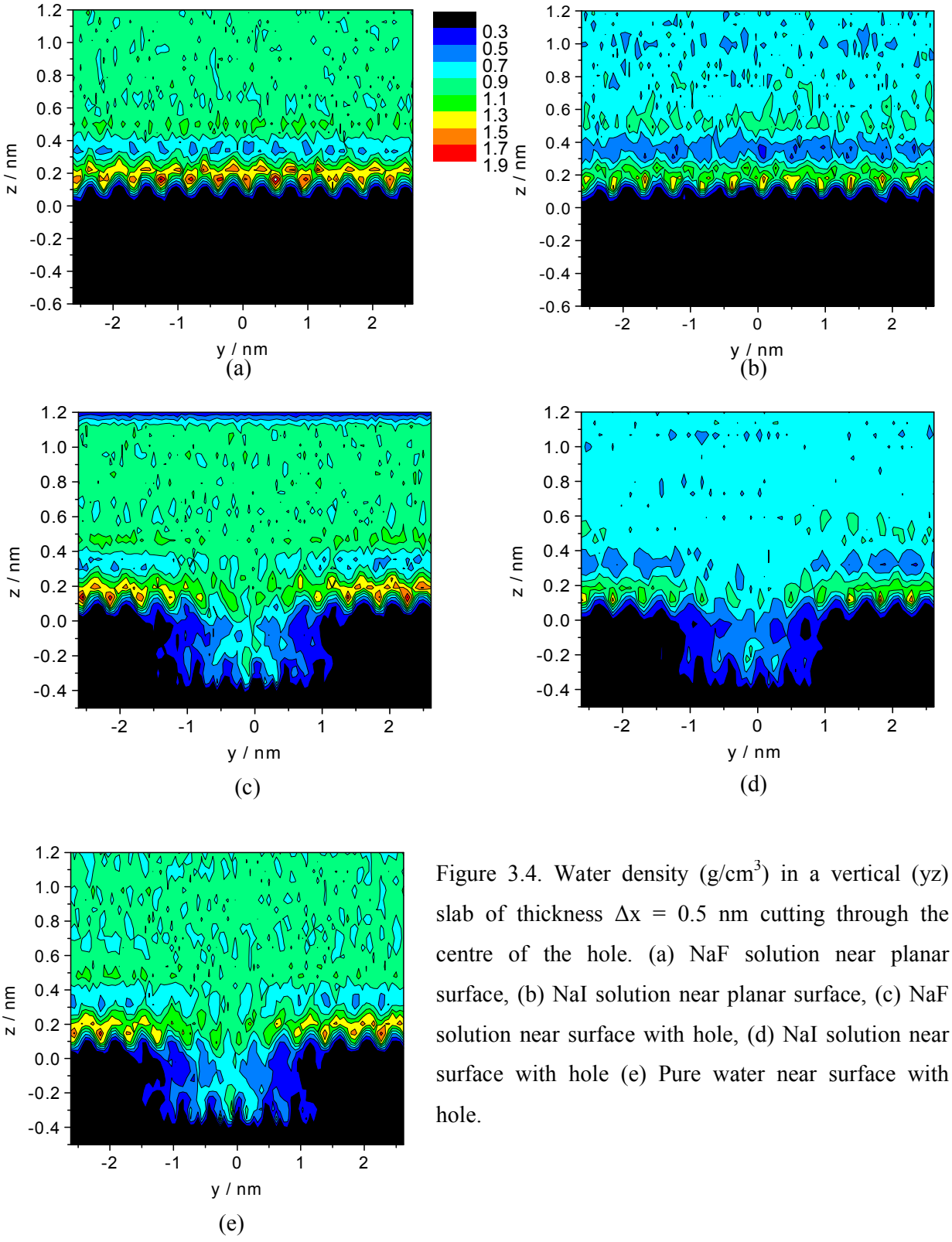

Figure 3.4. Water density (g/cm^3) in a vertical (yz) slab of thickness Δx = 0.5 nm cutting through the centre of the hole. (a) NaF solution near planar surface, (b) NaI solution near planar surface, (c) NaF solution near surface with hole, (d) NaI solution near surface with hole (e) Pure water near surface with hole.

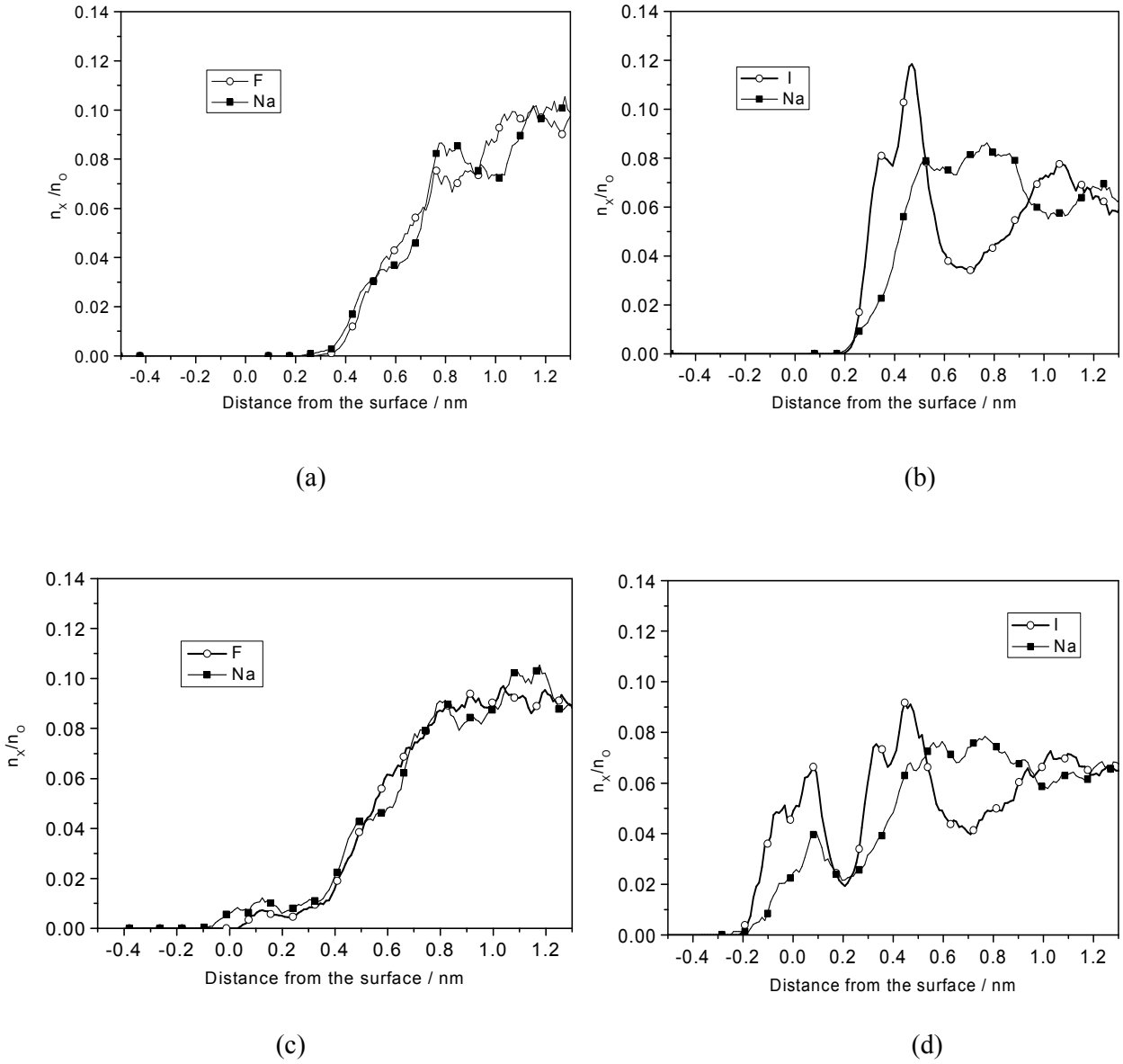

Figure 3.5. Ion Concentration (ratio of number of ions to the number of oxygen atoms) versus the distance from the surface. (a) Fluoride and sodium concentration near the planar surface. (b) Iodide and sodium concentration near the planar surface. (c) Fluoride and sodium concentration near the surface with hole. (d) Iodide and sodium concentration near the surface with hole.

Figure 3.7(a) and (b) shows the radial distribution function between surface carbons and water molecules. Surface carbons are the methyl carbons (C_1) at the chain ends for the planar surface. For the structured surface, also the C_2 to C_4 carbons lining the hole count as surface carbons. For the NaI solution, the number of contacts between the water and the surface carbons have visibly decreased compared to the NaF solution and pure water for both surface topographies. In contrast there is practically no difference between the NaF solution and pure water. By integrating the radial distribution function till the first minimum at r = 0.5 nm we find the number of contacts between the surface carbons with the water molecules. The number of contacts the hydrophobic surfaces make with water is shown in Table 3.2. The presence of iodide reduces the water-surface contacts by approximately 10% for both surface topographies, whereas NaF slightly increases the number of water-surface contacts.

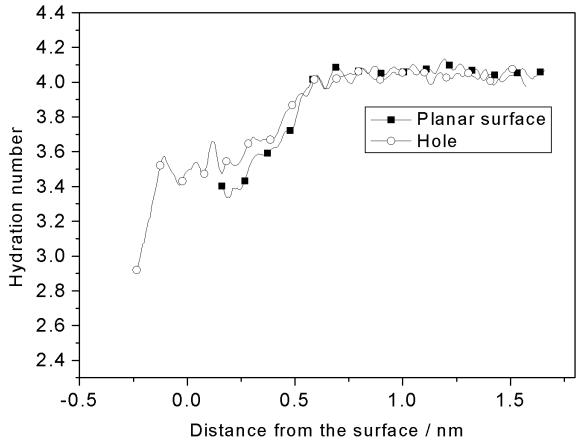

Figure 3.6: Average hydration number of iodide ions (water molecules in first hydration shell; for definition, see text) as a function of their distance from the surface.

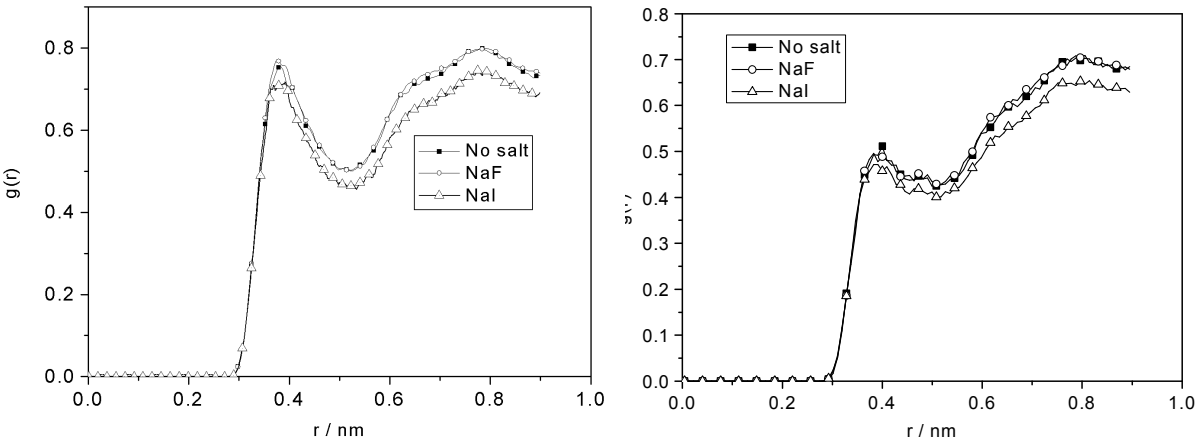

Figure 3.7: Radial distribution function of the surface carbons and water oxygen atoms (a) for the planar surface, (b) for the surface with the hexagonal hole.

Table 3.2. Number of contacts between the water and surface carbons per water molecule.[a]

Electrolyte	Planar surface	Hexagonal hole
NaI	0.38 (3.45)	0.25 (2.77)
NaF	0.46 (4.11)	0.29 (3.25)
Pure water	0.45 (4.00)	0.28 (3.21)

[a] In parentheses the number of contacts between the water and surface carbons per surface carbon atom is shown.

3.3.4 Orientation of hydrogen bonds

We show the orientation of water-water and ion-water hydrogen bonds in the electrolyte solutions as a function of z in Figure 3.8 and Figure 3.9. The definition of hydrogen bonding is given in the caption of Figure 3.8. We define a vector pointing from the oxygen atom of the water molecule acting as the hydrogen bond donor to the atom acting as a hydrogen bond acceptor, i.e. a water oxygen or an anion. Figure 3.8(a) shows the hydrogen bond orientation of the water molecule in two different ways: First as the cosine of the angle θ between this vector and the surface normal of the slab $\langle \cos(\theta) \rangle$. A positive value of $\langle \cos(\theta) \rangle$, means that the hydrogen bond vector points away from the surface. The orientation is secondly measured by an order parameter $\langle S^2 \rangle$ of the same angle θ, in Figure 3.8(b).

$$\langle S^2 \rangle = 0.5 < 3\cos^2\theta - 1 > \tag{3.9}$$

A positive value of $\langle S^2 \rangle$ implies that the hydrogen bonds prefer to align perpendicular to the surface, it is negative when the preferred alignment is parallel to the surface. It is zero at the magic angle or for random orientations.

The ion densities (cf. Figure 1) have a direct influence on the orientation of water-anion hydrogen bonds (Figure 3.8). Close to the surface (< 0.5 nm) they point away from the surface, reflecting the fact some water molecules approach the surface more closely than the ions (Figure 3.8a). This is true for both anions and both surfaces. There are however differences between fluoride and iodide, which are best seen comparing the NaF and NaI curves for the planar interface. Fluoride avoids the surface, so water-fluoride hydrogen bonds point upwards (away from the surface), and $\langle \cos(\theta) \rangle$ decays uniformly. In contrast, iodide prefers the surface, which leads to a region of negative $\langle \cos(\theta) \rangle$ between 0.45 and 0.75 nm, indicating that there is a layer of water molecules above the iodide layer, whose water-iodide hydrogen bonds point

downwards (towards the surface). The fact that there is at all a water layer (< 0.45 nm) with hydrogen bonds pointing upward towards iodide is due to the large diameter of this anion: Although it prefers the surface it cannot get as close as a water molecule. Beyond 0.75 nm, $\langle \cos(\theta) \rangle$ for NaI is again positive. This is explained by a secondary iodide layer at ≈ 1.0 nm, visible in Figure 3.1b and 3.2b. The surface topography does not influence the hydrogen-bond orientations much except that there is less order inside the hole, since the vertical hole walls influence the hydrogen bond orientation, too.

The order parameter $\langle S^2 \rangle$ (Figure 3.8b) are consistent with this picture. At close range (< 0.45 nm), the water-fluoride H bonds are more perpendicular than the magic angle whereas the water-iodide H-bonds are more parallel due to the position of the anions (fluoride away from the surface, iodide in the surface layer).

The water-water hydrogen bond orientation, defined by the order parameter $\langle S^2 \rangle$, for both the NaF and NaI solutions shows a preferential parallel orientation near the interface, which is a characteristic of hydrophobic surfaces, Figure 3.9(a) and (b).[36] In the bulk region (> 0.5 nm) the water-water hydrogen bonds show no preferred orientation. Figure 3.9(a) shows that the water-water hydrogen bonding has a parallel arrangement near (< 0.5 nm) the planar surface. In the hole case, Figure 3.9(b), there is a double minimum structure at z = 0.3 nm (at the interface) and z = -0.2 nm inside the hexagonal hole probably due to the competing influence of the hole walls. In the NaI solution, there is a stronger parallel alignment of hydrogen bonds than in the NaF solution or in pure water near both surfaces, Figure 3.9(a) and 3.9(b). This orientation of the water-water hydrogen bonds is different from previous results[6-7] observed for the hydrogen bonding orientation of water. They show that in case of NaI electrolytes near the vacuum interface the hydrogen bond orientation is slightly disrupted and the orientation of the water-water hydrogen bond vectors point toward the bulk.

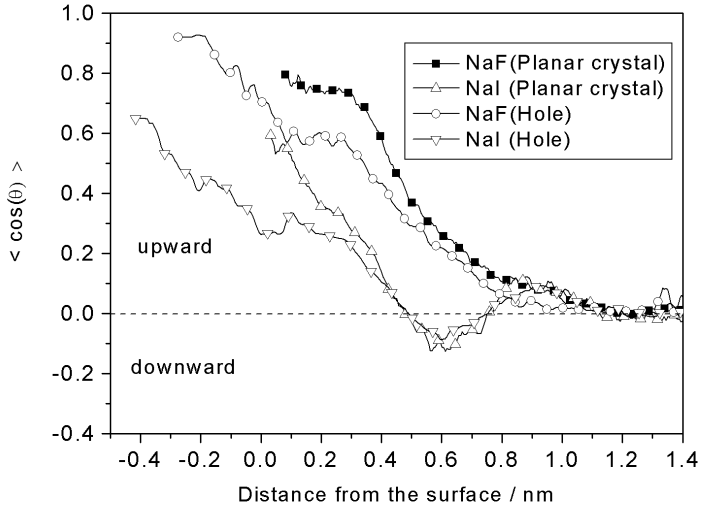

(a)

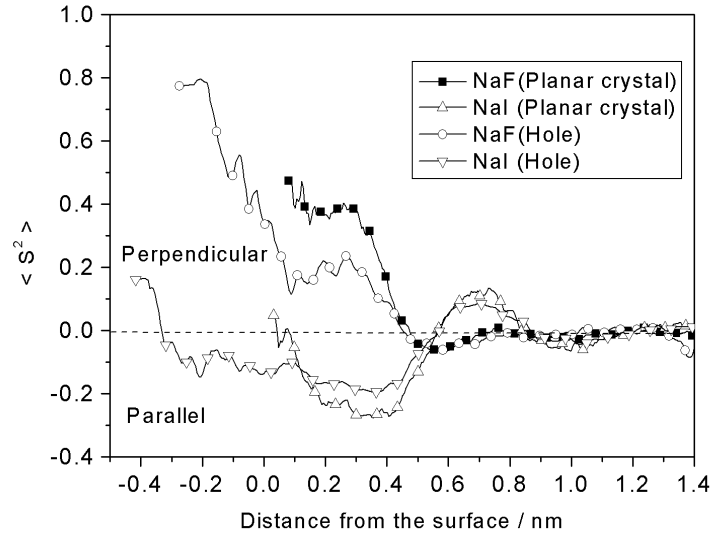

(b)

Figure 3.8. Orientation of the water anion hydrogen bonds. A water molecule is considered hydrogen-bonded to a hydrogen bond acceptor, A, if the O-A distance is less than a cutoff value (3.5 Å for water-water, 3.3 Å for water-fluoride, 4.3 Å for water-iodide), and the angle between O-A axis and the O-H bond is less than 30^0. The orientation is reported as (a) the cosine of the angle between the vector from the water oxygen to the acceptor atom A and the surface normal, and as (b) the second Legendre polynomial $\left\langle S^2 \right\rangle$ of the cosine of the same angle.

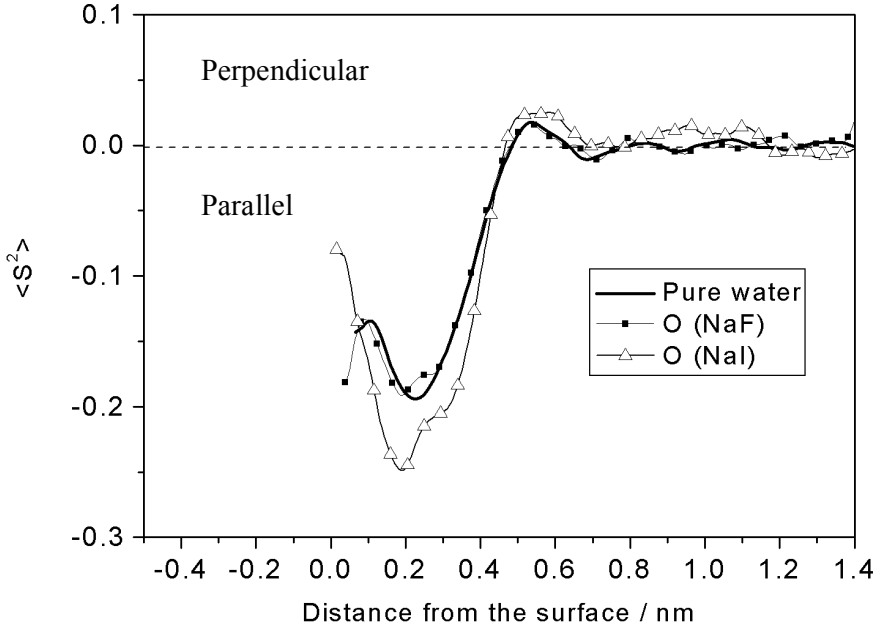

(a)

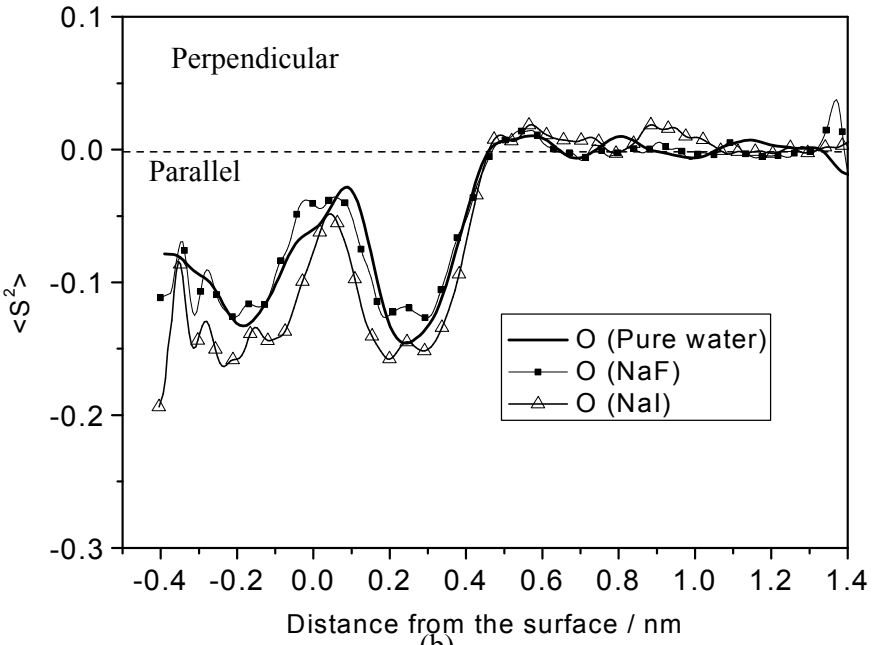

(b)

Figure 3.9: Orientation of water-water hydrogen bonds. (a) Near the planar surface (b) Near the surface with the hole. The definition of hydrogen bonds and orientations is the same as in Figure 10.

3.3.5 Diffusion near the interface

Although the emphasis of this article is on the static distribution of water and ions near the interface, we have also calculated the parallel diffusion coefficient $D_{\|}$ of all species in the different cases. (The perpendicular diffusion coefficient $D_{\perp} = D_{zz}$ cannot be evaluated, since the displacement is bounded by the alkane slabs.) The Cartesian components of the diffusion coefficients were determined by calculating the centre-of-mass mean-square displacements of the species and determining the slope from the linear region between 600 ps and 1 ns during the production run. The parallel diffusion coefficient was calculated from the components as

$$D_{\|} = 0.5 \, (D_{xx} + D_{yy}) \qquad (3.10)$$

The diffusion coefficients are of the order of 10^{-5} cm^2/s showing that all systems are liquid, Table 3. The anions move faster than the cation and I^- is faster than F^-, all in line with the experimental and simulation data.[37] The surface topography has a minor influence, if any: corresponding diffusion coefficients for the planar and the hole geometries agree to within their error limits. This means that although I^- is attracted to the surface, this attraction does not inhibit sideways translation, so the residence times at surface sites must be short.

3.4 CONCLUSIONS

This contribution has studied the behaviour of aqueous salt solutions near a flat and a nanostructured hydrophobic surface. In many ways, the distribution of the ions follows the pattern found near the vacuum interface: Small anions (F^-) avoid the surface whereas large anions (I^-) prefer the surface. The cations (Na^+) adapt to the anion distribution: For NaF solutions, the cation follows the anion into the bulk, for NaI solutions the Na^+ form a layer above the interfacial layer of I^-. The distribution of water is dictated by the salt distribution. As fluoride avoids the interface, the hydrophobic surface is in contact with a thin layer of almost pure water and, thus, the water density profile near the surface is very much that of pure water. Iodide, in contrast, is surface-active and displaces water molecules from the first layer.

The density profiles were used to calculate the preferential interaction coefficients. The surface free energy increment of the planar surface and the indented surface per unit area were found to be positive due to the presence of the salts (NaF and NaI). The

Table 3.3. The diffusion coefficients (in 10^{-5} cm^2/s) parallel to the surface $D_{||}$.

System	Na^+	F^-	I^-	H_2O
Planar Crystal				
Pure water	—	—	—	16.2 ± 0.39
NaF solution	4.9 ± 1.7	5.1 ± 0.9	—	10.3 ± 0.5
NaI solution	8.2 ± 2.0	—	11.5 ± 1.5	12.8 ± 0.5
Hexagonal hole				
Pure water	—	—	—	16.5 ± 0.31
NaF solution	3.9 ± 0.1	2.9 ± 1.0	—	7.0 ± 0.15
NaI solution	9.9 ± 2.2	—	10.0 ± 3.1	12.7 ± 0.65

[(a)] The average diffusion coefficients were obtained as $D_{||} = ½ (D_{xx} + D_{yy})$, their errors as $| D_{xx} – D_{yy} |$.

salts ions are preferentially excluded from the hydrophobic surface increasing the surface free energy of the hydrophobic interface. The water molecules are oriented to form hydrogen bonds with the ions and this effect dominates over the orientational ordering due to the surface.

The introduction of a nm-size indentation into the hydrophobic surface has differentconsequences for the two solutions. As fluoride, like Na^+, wants to be hydrated, it avoids the hole. Inside the hole, there is even less fluoride than above the flat surface. The low water density creates a bad hydration environment for fluoride. For iodide the situation is different. Iodide accumulates at the hole bottom qualitatively in the same way as it accumulate against the flat surface. Still, there is no enrichment of iodide inside the holes. The low water density and the spatial constraint preclude this. Therefore, the holes cannot be viewed as traps for large anions. The finding is corroborated by the ion diffusion coefficients, which are virtually unchanged between the planar and the nanostructured surface.

The fact that surface indentations do not act as ion entrapments has important technological implications: if they did cause an increased binding of ions to the interface they would effectively bestow negative charge on the surface, and a negative surface would lose some of its hydrophobic character. Such worries can be dispelled by the present results.

References

(1) Adam, N. K. The Physics and Chemistry of Surfaces; Oxford University Press: London, **1941**.

(2) Bikerman, J. J. Surface Chemistry: Theory and Applications; Academic Press: New York, **1958**.

(3) Chattoraj, D. K.; Birdi, K. S. Adsorption and the Gibbs Surface Excess; Plenum: New York, **1984**.

(4) Knipping, E.; Lakin, M. J.; Foster, K. L.; Jungwirth, P.; Tobias, D. J.; Gerber, R. B.; Dabdub, D.; Finlayson-Pitts, B. J. *Science* **2000**, *288*, 301.

(5) Randles, J. E. B. *Phys. Chem. Liq*. **1977**, *7*, 107.

(6) Jungwirth, P.; Tobias, D. J. *J. Phys. Chem. B* **2001**, *105*, 10468.

(7) Jungwirth, P.; Tobias, D. J. *J. Phys. Chem. B* **2002**, *106*, 6361.

(8) Tobias, D. J.; Jungwirth, P.; Parrinello, M. *J. Phys. Chem*. **2001**, *114*, 7036.

(9) Garrett, B. C. *Science* **2004**, *303*, 1146.

(10) Dang, L. X.; Chang, T. M. *J. Phys. Chem. B*, **2002**, *106*, 235.

(11) Ayotte, P.; Nielsen, S. B.; Weddle, G. H.; Johnson, M. A.; Xantheas, S. S. *J. Phys. Chem. A*, **1999**, *103*, 10665.

(12) Seinfeld, J. H. *Science*, **2002**, *288*, 285.

(13) Caldwell, J.; Dang, L. X.; Kollman, P. A. *J. Am. Chem. Soc*, **1990**, *112*, 9144.

(14) Perera, L.; Berkowitz, M. L. *J. Chem. Phys*, **1991**, *95*, 1954.

(15) Hu, J. H.; Shi, Q.; Dandroits, P.; Worsnop, D. R.; Zahniser, M. S.; Kolb, C. E. *J. Phys. Chem*. **1995**, *99*, 8768.

(16) Bhatt, D.; Newmann, J.; Radke, C. J. *J. Chem. Phys. B.* **2004**, *108*, 9077.

(17) Kalra, A.; Tugcu, N.; Cramer, S. M.; Garde, S. *J. Phys. Chem. B.* **2001**, *105*, 6380.

(18) van der Vegt. N. F. A.; van Gunsteren. W. F. *J. Phys. Chem. B*, **2004**, *108*, 1056

(19) van der Vegt. N. F. A.; Trzesniak, D.; Kasumaj, B.; van Gunsteren. W. F. *ChemPhysChem*, 2004, *5*, 144.

(20) Pal, S.; Müller-Plathe, F.; Weiss, H.; Keller, H. Submitted to *Langmuir.*

(21) Nyburg, S. C.; Potworowski, J. K.; *Acta Cryst*. **1973**, *B29*, 347.

(22) Waheed, N.; Lavine, M. S.; Rutledge, G. C.; *J. Chem. Phys*, **2001**, *116*, 2301.

(23) Small, D. M.; The Physical Chemistry of Lipids: From Alkanes to *Phospholipids.* Plenum, New York, **1986**, 183.

(24) Müller-Plathe, F. *Comput. Phys. Commun*. **1993,** *78*, 77

(25) Allen, M. P.; Tildesly, D. J. *Computer simulation of liquids*; Clarendron Press: Oxford, **1987**.

(26) Frenkel, D.; Smit, B. *Understanding Molecular Simulation*; Academic Press, San Diego, **2002**.

(27) Jensen, F.; *Introduction to Computational Chemistry*, Wiley VCH, Chichester, **1998**.

(28) Ryckaert, J. P.; Ciccotti, G.; Berendsen, H. J. C. *J. Comp. Phys*. **1971**,

(29) Duffy, E. M.; Jorgensen; W. L. *J. Am. Chem. Soc*. **2000**, *122*, 2878.

(30) Kaminski, G.; Duffy, E. M.; Matsui, T.; Jorgensen, W. L. *J. Phys. Chem*. **1994**, *98*, 13077.

(31) Berendsen, H. J. C.; Postma, J. P. M.; van Gunsteren, W. F.; DiNola, A.; Haak, J. R. *J. Chem. Phys*. **1984**, *81*, 3684.

(32) Berendsen, H. J. C.; Grigera, J. R.; Straatsma, T. P. *J. Phys.Chem*. **1987**, *91*, 6269.

(33) Koneshan, S.; Rasaiah, J. C.; Lynden-Bell, R. M.; Lee, S. H. *J. Phys. Chem*. **1998**, *102*, 4193.

(34) Parsegian, V. A.; Rand, R. P.; Rau, D. C. Proc. Natl. Acad. Sci. USA. **2000**, *97*, 3987.

(35) Washburn, E. W. *International Critical Tables of Numerical Data, Physics, Chemistry, and Technology*; McGraw-Hill: New York, 1928: Vol. 4.

(36) Grigera, J. R.; Kalko, S. G.; Fischbarg, J. *Langmuir.* **1996**, *12*, 154.

(37) CRC Handbook of Chemistry and Physics: 62nd edition, Boca Raton, **1993** Weast, R. C.

Chapter 4

Molecular dynamics simulation of water near nanostructured hydrophobic surfaces: Interfacial energies

ABSTRACT

We present results from molecular dynamics simulation of water near structured hydrophobic surfaces. The surface structures studied in this article are a planar alkane crystal as reference and crystals with a hole and a protrusion of approximately 2.5 nm diameter and 0.5 nm depth or height. All indicators show that surface structuring increases the hydrophobicity: The water density is reduced near the structure elements and the number of residual contacts between water and the surface decreases by about 40% with respect to the planar surface. Thermodynamic integration shows that the interfacial energy of the structured surfaces is about 7mJ/m^2 higher for structured surfaces than for the planar surface. The hydrophobicity increases by similar amount for the hole and the protrusion geometries compared to the planar surface.

4.1.INTRODUCTION

We investigate the effect of a hole and a protrusion indented/raised on a planar hydrophobic surface on the structural and thermodynamic properties of water at the interface with it. As a model of the surface, we use an alkane crystal. The properties of interest are the density distribution of water near the hydrophobic surface, the potential of mean force calculated from the density distribution and the contacts between water and the structured crystal. Finally, we compare the difference in hydration free energy between a structured crystal and a planar crystal.

In order to see how surface structuring can increase the hydrophobicity of a surface, a view to the so-called lotus effect is useful.[1-10] The water on the surface of the lotus leaves is very unstable and rolling off it takes off any dirt with it. Many plant leaves use this phenomenon. The surface of the lotus leaf is structured on a micrometer

Submitted to ChemPhysChem

length scale. The water drop rests only on the tips of the peaked microstructures, the contact area between leaf and droplet is minimized.

Recently some of the theoretical and experimental studies were done in detail about the lotus effect.[11-14] The problem of drop roll-off from the surface was dealt with a very simple theoretical model of the protrusions on a planar surface by Marmur.[11] In this article, the wetting on rough surfaces was studied in two regimes: homogeneous regime, where the liquid completely penetrates the rough grooves or heterogeneous wetting, where air is trapped underneath the liquid inside the rough grooves. The dynamic electrical control of the wetting behaviour of liquids on nanostructured surfaces has been dealt with by Krupenkin et al.[13] The method primarily relies on using the electrowetting to adjust the local contact angle that the liquid forms with the nanosized features of the surface.

Lee *et al*.[15] have compared the structure and dynamics of water near two different hydrophobic surface, one near a flat surface and the other near an atomic Lennard-Jones surface. The range of the surface induced perturbation in the static and dynamical properties of water is found within two layers of water molecules (~ 0.8 nm) from the surface. The density profiles of the water molecules near an atomic Lennard-Jones surface is slightly higher and is shifted more towards the hydrophobic surface than the perfectly planar surface. The water molecule near atomic Lennard-Jones surface manifest slowed translational dynamics compared to that of a flat surface.

While the recent theoretical and experimental articles on Lotus effect describe how the hydrophobicity changes due to microstructuring, in this article we consider comparing two different surface structures, a hole and protrusion, of nanometre dimensions. The motivation for performing the calculations are basically two. Firstly, we supplement our previous article[16,17] which found enhanced hydrophobicity for structured hydrophobic surfaces having different indentations (hexagonal, stripes, triangular) compared to flat surfaces. While indentations are easier to manufacture technically, it is not clear if they are as efficient as protrusions for increasing the hydrophobicity of the surface. We, therefore study here the most efficient hole geometry (diameter ≈ 2.5 nm) in comparison with a protrusion of the same size.

Secondly, this article goes beyond the analysis of water density and structure presented in reference 16. We study here also the differences in interfacial free energy

between a planar surface, a surface with a hole and a surface with a protrusion. There exist simulation approaches for finding the absolute hydration free energy of a hydrophobic interface.[18,19] They are, however, in the present form suitable only for interfaces between two isotropic phases (vacuum, fluid, structureless walls, crystal/melt interface). In this article we use thermodynamics integration to calculate the difference in the Helmholtz free energy of hydration between a structured (hole or protrusion) and a planar crystal. If the free energy change is positive then the structured surface is more hydrophobic than the planar surface and vice versa.

4.2 Computational details

4.2.1 Details of the surface structure

A crystal of n-eicosane molecules ($C_{20}H_{42}$) (one layer of 7×12 molecules) serves as the model of our hydrophobic surface. Crystallography of n-eicosane shows that it has a triclinic crystal structure.[18-20] The model of our n-eicosane crystal has been described in reference 17. The crystal structure is triclinic ($\alpha = 67.6^0, \beta = 83.9^0, \mathrm{c} = 2.544\ \mathrm{nm}$) and close to the experimental crystal ($\alpha = 68.2^0, \beta = 85.7^0, \mathrm{c} = 2.743\ \mathrm{nm}$).[19-22] The eicosane crystal (thickness 2.5 nm) was separated from its periodic image by a water layer (thickness 2.6 nm). Two different topographies were created on the surface (Figure. 4.1):

A hexagonal hole (19 alkane chains shortenened by four carbon atoms) and a hexagonal protrusion of the same size (65 alkane chains shortened by four carbon atoms resulting in the remaining 19 chains forming a protrusion on the surface of the planar crystal). Figure. 4.2 shows the schematics and defines the label of the different surface segments for the remainder of this article. Figure 2.4 shows the top view of a $C_{20}H_{42}$ crystal with a surface structure raised/indented on it. In all analyses, z = 0 refers to the surface of the planar crystal defined by the arithmetic mean of the z coordinates of all the unindented surface carbons, so the hole carries a negative z and the protrusion a positive z (Figure 4.2). The protrusion was created on only one side of the crystal to keep the water on both the sides of the surface well separated. However, holes were created on both the sides of the crystal and offset by 2 nm in the y direction and 1 nm in the x direction to have more statistics. Measuring between carbon chain positions flanking the holes/protrusions, the hole and protrusion have a

diameter of approximately 2.5 nm. To convert to the inner widths, the diameter of a CH_3 group should be subtracted from these values. The total surface areas of the hole and the protrusion is $\sim 2.5 \times \pi \times 0.5\,\mathrm{nm}^2 = 4\ \mathrm{nm}^2$. With the surface area of the crystal of $3.3 \times 5.3\,\mathrm{nm}$, we therefore have a percentage of indented/raised surface of 21.8%.

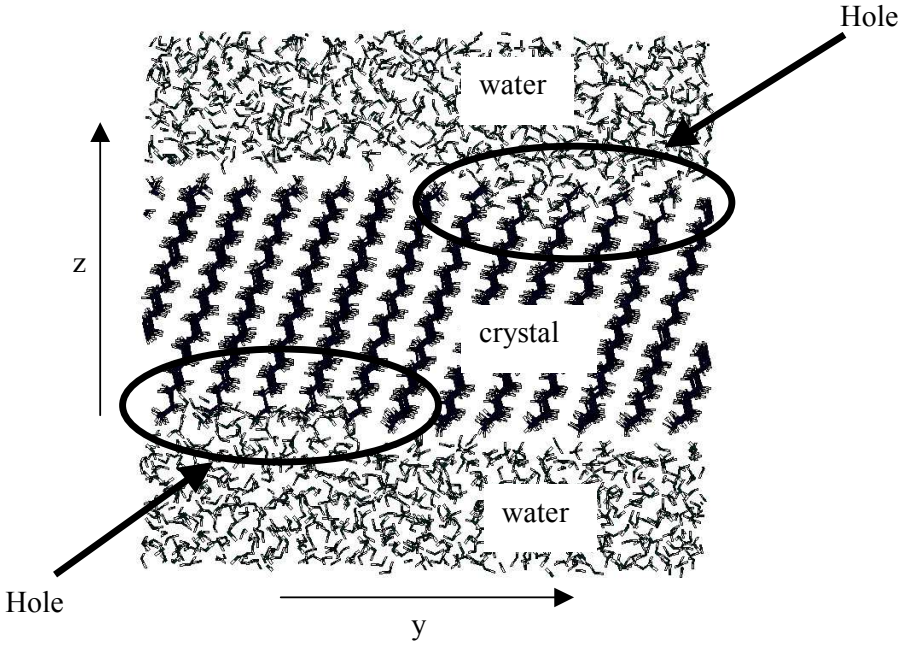

(a)

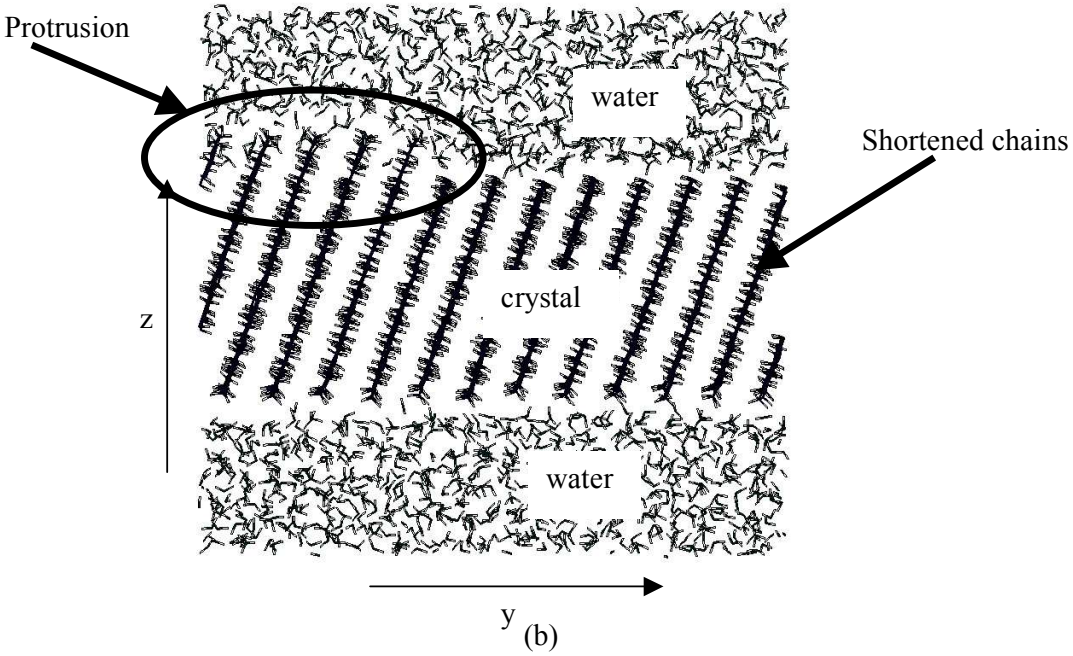

(b)

Figure: 4.1 The system chosen for our MD simulation. One corrugation/hole is indicated in the figure.

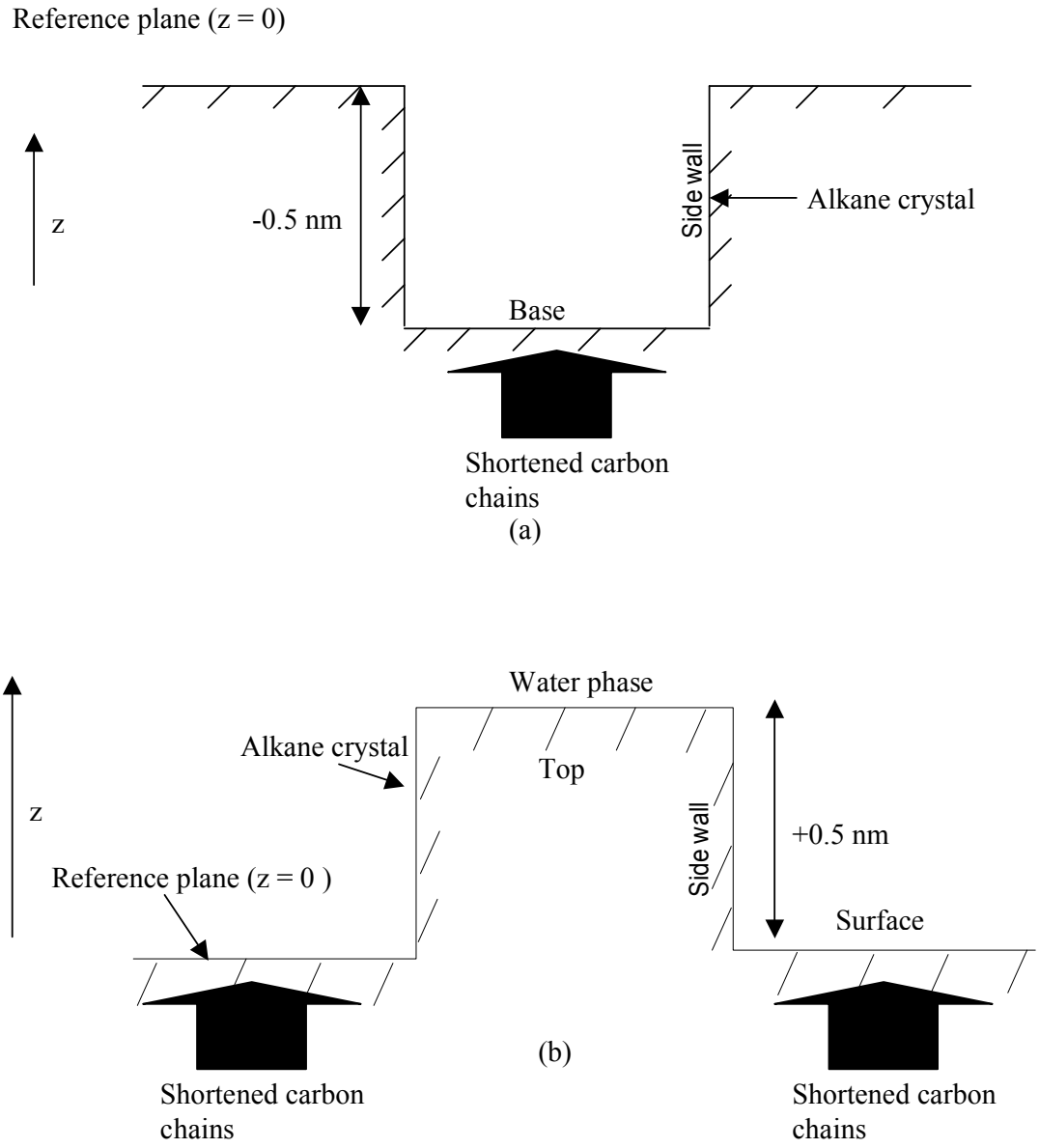

Figure 4.2 (a) The schematic of the hole. The reference height (z = 0) is the average of the terminal methyl carbons. The depth of the hole is ~ 0.5 nm. (b) The schematic of a protrusion. The reference height (z = 0) is the average of the terminal methyl carbons. The height of the protrusion is ~ 0.5 nm.

4.2.2 Simulation model

Our periodic simulation box ($3.3 \times 5.3 \times 5.1\,nm^3$) contained 1500 molecules of water and 84 n-eicosane molecules. The details of the simulation setup are discussed in reference 17. We have used the YASP simulation package[23] for the molecular dynamics simulations. The system was weakly coupled to the desired temperature (298 K) with a relaxation time of 0.2 ps.[24-25] The Cartesian diagonal components of the pressure tensor were coupled separately to an external pressure of 0.1013 MPa with a relaxation time of 5 ps.[24-27] Bond lengths were constrained using the SHAKE algorithm.[28] The time step for the leapfrog integration scheme[24-25] was set to 0.002 ps and the trajectory frames were saved every 1 ps. The total simulation run was 2 ns with 1 ns for the equilibration and the production run respectively. Non-bonded interactions were evaluated at every time step with a cutoff radius of 0.9 nm and using a neighbour list (update every 20 steps, neighbour list cutoff 1.0 nm). The n-eicosane was described by the all-atom OPLS model.[29-30] Water was treated with the SPC/E model.[31] Lennard-Jones parameters for interactions between unlike atoms were evaluated using the Lorentz-Berthelot mixing rules,[24] electrostatic interactions were treated with the reaction field approximation,[24] using an effective dielectric constant of 72. The intra/inter molecular interactions (Lennard Jones + Coulombic interaction) between the chains were switched off in the calculations of non-bonded interactions between alkane molecules, springs were used between adjacent carbons of any chain and carbons of its six nearest neighbours taking into account periodic boundary conditions. The springs were used between carbons of the same index (i.e. C_i - $C_i^{/}$, length: 0.497 nm) and carbon one index apart (C_i - $C_{i+1}^{/}$, length: 0.89 nm). The spring constants were chosen as 2000 kJ mol^{-1} $Å^{-2}$. These lengths were chosen to maintain crystal structure of n-eicosane[15-17] in constant pressure simulations. This rigidification was necessary not so much for the native planar alkane slab, but to prevent surface reconstruction of structured alkane surfaces, which contained also shorter alkane chains.

The thermodynamic integration calculations[32,33] were carried out with the GROMACS molecular dynamics simulation package.[32-36] The details of the procedure are discussed in section 3.3. The potential parameters except the alkane-alkane interactions are the same as described above for the simulations using YASP.

GROMACS uses the softcore non-bonded potentials for the thermodynamic integration procedure. In order to avoid singularities the soft-core potential *Vsc* is:

$$V_{SC}(r) = (1-\lambda)\, V^A(r_A) + \lambda\, V^B(r_B) \quad (4.1)$$

$$r_A = (\alpha\sigma_A^6 \lambda^2 + r^6)^{1/6} \quad (4.2)$$

$$r_B = (\alpha\sigma_B^6 (1-\lambda)^2 + r^6)^{1/6} \quad (4.3)$$

where λ is the coupling parameter which varies from 0 to 1. V^A and V^B are the normal "hard core" van der Waals or electrostatic potentials in states A (λ = 0) and B (λ = 1), respectively, α = 1.51 is the soft-core parameter, which mainly controls the height of the potential around $r = 0$,[36] σ is the radius of the interaction defined as $\sigma = \left(\frac{C_{12}}{C_6}\right)^{1/6}$, or $\sigma = 0.3$ nm when C_{12} or C_6 (Lennard Jones 12 and 6 terms) is zero.

The simulations were established at constant pressure (NPT ensemble) using a anisotropic coupling during the equilibration run of 1 ns for each value of the coupling parameter λ: The compressibility in the xy directions was chosen at a very small value (10^9 times less than the compressibility of water) to keep the crystal geometry rigid in the xy direction, whereas in the z direction the value was equal to the compressibility of water. The box geometry was then fixed and a production run of 4 ns was performed at every λ at a constant volume (NVT). The bond lengths were constrained using the SHAKE algorithm and a leapfrog algorithm was used for integrating the equations of motion. The cutoff for the different nonbonded interactions was 0.9 nm. The Coulombic interactions were treated with a reaction field technique (ε = 72). As in the MD simulation using YASP [no thermodynamic integration], the only interaction potential present inside the crystal is the spring potential and the bonded interactions between atoms within a molecule, which did not change with the coupling parameter λ. The masses of the atoms being switched on/off were not changed.

4.2.3 Analysis

The simulations were analysed in terms of the density of water at and near the interface. We have analysed the local densities by dividing the simulation box into cells ($0.4 \times 0.4 \times 0.2\,\text{nm}^3$) and finding the density in each cell. Since the crystal is not space fixed and has the freedom to diffuse in x and y direction, the grid geometry was

attached to it in order to get consistent density distributions in the course of the MD simulations. Fixing grid points to the surface carbon atoms of the crystal does this. The density distribution (g/cm^3) was evaluated using

$$\rho(\vec{r}) = \frac{< N[\vec{r}, (x - \frac{\Delta x}{2}, x + \frac{\Delta x}{2}), (y - \frac{\Delta y}{2}, y + \frac{\Delta y}{2}), (z - \frac{\Delta z}{2}, z + \frac{\Delta z}{2})] > \mathrm{M_W}}{\Delta x \Delta y \Delta z}. \qquad (4.4)$$

where $\vec{r} = (x, y, z)$ is the centre of the cell, Δx, Δy, Δz are the lengths of the sides of the cell, M_w is the molecular weight of water and $< N[\vec{r}] >$, is the number of water oxygens inside the cell at $\vec{r}$ averaged over the 10^3 trajectory frames. The density distributions were converted to local chemical potentials using Boltzmann inversion[32]

$$\Delta\mu(\vec{\mathrm{r}}) = \text{-RT ln}\left(\frac{\rho(\vec{\mathrm{r}})}{\rho_{Bulk}}\right). \qquad (4.5)$$

ρ_{Bulk} is the bulk density of water away from the surface calculated at the centre of the water layer, $\Delta\mu(\vec{\mathrm{r}})$ is the difference of the chemical potential between position $\vec{r}$ and the bulk water chemical potential. For $\Delta\mu(\vec{\mathrm{r}}) < 0$, position $\vec{\mathrm{r}}$ is hydrophilic and if $\Delta\mu(\vec{\mathrm{r}}) > 0$ it is hydrophobic.

For the thermodynamic integration calculations, the hole/protrusion was created by reversibly switching on/off the interaction between four carbon atoms and associated hydrogens of 19 chains, from the 84 chains, and water, Fig. 4.[24-25] Care has been taken to turn the fourth carbon atom from the surface to a hydrogen atom and the bond length of the of the resulting carbon hydrogen bond value was equal to 0.109 nm. The torsional and the angle potentials were not altered during this change. The difference in the free energy between two states A and B of a molecular system, with Hamiltonians denoted by $H_A(\vec{r})$ and $H_B(\vec{r})$, is expressed as

$$\Delta A_{BA} = A_B - A_A = \int_0^1 \left\langle \frac{\partial H(\vec{r};\lambda)}{\partial \lambda} \right\rangle_\lambda d\lambda, \qquad (4.6)$$

where $\vec{r}$ is the (3N-dimensional) position vector of the N atoms of the system, and $H(\vec{r};\lambda)$ is the Hamiltonian parameterized by the coupling variable λ, and satisfying

$$H(\vec{r};0) = H_A(\vec{r}) \qquad \text{and} \qquad H(\vec{r};1) = H_B(\vec{r}). \qquad (4.7)$$

The angle brackets in (4.6) denote averaging over an equilibrium ensemble generated with the Hamiltonian function $H(\vec{r};\lambda)$. We have employed the multiconfiguration

thermodynamic-integration method[32] to evaluate the integral in eq.(4.6). This method performs a separate simulation at a number of discrete λ. At each λ point the value of $\left\langle \partial H(\vec{r};\lambda) / \partial\lambda \right\rangle$ is calculated. The integral in equation (4.6) is then determined numerically using the trapezoidal rule. The error bars at each λ point were found by block averaging[25] (150 blocks used in our simulations) of $\left\langle \partial H(\vec{r};\lambda) / \partial\lambda \right\rangle$ points. The error in the thermodynamic integration was determined using the following expression.[33]

$$\delta(\Delta A) = \left[\sum_{n=1}^{N_\lambda} w(\lambda_n) \delta^2 \left(\langle \partial H / \partial \lambda \rangle_{\lambda_n} \right) \right]^{1/2} \tag{4.8}$$

where $w(\lambda_n)$ is the weight

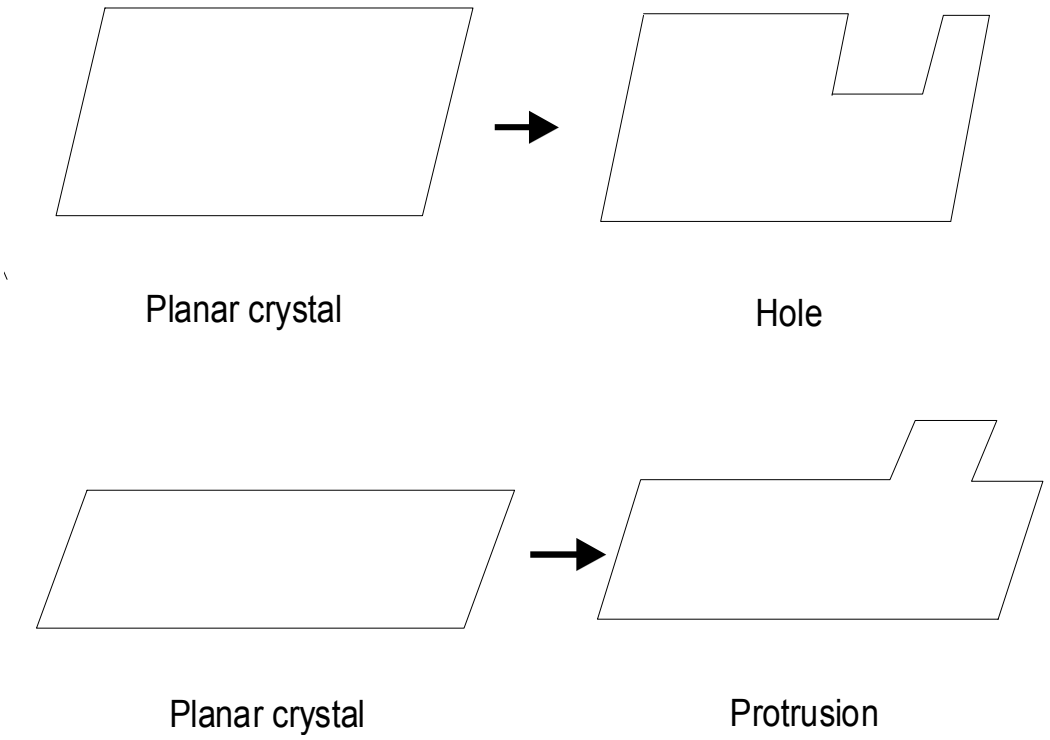

Figure 4.4. Schematic of the change in the free energy of hydration from a planar crystal to a structured crystal.

4.3 RESULTS AND DISCUSSION

4.3.1 Density distribution of water near the two surface structures

The grid geometry as described by equation (4.4) is used to describe the various density distributions discussed below. Figure. 4.5 shows the density profile in a yz slab of thickness $\Delta x = 0.5$ nm positioned between $x_1 = -0.25$ nm and $x_2 = 0.25$ nm relative to the central reference carbon atom. This slab vertically cuts through the surface and the protrusion/hole. For comparison, the water density near a planar crystal is also plotted.

From the Fig 4.5(a) and 4.5(b) following observations are evident. (a) The water density is less at the edge walls of the holes and the protrusion, it avoids contacts with the edges of the surface structures. (b) The density of water at the surface of the crystal in all cases is higher than in the bulk water region. This is due to the structuring of water at the interfacial region of water and the crystal surface. (c) The density of water at the "base carbons" (cf. Fig.4.2) of the holes is ~ 0.5 g/cm^3 Fig. 4.4(a) , at the "top carbons" (cf. Fig.4.2) of the protrusions is ~ 1.4 g/cm^3, Fig. 4.4(b). holes are –0.4 to –0.2 nm, -0.2 to 0 nm, 0 to 0.2 nm, 0.2 to 0.4 nm, 0.4 to 0.6 nm and 0.6 to 0.8 nm, respectively, Fig 4.5(a) to (f). In case of the protrusions the following slabs of thickness 0.2 nm, from Fig. 4.6 (a) to (f) were chosen, 0 to 0.2 nm, 0.2 to 0.4 nm, 0.4 to 0.6 nm, 0.6 to 0.8 nm, 0.8 to 1.0 nm and 1.0 to 1.2 nm, respectively. Similar analysis has been used in the past to investigate the hydrophobicity of cellulose surfaces.[32]

At –0.4 to –0.2 nm region, Fig 4.5(a), inside the hole the water density around the 19 head groups of the base carbons are evident showing the underlying crystal arrangement of the base carbons. Fig 4.5(b), -0.2 to 0 nm, also shows the water density inside the hole however the underlying crystal geometry is less evident in this region, since at this level a closed water layer inside the hole in possible. The water density is lower at the side walls than the centre of the hole. At 0-0.2 nm from the surface Fig. 4.5(c), there are only few water density spots on the surface of the crystals as the slab thickness is too small to include the first layer of water molecules. Again the underlying crystal structure is visible in the water density: Water molecules can approach the surface away from the hole more closely at the small depressions between adjacent CH_3 groups. Above the hole the water density is larger, rising to

0.7-0.8 g/cm^3 above the centre of the hole. At this level, the hole geometry is visible in the water density.

In order to understand the effect of the two surface topographies on the interfacial water in a systematic way, horizontal slabs (layers) of 0.2 nm thicknesses were placed at different heights (z) above the surface, Fig. 4.5 and 4.6. The heights considered for the

In the layer between 0.2 and 0.4 nm, Fig. 4.5(d), the influence of the hole geometry is not clear. The underlying crystal geometry is not visible as a layer of water molecules at this altitude. At the level between 0.4 and 0.6 nm distance, the density above the hexagonal hole is around 0.7 g/cm^3, whereas it is just below the bulk value elsewhere Fig. 4.5(e). Fig. 4.5(f) shows that the water density has reached its bulk value and there is no influence of hole in this region. In Fig.4.6 we compare the water density around and above the protrusion. Fig. 4.6(a) (0-0.2 nm) clearly depicts the excluded volume. Fig 4.6(b), 0.2 - 0.4nm, shows a not so sharp interface between water and the side walls of the protrusion. Interestingly, the density is lower on the surface west and east (x) of the protrusion than north and south (y). This is owed to the fact that the periodic images of the protrusions stand much closer in x than in y. Similar observations of density reduction were made for holes of different sizes and shapes[17]. Fig. 4.6(c) shows the density distribution of water in the region between 0.4 and 0.6 nm slab in case of the protrusion. At this altitude the nineteen "top" CH_3 groups surrounded by water molecules predominantly from the sides of the protrusion and to a lesser extent from the top of the protrusion are visible. The water molecules have a higher density at the edges of the protrusion than the centre of the protrusion. Fig. 4.6(d), layer between 0.6-0.8 nm, shows the water density is slightly greater above the protrusion than the surrounding region. In the Fig 4.6(e) and (f), the water density is similar to the bulk water and the influence of the surface structures on the water density is barely evident.

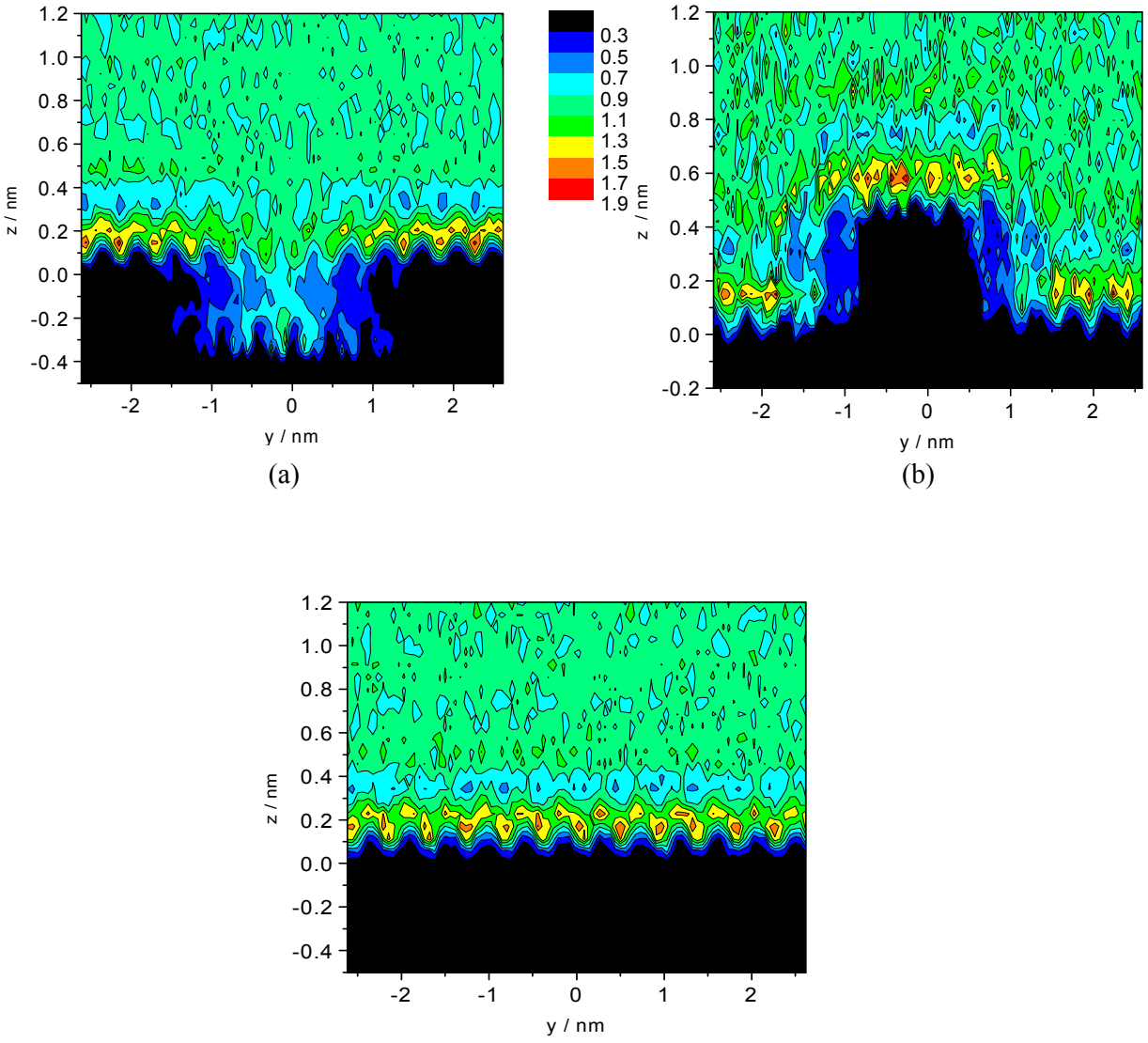

(a) (b)

(c)

Figure 4.5. Water density (g/cm^3) in a vertical (yz) slab of thickness $\Delta x = 0.5$ nm cutting through the centre of the hole/protrusion (a) Hole (b) Protrusion (c) Planar crystal.

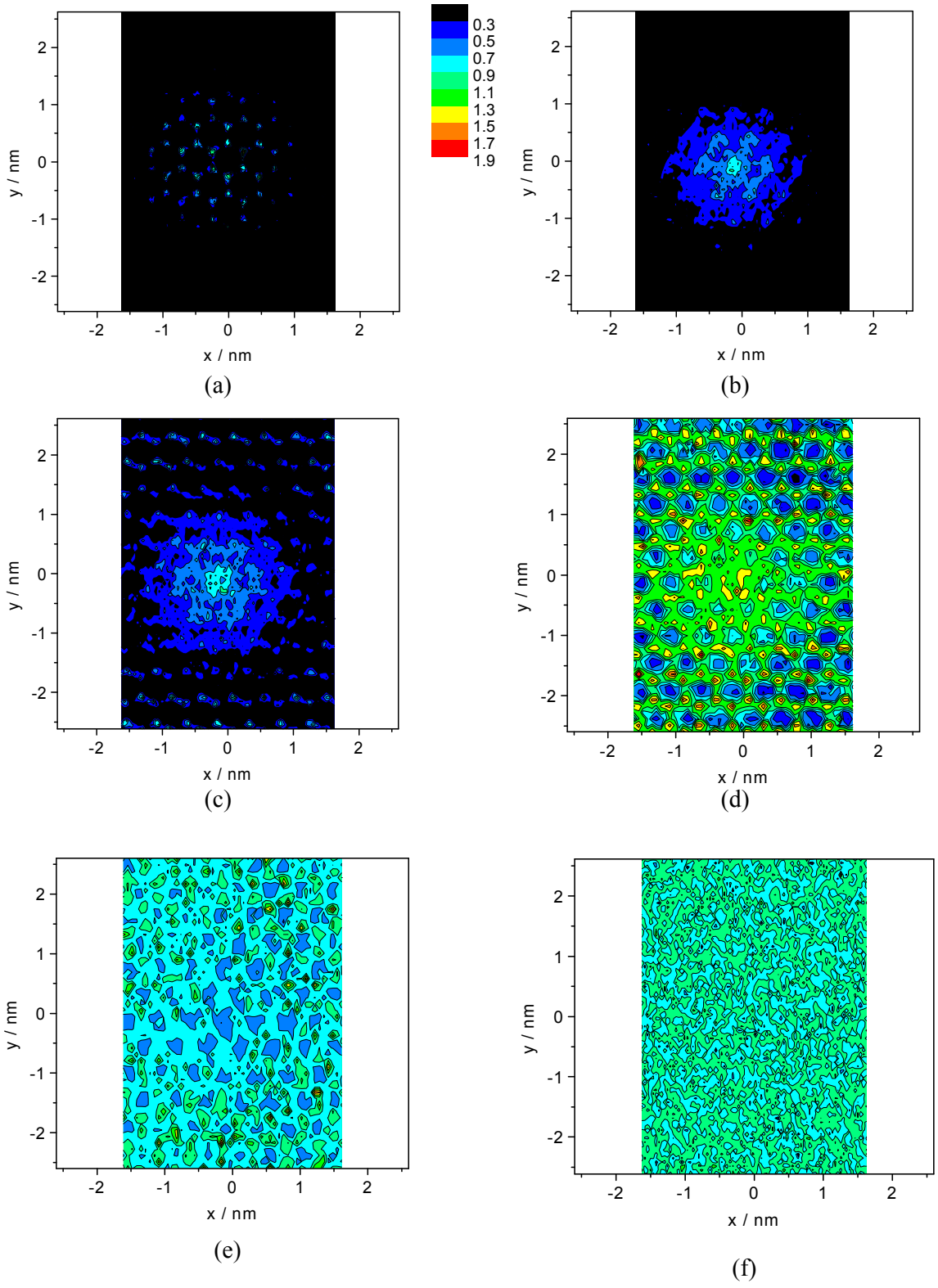

Figure 4.6. Water density (g/cm^3) in the vicinity of the hole for slabs placed in the xy direction at the following range of heights (a) z = -0.4 to -0.2 nm (b) z = -0.2 to 0 nm and (c) z = 0 to 0.2 nm (d) z = 0.2 to 0.4 nm (e) z = 0.4 to 0.6 nm (f) z = 0.6 to 0.8 nm.

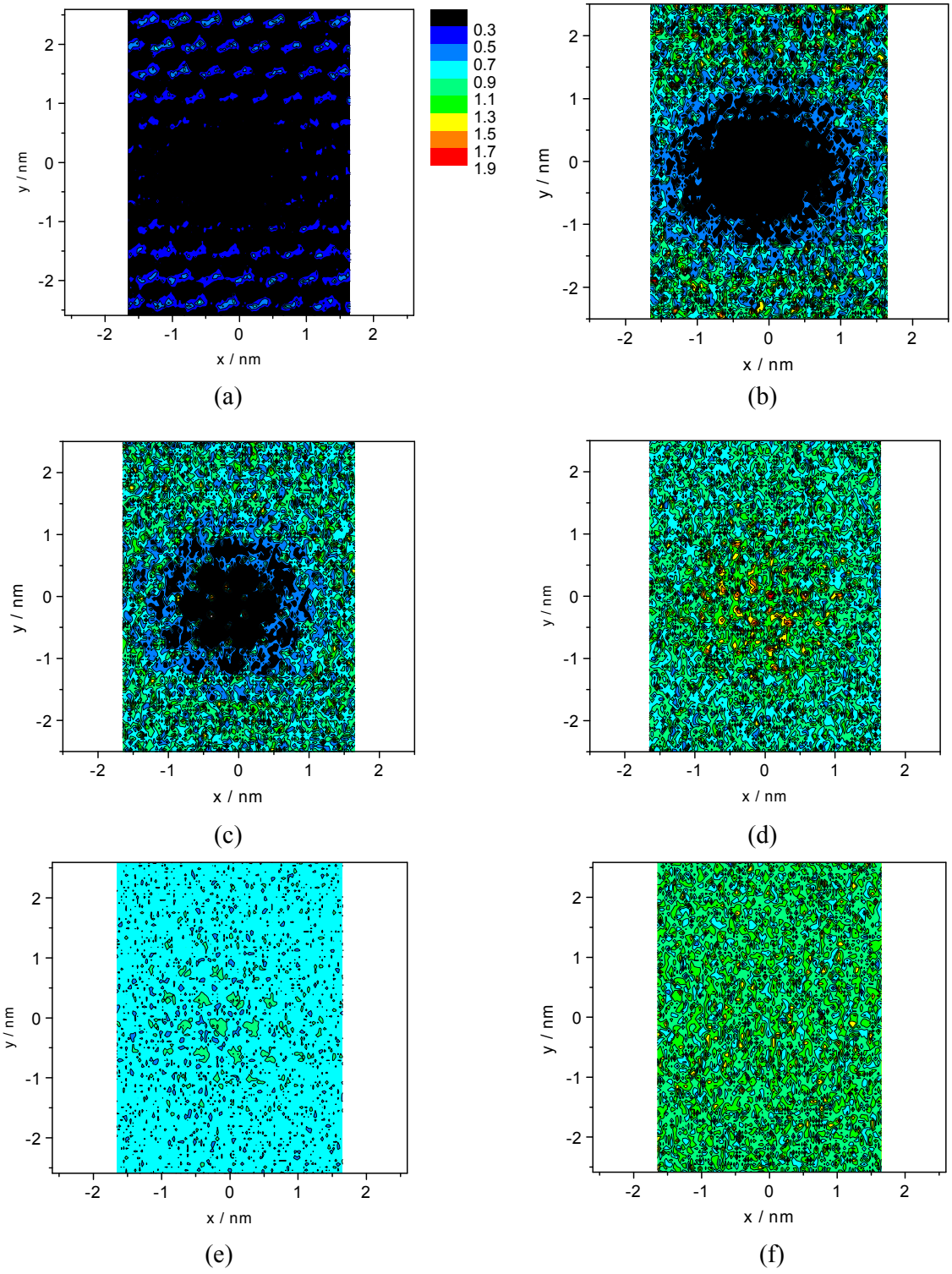

Figure 4.7. Water density (g/cm^3) in the vicinity of the protrusions for slabs placed in the xy direction at the following range of heights (a) z = 0 to 0.2 nm (b) z = 0.2 to 0.4 nm and (c) z = 0.4 to 0.6 nm (d) z = 0.6 to 0.8 nm (e) z = 0.8 to 1.0 nm (f) z = 1.0 to 1.2 nm.

4.3.2 Water density normal to the surface

Figure. 4.7(a) shows the density averaged in the x and y direction as a function of z. The same grid as before is used for the analysis. Recall that z = 0 corresponds to the height of the surface carbons. Thus, cells inside the alkane crystal are excluded. In all cases, the water density approaches the same bulk density of water ~ 0.98 g /cm^3 away from the crystal surface. The water density in case of a hole and a planar crystal shows the same height of the first peak 1.38 g/cm^3 at 0.25 nm from the surface. The density of water inside the hole is ~ 0.2 g/cm^3. For the protrusion, the water density has a shoulder at 0.18 nm and peaks at 0.28 nm and 0.6 nm. Their height is 1.0 g/ cm^3 whereas the density in case of the hole and the planar surface are similar and is significantly different in case of the protrusion.

The density distributions were converted to chemical potential differences by Boltzmann inversion, (Fig. 4.7(b)) using equation (4.5). The figure shows that at z ≈ 0.25 nm the value of Δμ is –0.25RT, in case of the hole and the planar slab, implying a small free energetic benefit for water to be at the interface than in the bulk. However the value Δμ/RT rises sharply inside the hole. In case of the protrusion, there is no region of Δμ/RT < 0 which means that water is not attracted to the surface preferentially.

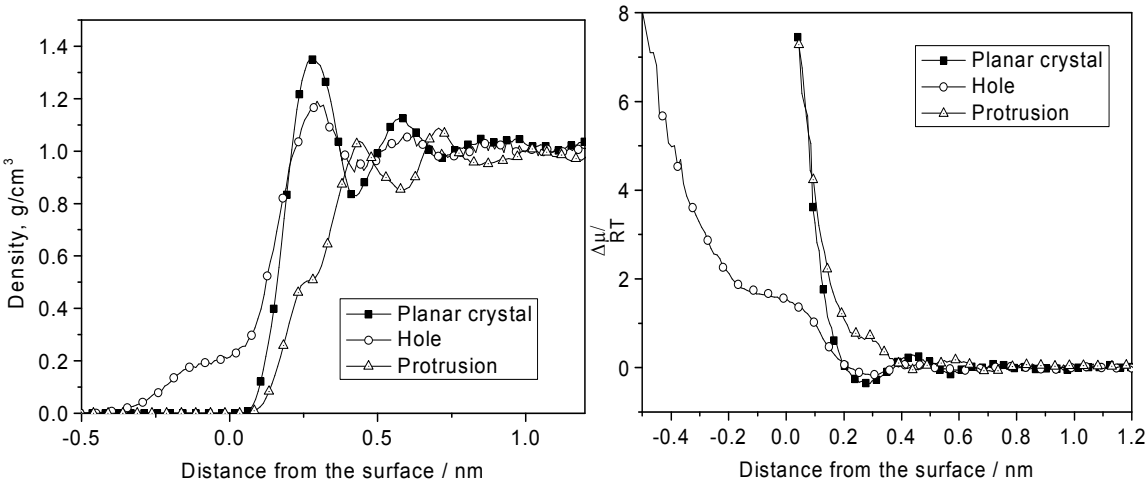

(a) (b)

Figure 4.8. (a) Density of water as a function of z, the distance from the surface. (b) Difference of the water chemical potential as a function of z from the surface.

4.3.3 Contacts of water with the surface carbon atoms

The number of contacts, the water makes with the surface atoms, can also be used to judge the hydrophobicity of an interface. The more contacts there are, the larger is the residual dispersive attraction between water and surface, and the lower is the hydrophobicity. As surface carbons we count all methyl carbons at chain ends, as well as the three following methylene carbons of the chains forming the sides of the hole/protrusion. The contacts are calculated from the corresponding radial distribution function, g(r). Figure. 4.8(a) shows the radial distribution functions between oxygen atoms of the water molecules and all surface carbons. For comparison, the corresponding g(r) for a completely planar surface is also included. Fig. 4.8(b) and (c) shows the different contributions to the radial distribution function between water and surface carbons.

The number of contacts is obtained by integrating the first peak of the radial distribution function (0 to 0.5 nm) (Table 4.1). The number of contacts are analysed in the two following ways, per water oxygen atom (water side) and per surface carbon atom (surface carbon side). The total number of contacts from the water side is the sum of all the three contributions. The contributions to surface carbons, in case of protrusion (on one side), are 65 reference plane carbons, 36 side wall carbons and 19 top surface carbons. In case of hole the contributions are 130 reference plane carbons, 108 side wall carbons and 38 top surface carbons, considering the contributions from both the sides of the slab. A water molecule has considerably fewer contacts with either of the structured surfaces than with the planar surface. The number of contacts is similar for the hole and the protrusion geometry, with the later being slightly lower. The contacts are, however, being made with different atoms. The reference plane has 1.5 times more contacts in case of hole than the protrusion. The protruded carbons however have 3 times more contact than the hole base carbons. The number of contacts from of the side walls is approximately the same for both the protrusion and the hole.

Comparing the number of contacts from the carbon side, the number of contacts of the reference plane is 1.5 times higher for the hole than for the protrusion. The protruded carbons have 3 times more contacts than the base carbons. The side wall

carbons shows 1.2 times more number of contacts in case of protrusion than the hole. The total number of contacts between all the surface carbons and water is the same in case of hole/protrusion however it is 40% less than for the planar crystal. From this we conclude that the surface structuring does impart higher hydrophobicity to the crystal. However the analysis shows difference between protrusion and hole geometry in terms of number of contacts.

4.3.4 Free energy calculations

The Gibbs free energy difference between a crystal with surface structuring and a planar crystal is calculated in this section. The coupling variable λ, is used to scale the potential parameters of atoms, which participate in reversibly changing the crystal from planar ($\lambda = 0$) to a structured ($\lambda = 1$). The transformation during the free energy calculations from an interacting to a non-interacting ghost or dummy atoms in the slab were performed using at least 23 λ points, which was sufficient to ensure a smooth integrand.

We have the following expression for the Hamiltonian of a planar crystal with water H_i.

$$H_i = [H_{ww} + H_{wc}]_i \tag{4.9}$$

where H_{ww} and H_{wc} are the Hamiltonian for water-water and water-crystal interacitons. (The subscript i indicates initial). Similarly, we can write the Hamiltonian of the final system i.e. water + structured crystal.

$$H_f = [H_{ww} + H_{wc} + H_{sw}]_f \tag{4.10}$$

where H_{sw} is the Hamiltonian due to the surface structure (hole/protrusion) on the surface of the crystal. It consists of additional interactions with the added carbon units in the case of the protrusion. For the hole case, however, H_{sw} corresponds to removing the appropriate water-carbon and water-hydrogen interactions. The water–water Hamiltonian does not change with the coupling parameter λ. With the change in coupling variable λ, H_{wc} and H_{sw} change. The results of the integration are shown in Table 4.2 with the associated error bars calculated from eq. 4.8 after 4 ns of production run. As the volume is allowed to equilibrate at each λ point, the free energy allows for a $p\Delta V$ term and is the Gibbs free energy for the process of creating a hole or protrusion. From the volume change (~ 2 %) the $p\Delta V$ contribution can be

estimated. It amounts to ≈ 10^{-2} mJ/m^2, which is small compared to the free energy changes and their error bars. The Gibbs and Helmholtz energies for the surface structuring can, therefore be considered numerically equal.

The change in the surface free energy is positive in both cases. This implies that both the hole geometry and the protrusion geometry impart higher hydrophobicity to the crystal. For both, the gain of free energy is of similar order.

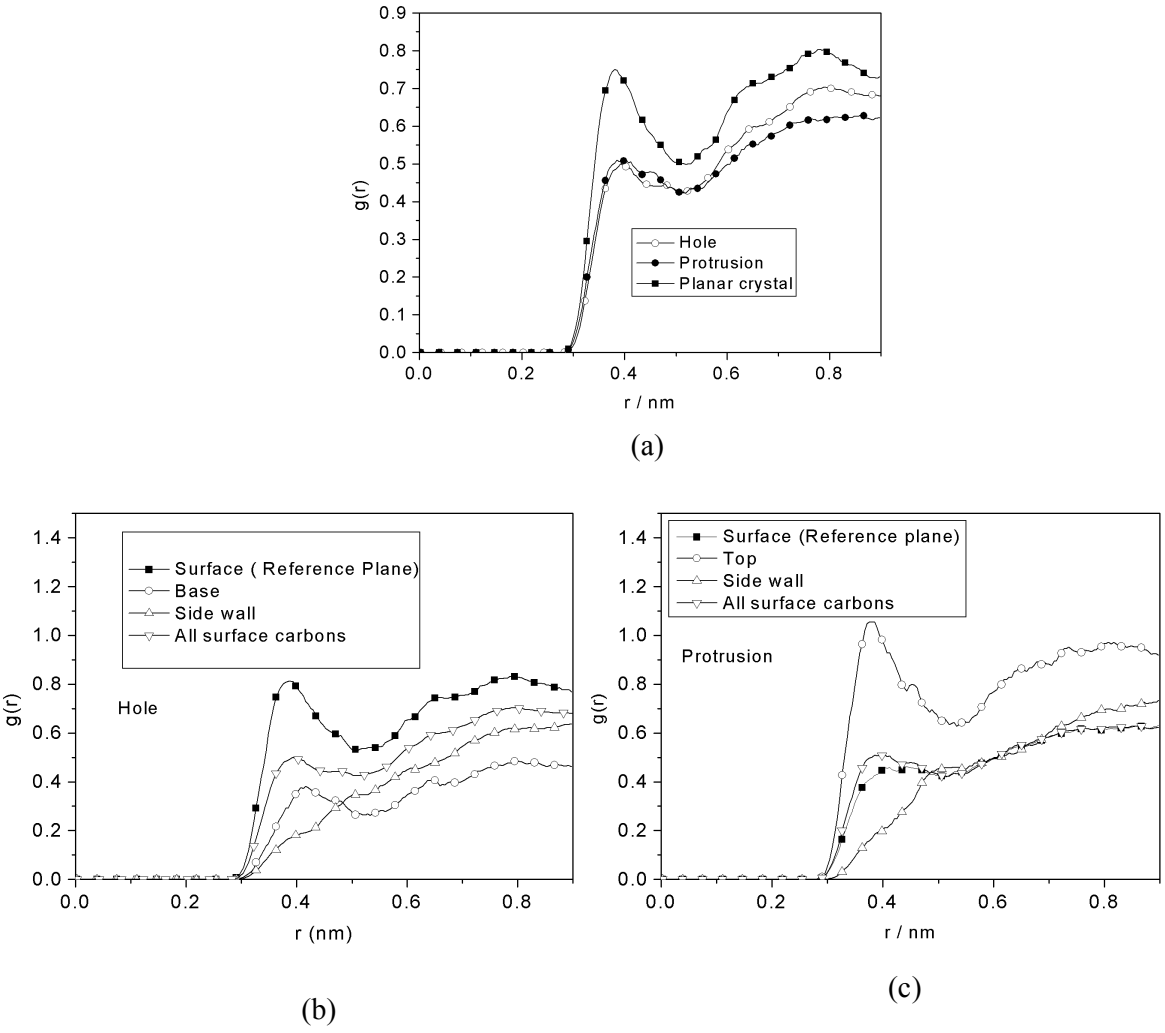

Figure 4.9. (a) Radial distribution function between all surface carbons and water. Radial distribution function between different components of surface carbons as mentioned in Fig. 4.4 and water (a) Hole (b) Protrusion.

Table.4.1 Number of contacts between water and the surface carbon atoms from the water side. Inside the parentheses the number of contacts from the surface carbon side is reported.

Surface structuring	Reference plane	Base/Protrusion	Side walls	All surface
Hole	0.19 (4.4)	0.03 (2.0) (Base carbons)	0.05 (1.5)	0.27 (3.0)
Protrusion	0.13 (2.9)	0.07 (5.7) (Top carbons)	0.05 (1.9)	0.25 (3.1)
Planar crystal	0.45 (4.0)	-	-	0.45 (4.0)

Table.4.2 Difference in the free energy of hydration between a structured crystal (Hole/protrusion) and a planar crystal

Free energy process	ΔA (kJ / mol)	ΔA / Area (mJ/m^2)
Planar crystal → Hole geometry	75 ± 13	7.1 ± 1.0
Planar crystal → Protrusion geometry	66 ± 13	6.3± 1.0

4.4 CONCLUSIONS

Nanostructuring enhances the hydrophobicity of a surface, which is per se already hydrophobic. The density profile of water near our hydrophobic planar crystal is similar to the density profile of water near an atomic Lennard-Jones surface studied by Lee *et al.*[15]. The location of the first peak of the water density profile is at the same distance with respect to the hydrophobic surface (~0.25 nm) (comparing our simulation and the simulation of Lee *et al.*[15]), however the first peak of the water density profile has an amplitude of 1.38 g/cm^3 (in our simulations) compared to the amplitude of 1.25 g/cm^3 observed by Lee *et al.*[15] for atomic Lennard-Jones surface.

We have created structures ~ 2.5 nm in diameter and ~ 0.5 nm in depth or height on alkane crystals serving as models for a hydrophobic material. Both indentations and protrusions increase the hydrophobicity by approximately the same amount. The increased hydrophobicity is evident in the average number of contacts experienced by a water molecule. It drops from 0.45 for a planar surface to 0.27 and 0.25 for the surface with a hole and a protrusion, respectively. The effect can be quantified by thermodynamic integration calculations, which show that the free energy per unit area increases by 7.1 mJ/m^2 and 6.3 mJ/m^2 for the hole and the protrusion topographies, respectively, compared to the planar surface. While the precise values of these increments depend on details of the simulation such as force field parameters, the qualitative result is clear: Both ways of surface structuring increase the interfacial tension and hence the hydrophobicity. A methodological side result is that the simple reasoning based on water-surface contacts (fewer contacts → less interactions → higher hydrophobicity) is borne out by thermodynamic integration calculation of the surface free energy increments. As counting the number of contacts is much simpler and computationally cheaper than thermodynamic integration, it might be a quick qualitative estimator for comparing the hydrophobicities of different surfaces. More work is, however, needed to determine how universal this relation between contacts and surface tension is.

References

(1) Adam, N. K. *The Physics and Chemistry of Surfaces*; Oxford University Press: London, **1941**.

(2) Israelachvili, J. N. Intermolecular and surface forces; Academic Press, San Diego, 1991.

(3) Neinhuis, C.; Barthlott, W. *Annals of Botany.* **1997**, *79*, 667-677.

(4) Baker, E. A.; Parsons, E. *Journal of Microscopy.* **1971,** *9*4, 39-49.

(5) Barthlott, W. In: Claughter D, ed. *Scanning electron microscopy in taxonomy and functional morphology*; Oxford: Clarendron Press, **1990**, 69-94.

(6) Baker, E. A.; Hunt, G.M. **1986**, *102*, 161-173.

(7) Cassie, A. B. D.; Baxter, S. *Trans of Faraday Society.* **1944**, 40, 546-551.

(8) Adam, N. K.; In: Moilliet JL, ed. *Waterproofing and water-repellency*; **1963**, Elsevier, Amsterdam, 1-23.

(9) Linsken, H. F. *Planta.* **1950,** 38 , 591-600.

(10) Rentshler, I. *Planta.* **1971,** *96*, 119-135.

(11) Marmur, A. *Langmuir* **(Communication)**. **2004**, *20(9)*, 3517-3519.

(12) Wenzel, R.N. *Ind. Eng. Chem*. **1936**, 28, 988-993.

(13) Krupenkin, T. N.; Taylor, J. A.; Schneider, T. M.; Yang, S. *Langmuir* **(Communication). 2004,** *20(10),* 3824-3827.

(14) Otten, A.; Herminghaus, S; *Langmuir* **(Communication). 2004**, *20(6)*, 2405-2408.

(15) Lee, S. H.; Rossky, P. J. *Proceedings of the 10th Korean Scientists and Engineers Conference* (Inchen, Korea, 1987), 150-155.

(16) Pal, S.; Weiss, H.; Keller, H.; Müller-Plathe. F. *Langmuir.* **2005**; *21*(8); 3699-3709.

(17) Pal, S.; Muller-Plathe, F.; *J. Phys. Chem. B*. **2005**; *109*(13); 6405-6415

(18) Huang, D. M.; Chandler, D. *J. Phys. Chem*. B **2002**, *106*, 2047-2053.

(19) Davidchack, R. L.; Laird, B. B. *J. Chem. Phys*. **2003**, *118*(*16*), 7651-7657.

(20) Kirkwood, J. G.; Buff, F. P. *J. Chem. Phys.* **1949**, *17*, 3-9.

(21) Blokhuis, E. M.; Bedaux, D.; Holcomb, C. D.; Zollweg, J. A. *Mol Phys.* **1995**. *85*, 665-669.

(22) Nyburg, S. C.; Potworowski, J. K.; *Acta Cryst*. **1973**, *B29*, 347-352.

(23) Waheed, N.; Lavine, M. S.; Rutledge, G. C.; *J. Chem. Phys*. **2001**, *116*, 2301-2309.

(24) Small, D. M.; *The Physical Chemistry of Lipids: From Alkanes to*

Phospholipids; Plenum, New York, **1986**, 183-190.

(25) Müller-Plathe. F. *Comput. Phys. Commun*. **1993,** *78*, 77-94.

(26) Allen, M. P.; Tildesly, D. J. *Computer simulation of liquids*; Clarendon Press: Oxford, **1987**.

(27) Frenkel, D.; Smit, B. *Understanding Molecular Simulation*; Academic Press, San Diego, **2002**.

(28) Jensen, F.; *Introduction to Computational Chemistry*; Wiley VCH, Chichester, **1998**.

(29) Berendsen, H. J. C.; Postma, J. P. M.; van Gunsteren, W. F.; DiNola, A.; Haak, J. R. *J. Chem. Phys*. **1984**, *81*, 3684-3690.

(30) Ryckaert, J. P.; Ciccotti, G.; Berendsen, H. J. C. *J. Comp. Phys*. **1977**, *23*, 327-341.

(31) Duffy, E. M.; Jorgensen; W. L. *J. Am. Chem. Soc*. **2000**, *122*, 2878-2888.

(32) Kaminski, G.; Duffy, E. M.; Matsui, T.; Jorgensen, W. L. *J. Phys. Chem*. **1994**, *98*, 13077-13082.

(33) Berendsen, H. J. C.; Grigera, J. R.; Straatsma, T. P. *J. Phys.Chem*. **1987**, *91*, 6269-6271.

(34) Biermann, O.; Hädicke, E.; Koltzenburg, S.; Müller-Plathe. F. *Angew. Chem. Int. Ed.* **2001**, *113* , 3938-3942.

(35) Daura, X.; Mark, A. E.; van Gunsteren, W. F. *J. Comp. Chem*. **1998**, 19, 535-547.

(36) Berendsen, H. J. C.; van, der Spoel, D.; van Drunen, R. *Comp. Phys. Commun.* **1995**, 91, 43-56.

(37) Lindahl, E.; Hess, B.; van der Spoel, D. *J. Mol. Model.* **2001**, 7, 306-317.

Chapter 5

The hydrophobicity of nanostructured alkane and perfluoro alkane surfaces: A comparison by molecular dynamics simulation.

ABSTRACT

In this contribution we investigate the differences in the hydrophobicity of a perfluoro-n-eicosane crystal and the n-eicosane crystal by molecular dynamics simulation. The results were analysed in terms of density of water at the interface, the chemical potential of water at the interface and the orientational ordering of water at the interface. The perfluoro-n-eicosane crystal – water interface is found to have a less density, higher chemical potential and a weaker orientational ordering at the interface than the corresponding n-eicosane crystal.

5.1.INTRODUCTION

Perfluoroalkanes are known to be highly hydrophobic.[1-5] They are therefore candidates for manufacturing extremely hydrophobic surfaces. We investigate the hydrophobicity of an alkane crystal and a perfluoro alkane crystal, the two crystal chemistries, by molecular dynamics simulation. The comparison was made on two crystal geometries, a planar crystal surface and one with an indented hole of approximately 2.5 nm diameters. Our previous simulations on alkane surface[6,7] showed that structuring of the crystal surfaces enhances the surface free energy of hydration or, in other words, surface structuring enhances hydrophobicity. Experimental work,[1-5,8-9] shows a lower surface tension of water on perfluoro-n-eicosane crystals than on the n-eicosane crystals. In this manuscript we focus on the differences between the two different crystal chemistries in terms of hydrophobicity on the molecular level by qualitative arguments by molecular dynamics simulations.

The contact angle studies of water on the surface of glass vapor deposited with $C_{20}F_{42}$ crystal were done by Nishsino et al.[2] The dynamic contact angle of the water on this kind of surface was found to be 119^0, which corresponds to a surface free energy

of 6.7 mJ/m^2 when the -CF_3 surface groups have hexagonal closed alignment. This article claims that the value of the surface free energy is the lowest surface free energy of any solid.[2] This article shows the effect of surface geometry (hexagonal arrangement of the -CF_3 surface groups) along with the chemistry of the -CF_3 surface groups can enhance the super-hydrophobicity of a surface.

Molecular dynamics simulations of the structure and properties of monolayers of perfluorinated amphiphiles[3,4] show that the monolayer of the perfluoroalkane have chains which have very little tilt in the chains with respect to the horizontal surface.[3,4] The simulations by Shin et al[3,4] show the different transitions in terms of structural properties at different packing fractions and temperatures for monolayers of fluorinated amphiphiles. .

5.2 Computational details

5.2.1 Details of the surface structure

The crystal of n-eicosane molecules ($C_{20}H_{42}$) (one layer of 7×12 molecules) serves as the model of our hydrophobic surface. Crystallography of n-eicosane shows that it has a triclinic crystal structure.[10-16] The description of the model of our n-eicosane crystal has already been mentioned in our previous work.[6,7] The crystal structure of n-eicosane is triclinic[17-23] ($\alpha = 67.6^0, \beta = 83.9^0, \mathrm{c} = 2.544\ \mathrm{nm}, \mathrm{a} = \mathrm{b} = 0.5\ \mathrm{nm}$) and close to the experimental crystal ($\alpha = 68.2^0, \beta = 85.7^0, \mathrm{c} = 2.743\ \mathrm{nm}, \mathrm{a} = \mathrm{b} = 0.5\ \mathrm{nm}$). The perfluoro n-eicosane crystal has a monoclinic crystal structure ($\alpha = 89^0, \beta = 92^0, \gamma = 120^0, \mathrm{c} = 2.83\ \mathrm{nm}, \mathrm{a} = \mathrm{b} = 0.57\ \mathrm{nm}$).[17] There exists literatures to describe the potential parameters of the pefluoroalkanes for molecular simulations of classical and ab-initio type.[13-16] However most of the parameters are done to fit the heat of vaporization and density of perfluoro alkanes. The potential parameters by Cui et al.[13] predicts the vapor-liquid equilibria of perfluoroalkanes Simulations of quantum mechanical origin correctly map the torsional potentials of perfluoroalkanes.[14-18] The perfluoroalkane chains are stiffer and more helical in origin than the corresponding alkane chains.[14-18] The torsional potential energy of the central C-C-C-C bond of n-alkanes and perfluoro-n-alkanes are very different. In alkanes an absolute minimum in the torsional potential energy is found for a torsional angle of 180^0, corresponding to the trans conformer, and a relative minimum is found at 60^0,

corresponding to the gauche conformation. In case of perfluoroalkanes the occurrence of absolute minima are located at angle of 170^0 on both sides of the staggered form.

OPLS-AA potential parameters are chosen to model the perfluoro-n-eicosane and n-eicosane crystal and are reported in Table.5.1 and Table. 5.2. Additionally harmonic potentials were used between carbons of the same index (i.e. C_i - $C_i^{/}$, length = 0.497 nm (n-eicosane crystal) and length = 0.57 nm (Perfluoro-n-eicosane crystal)) and carbon one index apart (C_i - $C_{i+1}^{/}$, length = 0.89 nm (n-eicosane crystal) and length = 0.7 nm (Perfluoro-n-eicosane crystal)). The spring constants were chosen as 2000 kJ mol^{-1} $Å^{-2}$. These lengths were chosen to maintain crystal structure in constant pressure simulations. Figure 5.1 (a) and (b) shows the schematic of an alkane crystal and a perfluoroalkane crystal. Two different topographies were chosen for study: a planar crystal and a hexagonal hole (19 alkane chains shortenened by four carbon atoms).[6,7] Holes were created on both sides of the crystal separated by 2 nm in the y direction and 1 nm in the x direction to have better statistics. Measuring between carbon chain positions flanking the holes, the holes have a diameter of approximately 2.5 nm for an n-eicosane crystal and 2.85 nm for a perfluoro-n-eicosane crystal. To convert to the inner widths, the diameter of a CH_3/CF_3 group should be subtracted from these values in case of the hole. The total surface areas of the holes of the crystal are $\sim 2.5\times\pi\times 0.5+\pi\times 1.25^2\ \mathrm{nm}^2 = 8.9\ \mathrm{nm}^2$ and $\sim 2.85\times\pi\times 0.5+\pi\times 1.42^2\ \mathrm{nm}^2 = 10.9\ \mathrm{nm}^2$, respectively for the n-eicosane and perfluoro-n-eicosane. With the surface area of the crystal of $3.3\times 5.3\ \mathrm{nm}^2$ for the n-eicosane crystal and $3.9\times 5.9\ \mathrm{nm}^2$ for the perfluoro-n-eicosane, we therefore have a percentage of indented surface of 50% for the n-eicosane crystal and 47% for the perfluoro-n-eicosane crystal. The total surface area of the hole for the perfluoro-n-eicosane is 22% larger than for the n-eicosane crystal.

Table 5.1 Potential parameters for alkanes (OPLS-AA model).

atom	q(e)	σ(nm)	ε(kcal/mol)	ref
$C(H_4)$	-0.24	0.35	0.066	13
$C(H_3)$	-0.18	0.35	0.066	13
$C(H_2)$	-0.12	0.35	0.066	13
H(C)	+0.06	0.25	0.030	13

The bond length r_{CH} = 0.109 nm, r_{CC} = 0.153 nm, ∠CCH = ∠HCH = 109.5^0 (for C-CH_3), ∠HCH = 107.0^0 (where C is bonded to two other carbons) and ∠CCC = 112.0^0

Table 5.2 Potential parameters for Perfluoro-n-nalkanes (OPLS-AA model).

atom	q(e)	σ(nm)	ε(kcal/mol)	ref
$C(F_4)$	0.48	0.35	0.097	12
$C(F_3)$	0.36	0.35	0.066	12
$C(F_2)$	0.24	0.35	0.066	12
F(C)	-0.12	0.295	0.053	12

The bond length r_{CF} = 0.1332 nm, r_{CC} = 0.1529 nm, ∠CCF = 109.5^0, ∠FCF = 109.1^0 and ∠CCC = 112.70^0

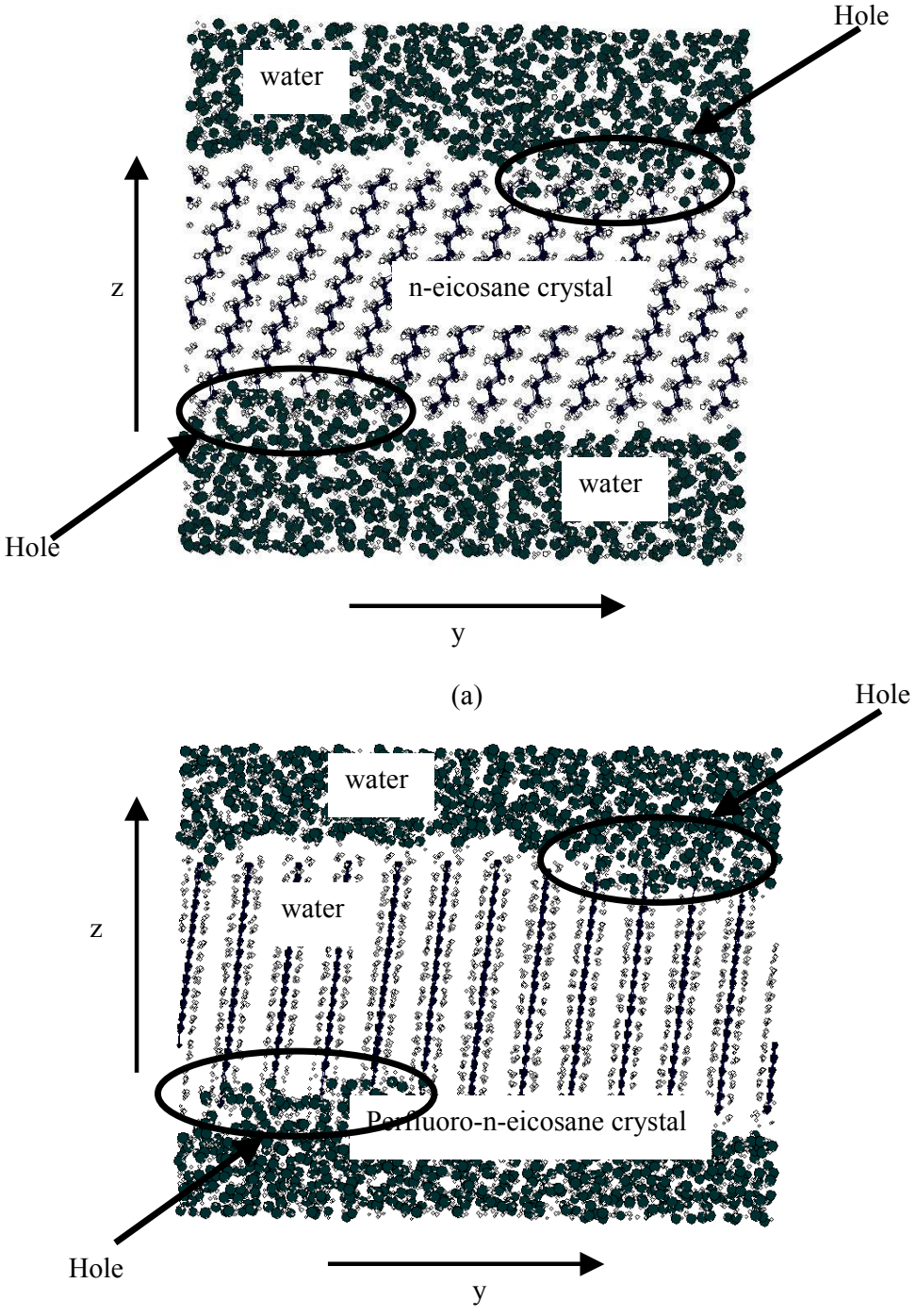

Figure 5.1 The system chosen for our MD simulation (a) n-eicosane crystal and (b) perfluoro-n-eicosane crystal.

5.2.2 Simulation model

The periodic simulation box contained 1500 molecules of water and 84 n-eicosane/perfluoro-n-eicosane molecules. The details of the setup procedure are discussed in reference 20. The crystal (thickness 2.5 nm) were separated from its periodic image by a water layer (thickness 2.6 nm). The perfluoro-n-eicosane crystal (thickness 2.8 nm) was also separated from its periodic image by a water layer (thickness = 2.0 nm). In all analyses, z = 0 refers to the surface of the planar crystal defined by the arithmetic mean of the z coordinates of all unindented surface carbons, so the hole carries a negative z.

We have used the YASP simulation package[24] for the molecular dynamics simulations. The system was weakly coupled to the desired temperature (298 K) with a relaxation time of 0.2 ps.[25-27] The Cartesian diagonal components of the pressure tensor were coupled separately to an external pressure of 0.1013 MPa with a relaxation time of 5 ps.[25-28] Bond lengths were constrained using the SHAKE algorithm.[29] The time step for the leapfrog integration scheme[25-28] was set to 0.002 ps and the trajectory frames were written to disk every 1 ps. The total simulation run is 2 ns with 1 ns each of equilibration and production. Non-bonded interactions were evaluated at every time step with a cutoff radius of 0.9 nm using a neighbour list (update every 20 steps, neighbour list cutoff 1.0 nm). Water is treated with the SPC/E model.[30] Lennard-Jones parameters for interactions between unlike atoms were evaluated using the Lorentz-Berthelot mixing rules,[26] electrostatic interactions were treated with the reaction field approximation,[25] using an effective dielectric constant of 72. As a test we have calculated the free energy of hydration for octane (-9.2 kJ/mol, experimental –9.87 kJ/mol) and perfluoro-n-heptane (-2.56 kJ/mol). There are no experimental values of solvation free energy of perfluoro-n-alkanes in water probably for the reason that they are extremely insoluble in water.

5.2.3 Analysis

The simulations were analysed in terms of the density of water at and near the interface. We have analysed the local densities by dividing the simulation box into cells ($0.4 \times 0.4 \times 0.2\,\mathrm{nm}^3$) and finding the density in each cell. Since the crystal is not space fixed and has the freedom to diffuse in x and y direction, the grid geometry is attached to the crystal in order to get consistent density distributions in the course of the MD simulations. The density distribution ($\mathrm{g/cm}^3$) is evaluated using

$$\rho(\vec{r}) = \frac{< N[\vec{r}, (x - \frac{\Delta x}{2}, x + \frac{\Delta x}{2}), (y - \frac{\Delta y}{2}, y + \frac{\Delta y}{2}), (z - \frac{\Delta z}{2}, z + \frac{\Delta z}{2})] > \mathrm{M_W}}{\Delta x \Delta y \Delta z}. \qquad (5.1)$$

where $\vec{r} = (x, y, z)$ is the centre of the cell, Δx, Δy, Δz are the length of the sides of the cell, M_w is the molecular weight of water and $< N[\vec{r}] >$, is the number of water oxygens inside the cell at $\vec{r}$ averaged over the 10^3 trajectory frames. The density distributions were converted to local chemical potentials by using Boltzmann inversion[31]

$$\Delta\mu(\vec{r}) = \text{-RT ln}\left(\frac{\rho(\vec{r})}{\rho_{Bulk}}\right). \qquad (5.2)$$

The bulk density of water ρ_{Bulk} away from the surface was calculated at the centre of the water layer, $\Delta\mu(\vec{r})$ is the difference of the chemical potential between position $\vec{r}$ and the bulk water chemical potential. For $\Delta\mu(\vec{r}) < 0$, position $\vec{r}$ is hydrophilic and if $\Delta\mu(\vec{r}) > 0$ it is hydrophobic.

5.3 RESULTS AND DISCUSSION

5.3.1 Density distribution of water near the two surface structures

The density distribution of water near the surface of the crystal indicates hydrophobicity of the crystal surface. A lower density of water at the interface signifies a higher hydrophobicity. The spatial density distribution of water with respect to the surface gives a first idea. Figure. 5.2 shows the density profile (equation 1) in a yz slab of thickness Δx = 0.5 nm positioned between x_1 = -0.25 nm and x_2 = 0.25 nm relative to the central reference carbon atom. This slab cuts vertically through the surface and the hole. The surface level is at z = 0 (methyl/trifluoro methyl carbons). The water density at the interface of the n-eicosane crystal is higher (Fig. 5.2(a) and (c)) than at the perfluoro-n-eicosane crystal (Fig. 5.2(b) and (d)) the water density maximum is shifted by 0.2 nm more towards the bulk in case of the perfluoro-n-eicosane crystal compared to the n-eicosane crystal. The shifting in the density distribution of water can be due to two possible effects:(1) the bigger size of the $–CF_3$ groups than the $–CH_3$ groups, or (2) the potential parameters in the simulation. In the $–CF_3$ group the individual atoms have higher absolute charges than in the $–CH_3$ groups, and the fluorine is negative whereas the hydrogen is a positive. In addition the

ordering of water near the n-eicosane crystal is higher than near the perfluoro-n-eicosane crystal. The orientational ordering of water is analysed in section 3.3. The water density is less at the edge walls of the holes, it avoids contacts with the edges of the surface structures. Figure. 5.2 shows the density averaged in the x and y direction as a function of z. Cells inside the crystal are excluded from the average. In all cases the water density approaches the bulk density of water ~ 0.98 g /cm^3 away from the crystal surface. Fig. 5.2(a) shows the density distribution of water near a planar crystal for both the n-eicosane and perfluoro-n-eicosane crystal. The water density maximum at z ~ 0.27 nm for n-eicosane crystal is shifted to z ~ 0.33 nm for the planar perfluoro n-eicosane crystal. At the same time, the initial rise in the density is less steep and the peak height decreases. The subsequent minimum shifts by the same amount. Fig. 5.2(b) shows the density distribution of water, for n-eicosane crystal and n-perfluoro-eicosane crystal with holes. The shift in the density distribution is also evident here. The water density inside the holes is approximately the same for both chemistries.

The density distributions were converted to chemical potential differences of water between interface and bulk water region by Boltzmann inversion, (Fig. 5.3) using equation (2). For the planar surfaces, Fig. 5.3(a), the minima at z~ 0.27 nm for n-eicosane and at z ~ 0.33 nm for perfluoro-n-eicosane, have an absolute difference of ~ 0.2 kT. There is a slight benefit for the water to be present at the interface of an n-eicosane crystal than a perfluoro-n-eicosane crystal. This also holds for the hole geometry.

5.3.2 Contacts between water and the surface carbon atoms of the crystal

The number of contacts the water makes with the surface atoms, can also be used to judge the hydrophobicity of an interface.[6,7] We have shown that the lower the number of contacts the higher is the hydrophobicity. A low number of contacts implies a low density of water at the interface and vice versa. The higher the number of contacts, the larger is the residual dispersive attraction between water and surface, and the lower is the hydrophobicity. In principle the same criteria applies here. However, owing to the different size of the -CH_3 and the –CF_3 groups and the different positions of the

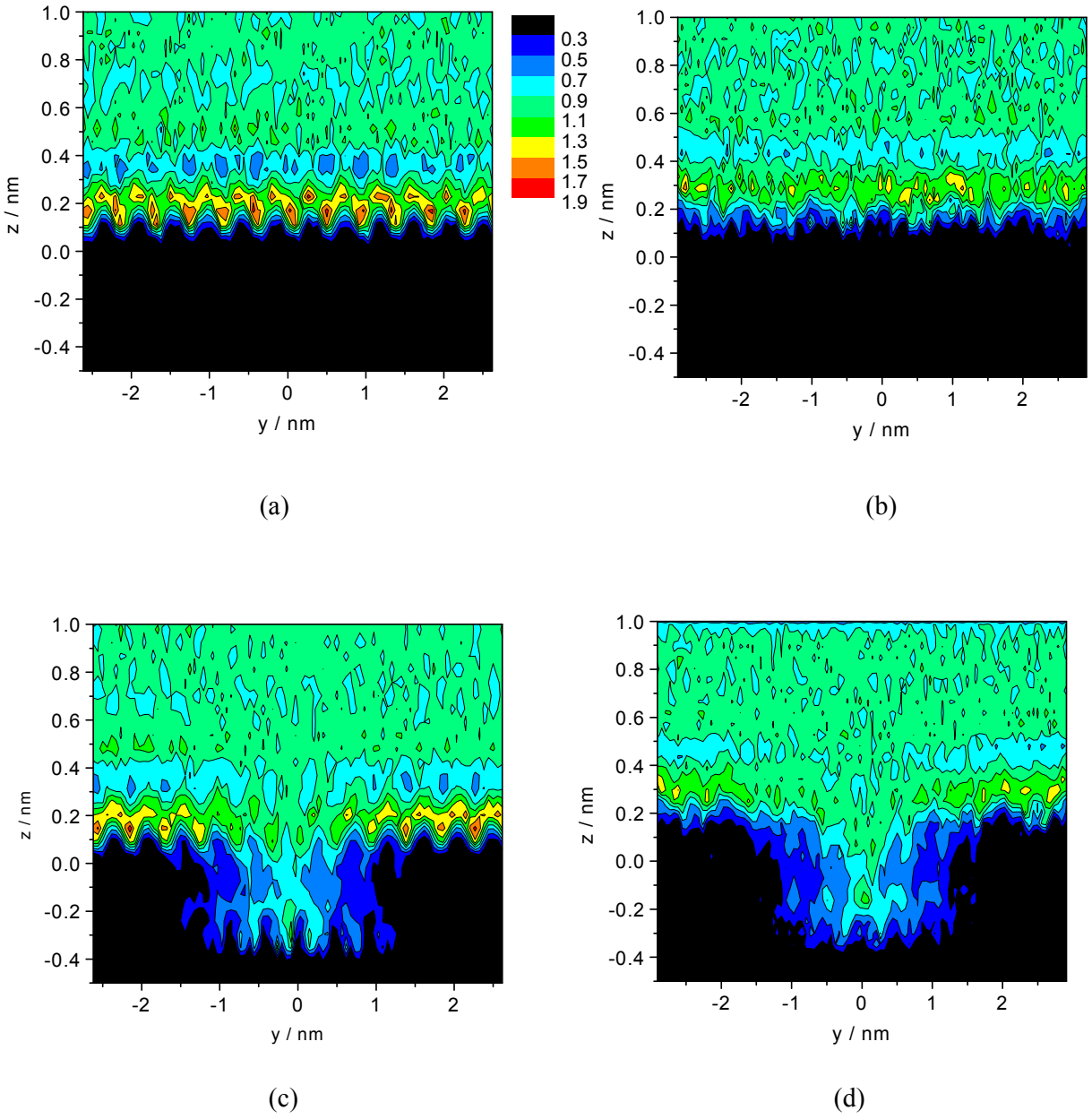

Figure 5.2 Water density (g/cm^3) in a vertical (yz) slab of thickness $\Delta x = 0.5$ nm cutting through the centre of the hole (a) Planar crystal (n-eicosane crystal) (b) Planar crystal (Perfluoro-n-eicosane crystal) (c) Hole (n-eicosane crystal) (d) Hole (Perfluoro-n-eicosane crystal).

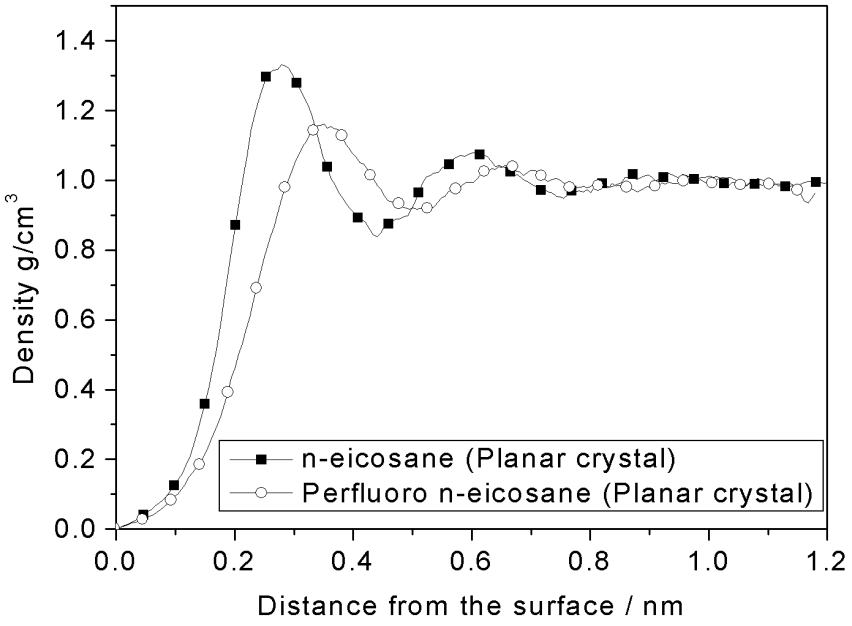

(a)

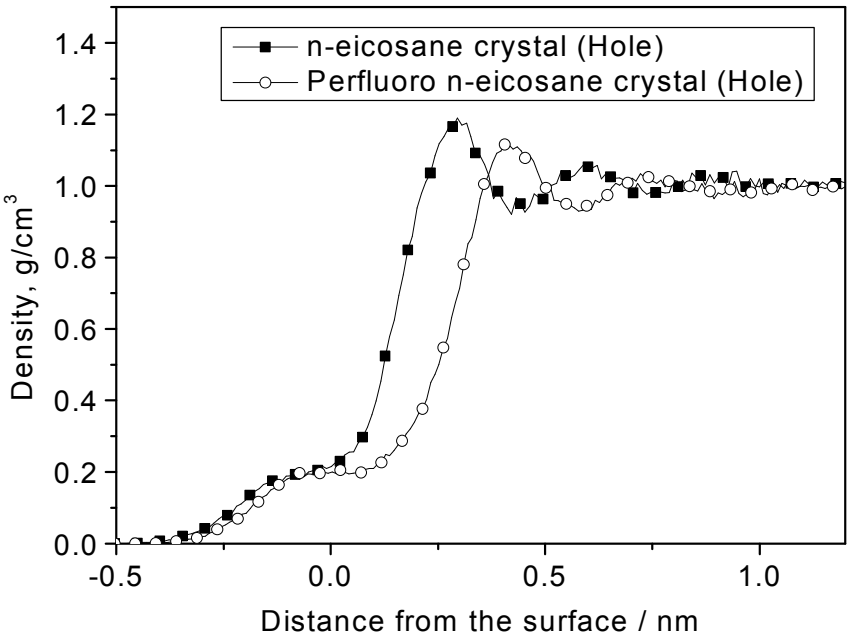

(b)

Figure. 5.3 Density of water (g/cm^3) as a function of z, the distance from the surface for an alkane crystal and a perfluoro-n-eicosane crystal. (a) planar crystal and (b) near a hexagonal hole.

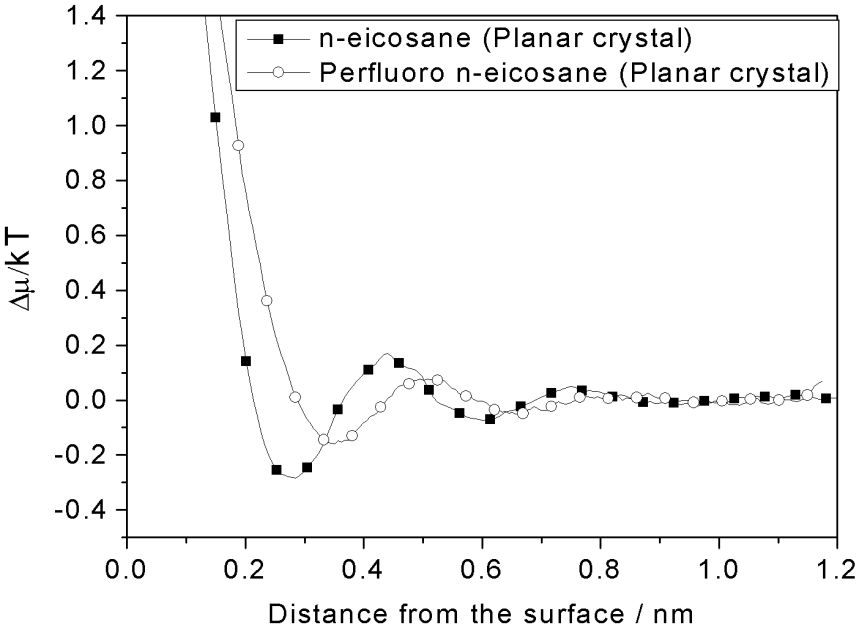

(a)

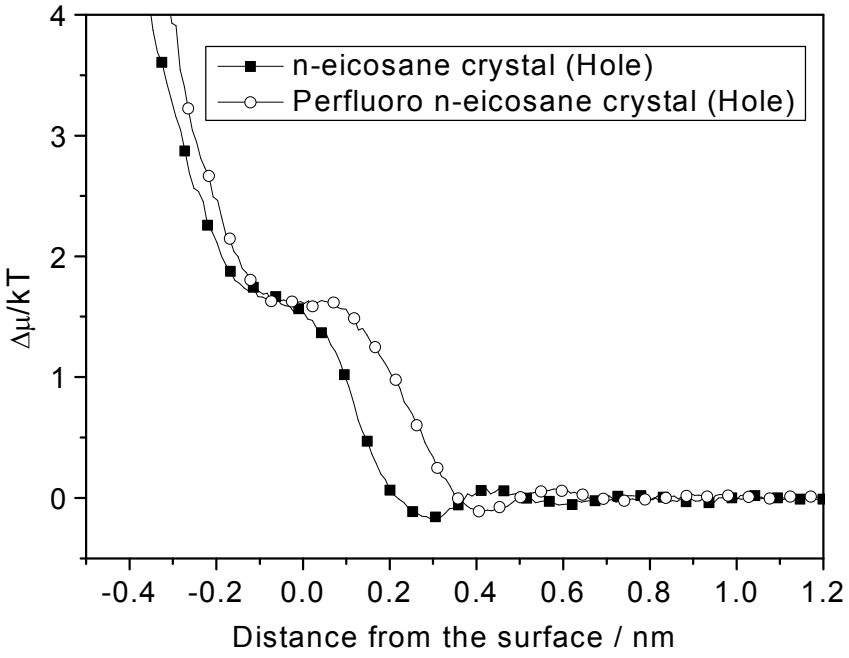

(b)

Figure.5.4 Difference of the water chemical potentials as s function of z, the distance from the surface for an alkane crystal and a perfluoro-n-eicosane crystal. (a) planar crystal and (b) near a hexagonal hole.

interface, it is difficult to compare the two different surface chemistries based on the number of water-carbon contacts. may not necessarily give the same correspondence between the number of surface contacts. The number of contacts evaluated form the radial distribution function (RDF) between water and all surface carbons.

As surface carbons we count all (perfluoro) methyl carbons at chain ends, as well as the three following (perfluoro) methylene carbons of the chains forming the sides of the holes. In case of the planar slab there are possible contacts between 168 surface carbons and water. For the holes there are contributions from 130 reference plane carbons, 108 side wall carbons 38 hole base carbons, considering both sides of the slab. From Fig 5.4(a) and (b) it is clear that the first peak of the RDF is shifted outwards ~ 0.07 nm in case of perfluoro-n-eicosane crystal compared to n-eicosane. The number of contacts, was obtained by integrating the first peak of the radial distribution function (0 to 0.5 nm or 0.57 nm, respectively), see Table 5.1. The number of contacts were normalized in two ways, per water molecule (water side) and per surface carbon atom (surface carbon side). The number of contacts in case of perfluoro-n-eicosane is calculated by integrating to r = 0.5 nm (similar to n-eicosane) crystal and to r = 0.57 nm to account for the shift of 0.07 nm of the radial distributions function towards larger distances. There is a systematic decrease of the number of contacts going from the planar to the structured surface. The magnitude of this decrease (~ 40%) is approximately the same for the alkane and the perfluoroalkane. This indicates that the effect of the nanostructure is generic and independent of the chemical identity of the surface, as long as it is hydrophobic.

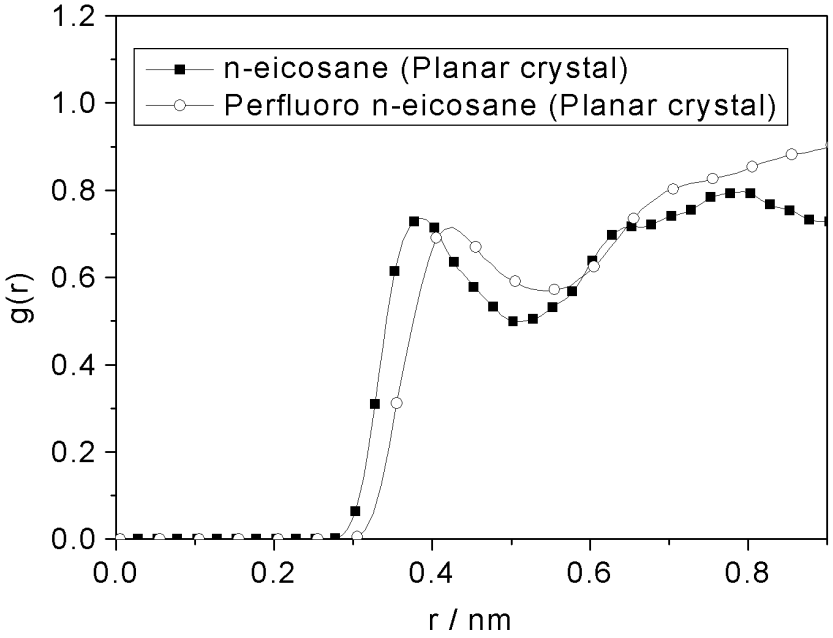

(a)

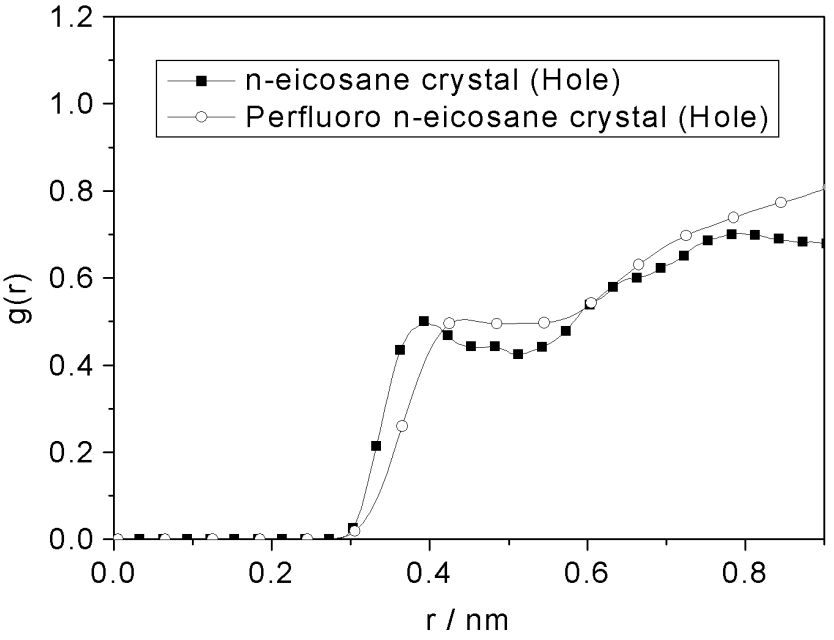

(b)

Figure 5.5 Radial distribution function g(r) between all surface carbons and water for an alkane crystal and a perfluoro-n-eicosane crystal (a) planar crystal and (b) near a hexagonal hole.

Table.5.3 Number of contacts between surface carbons and water per water molecule. In parentheses, the number of contacts per surface carbon atom is reported.

Crystal type	Planar crystal	Hole geometry
n-eicosane	0.45 (4.0)	0.27 (3.0)
Perfluoro-n-eicosane	0.36 (3.27) at r = 0.5 nm 0.42 (4.1) at r = 0.57 nm	0.21 (2.34) at r = 0.5 nm 0.23 (3.0) at r = 0.57 nm

5.3.3 Orientation of dipole moment vectors of water molecules

The lower positional order of water near a perfluoro-n-eicosane crystal compared to the n-eicosane crystal has been discussed in section 5.3.1. In this section we discuss the orientational order of the dipole moment vectors of water as function of distance from the surface. The orientational order is qualitatively related to entropy (order/disorder) of water at the interface. Stronger orientation signifies a lower entropy of water at the interface and vice versa. We define a vector pointing from the oxygen atom of the water molecule to the bisector of the line joining the two hydrogen atoms as the dipole moment vector. The orientation is then measured by an order parameter $\langle S^2 \rangle$ of the angle θ between the dipole moment vector and the surface normal.

$$\langle S^2 \rangle = 0.5 < 3\cos^2\theta - 1 >$$

A positive value of $\langle S^2 \rangle$ implies that the dipole moment vectors prefer to align perpendicular to the surface, it is negative when the preferred alignment is parallel to the surface. It is zero at the magic angle or for random orientations.

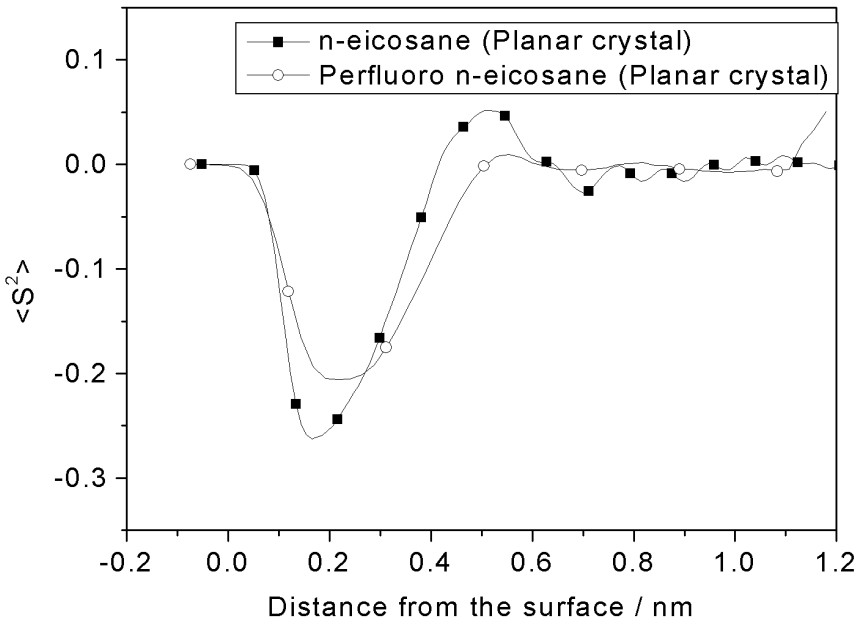

(a)

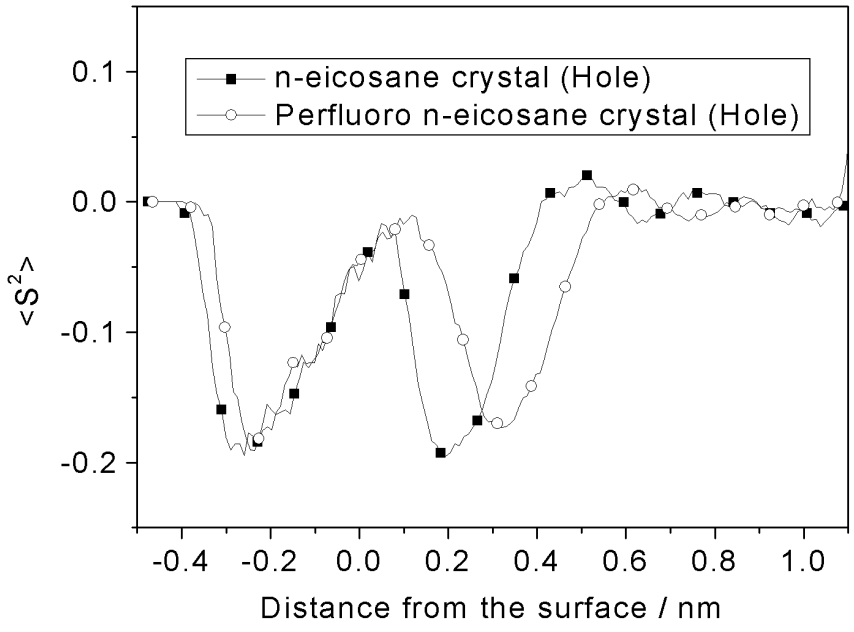

(b)

Figure.5.6 Orientation of water dipole moment vectors for an alkane crystal and a perfluoro-n-eicosane crystal. (a) planar crystal (b) near a hexagonal hole. The orientation is reported as the second Legendre polynomial $\langle S^2 \rangle$ of the cosine of the same angle.

The orientation of the dipole moment vectors for both geometries and both chemistries shows a preferential parallel orientation near the interface, which is a characteristic of hydrophobic surfaces,[32] Fig. 5.5. In the bulk region (> 0.6 nm) there is no preferred orientation for the water molecules. In case of the planar surface, Fig. 5.5(a), the single minimum is shifted outwards and shallower for perfluoro n-eicosane than for n-eicosane. In the hole case, Fig. 5.5(b), there is a double minimum structure at z = 0.3 nm (at the interface) and z = -0.2 nm inside the hexagonal hole (n-eicosane crystal) probably due to the competing influence of the hole walls. For the perfluoro-n-alkanes crystal with a hole, all features are shifted towards the bulk water region and are shallow compared to the hole n-eicosane case.

For both surface geometries, it is clear that the interface of the perfluoro-n-eicosane crystal-water has a higher entropy than the n-eicosane-water interface. Qualitatively, higher entropy should correspond to lower free energy or chemical potential of water at the interface for the perfluoro-n-eicosane crystal than the n-eicosane crystal. A lower free energy of water entails to a lower interfacial tension of this interface, which has been already proven to be true by experiments[2].

5.4 CONCLUSIONS

This article investigates how the hydrophobicity of a surface depends on the chemistry (alkane vs. perfluoroalkane) and the nanostructure (planar vs. nanometre-size indentations). All indicators, water density profiles, water orientation and the number of water-surface contacts, show that a perfluoroalkane surface is more hydrophobic than an alkane surface, no matter what the surface topography is. The terminal $–CF_3$ groups are large than the corresponding - CH_3 groups, which has three effects: Firstly, there are fewer of them per surface area, which reduces the possibility of interaction. Secondly, they are hydrated less, as the water molecules are kept farther away. This reduces the enthalpic contribution to the surface free energy. Thirdly, their repulsive potential is less steep, which reduces positional and orientational order of water molecules near the interface.

The effect of surface structure superpose over that of surface chemistry. For both alkane and perfluoroalkane surface, nano indentations increase the hydrophobicity. This is evident in water density and orientational ordering, but most noticeable in the number of water-surface contacts. Going from the planar to the indented interface, the

number of contacts is reduced by approximately 40% for both chemistries. While counting contacts is only a qualitative indicators, when one compares alkanes and perfluoroalkanes, as their molecular structure is too difficult to make them comparable, it certainly allows the comparison of different surface topographies realised with the same chemistry. The close correspondence between the number of contacts and the quantitative interfacial free energy has been shown in an earlier contribution.[5]

With a view to designing ever more hydrophobic surface the results present here have important consequences. Provided the base chemical, which constitutes the surface, is already sufficiently hydrophobic, the surface can be made even more hydrophobic by nano-structuring. The influence of nano-structuring is generic and independent from the chemistry. What matters are the size and shape of indentations or protrusions. Once they have been optimized (see. e.g. ref. 4), they may be transferred to another (hydrophobic) material.

References

(1) *CRC Handbook of Chemistry and Physics:* 74th edition, Boca Raton, **1993**.

(2) Nishino, T.; Meguro, M.; Nakamae, K.; Matsushita, M.; Ueda, Y. *Langmuir* **1999**, *15*, 4321.

(3) Collazo, N.; Shin, S.; Rice, S. A. *J. Chem. Phys.* **1992**, 96, 4735.

(4) Shin, S.; Collazo, N.; Rice, S. A. *J. Chem. Phys.* **1993**, 98, 3469.

(5) Mohammadi, R.; Wassink, J.; Amirfazli, A. *Langmuir* **2004**, 20, 9637.

(6) Pal, S.; Weiss, H.; Keller, H.; Müller-Plathe. F. *Langmuir*(Accepted).

(7) Pal, S.; Weiss, H.; Keller, H.; Müller-Plathe. F. Submitted to *ChemPhysChem*.

(8) Cassie, A. B. D.; Baxter, S. Trans of Faraday Society. **1944**, *40*, 546.

(9) Costa, Gomes, M. F.; Pádua, A. A. H. *J. Phys. Chem. B* **2003,** 107, 14020.

(10) Duffy, E. M.; Jorgensen; W. L. *J. Am. Chem. Soc*. **2000**, *122*, 2878.

(11) Kaminski, G.; Duffy, E. M.; Matsui, T.; Jorgensen, W. L. *J. Phys. Chem*. **1994**, *98*, 13077.

(12) Röthlisberger, U.; Laasonen, K.; Klein, M. L.; Sprik, M. *J. Chem. Phys*. **1996**, *104*, 3692.

(13) Cui, S. T.; Siepmann, J. I.; Cochran, H. D.; Cummings, P.T. *Fluid Phase Equilibria.* **1998**, *146*, 51.

(14) Song, W.; Rossky, P. J.; Maroncelli, M. *J. Chem. Phys.* **2003**, *119*, 9145.

(15) Kirkwood, J. G.; Buff, F. P. *J. Chem. Phys.* **1949**, *17*, 3.

(16) Blokhuis, E. M.; Bedaux, D.; Holcomb, C. D.; Zollweg, J. A. *Mol Phys.* **1995**. *85*, 3, 665.

(17) Nyburg, S. C.; Potworowski, J. K.; *Acta Cryst*. **1973**, *B29*, 347.

(18) Schwickert, H.; Strobl, G,; Kimmig, M. *J. Chem. Phys*. **1991**, 95, 2800.

(19) Borodin, O.; Smith, G. D.; Bedrov, D. *J. Phys. Chem.* **2002**, *106*, 9912.

(20) Watkins, E, W.; Jorgensen, W.L. *J. Phys. Chem. A* **2001**, 105, 4118.

(21) Jorgensen, W. L; Maxwell, D.S; Tivado-Rives,J. *J. Am.Chem. Soc*. **1996**, *118*,11225.

(22) Waheed, N.; Lavine, M. S.; Rutledge, G. C.; *J. Chem. Phys*. **2001**, *116*, 2301.

(23) Small, D. M.; The Physical Chemistry of Lipids: From Alkanes to *Phospholipids*; Plenum, New York, **1986**, 183.

(24) Müller-Plathe. F. *Comput. Phys. Commun*. **1993,** *78*, 77.

(25) Allen, M. P.; Tildesly, D. J. *Computer simulation of liquids*; Clarendon Press: Oxford, **1987**.

(26) Frenkel, D.; Smit, B. *Understanding Molecular Simulation*; Academic Press, San Diego, **2002**.

(27) Jensen, F.; *Introduction to Computational Chemistry*; Wiley VCH, Chichester, **1998**.

(28) Berendsen, H. J. C.; Postma, J. P. M.; van Gunsteren, W. F.; DiNola, A.; Haak, J. R. *J. Chem. Phys*. **1984**, *81*, 3684.

(29) Ryckaert, J. P.; Ciccotti, G.; Berendsen, H. J. C. *J. Comp. Phys*. **1971**, *23*, 237.

(30) Berendsen, H. J. C.; Grigera, J. R.; Straatsma, T. P. *J. Phys.Chem*. **1987**, *91*, 6269.

(31) Biermann, O.; Hädicke, E.; Koltzenburg, S.; Müller-Plathe. F. *Angew. Che Int. Ed.* **2001**, *113* , 3938.

(32) Daura, X.; Mark, A. E.; van Gunsteren, W. F. *J. Comp. Chem*. **1998**, 19, 535.

(33) Berendsen, H. J. C.; van, der Spoel, D.; van Drunen, R. *Comp. Phys. Commun.* **1995**, 91, 43.

(33) Grigera, J. R.; Kalko, S. G.; Fischbarg, J. *Langmuir*. **1996**, *12*, 154.

Summary

In this thesis, the water at the interface of a hydrophobic crystal surface has been investigated. The molecular dynamics method or "computer experiments" have been performed to investigate the influence of nanostructure on the hydrophobicity of a hydrophobic crystal surface. The primary aim of the thesis was to investigate whether the nano-structuring on the hydrophobic surface increases its hydrophobicity, as the micro-structuring of the paraffinic crystals on the surface of the lotus leaves is known to impart super-hydrophobicity (water repellency) to them. In this work the claim about super-hydrophobicity would be superfluous because the super-hydrophobicity is a term based on the contact angle measurements of water droplet on a hydrophobic surface and we have not attempted to calculate the contact angles directly in the thesis. To study droplets in molecular dynamics simulations, one would have to study bigger system sizes ranging up to micrometer length scale (infeasible in molecular simulations), to have a practical droplet on a surface moreover one should also consider the effect due to gravity to form a meaningful droplet on the surface. Experimental determination of contact angle measurements is an average of the receding and the advancing contact angles and contact angles vary with the site of measurement. However in our molecular dynamics simulations we have investigated the enhanced hydrophobicity of a surface structured crystal in terms of water structuring and clever free energy calculations.

The nano-structuring affects the density distribution of water at the interface of the water/hydrophobic crystal and is described in chapter two. The density of the water at the interface is an important property, which can decide the hydrophobicity of a crystal. The potential of mean force calculations show that a lower density of water at a given position relative to the density of bulk water, (1 g/cm^3), translates into a higher chemical potential of water relative to the bulk. A higher relative chemical potential of water at the interface of water/hydrophobic surface implies hydrophobicity. The density distribution of water also showed that the water molecules avoid the edges of the nano-structured surfaces. The number of contacts between water and the interfacial carbon atoms of the hydrophobic crystal showed a systematic decrease of the number of contacts between water oxygen and the surface

molecules of the crystal for different nanostructures. The different surface structures studied are triangular holes (~ 1.7 nm), hexagonal hole (~ 1.7 nm), stripes (~ 1.2 nm×∞), big hexagonal hole (~ 2.5 nm) and protrusion of size (~2.5 nm). Big hexagonal holes and protrusion show the maximum enhancement in the hydrophobicity. The number of contacts between water and the surface carbons was used as one of the tools to determine the enhancement in the hydrophobicity due to surface structuring. Crystal surface having the big hexagonal hole and the protrusion showed the maximum enhancement in the hydrophobicity.

Another important property, which determines hydrophobicity of a surface, is the surface free energy. The absolute free energy calculation of the water/hydrophobic surface, a solid/liquid interface, has complications and is discussed at the end of this chapter. The calculation of the difference in the interfacial free energies between a structured hydrophobic surface and a planar crystal (the reference state), by thermodynamic integration method, is however, possible and it is done on hexagonal hole and protrusion of similar size (~2.5 nm). It is found that surface structuring (hole or protrusion) increases the surface tension and hence the hydrophobicity. The correlation between the number of contacts between water and the surface carbons of the hydrophobic crystal was in good accordance with the interfacial free energy calculations. The calculations involving number of contacts and the free energy calculations showed a methodological result based on water-surface contacts (fewer contacts → less interactions → higher hydrophobicity).

The behaviour of aqueous salt solutions near a flat and a nano-structured hydrophobic surface was studied and analysed in chapter 3. The motivation was to study the interface of water-hydrophobic crystal under the influence of electrolyte salts. The distribution of the ions followed the pattern also found near the vacuum interface: Small anions (F^-) avoid the surface whereas large anions (I^-) prefer the surface. The cations (Na^+) adapt to the anion distribution. This finding is against the traditional view that electrolytes always stay away from the interface since they increase the water/hydrophobic surface tension. The increase in the surface tension/surface free energy per unit area of the water/water vapour interface in spite of the presence of the salt ions at the interface was also confirmed for the water/hydrophobic interface. The theory of preferential interactions is used to determine the change of the free energy of hydration of a solute due to the presence of

a cosolvent (salts). The conjecture that the presence of the I^- at the interface of the crystal/water interface might impart a residual negative charge to the interface turning it to be a hydrophilic crystal/water interface is proven to be wrong by the molecular dynamics simulations. The cumulative presence of the I^- and the Na^+ ions (as a double layer) imparts a slight enhancement in the surface tension of the crystal/water interface.

In chapter 5 we have studied the difference in hydrophobicity of a n-eicosane crystal and a perfluoro-n-eicosane crystal. The hydrophobicity is enhanced due to surface structuring and surface chemistry of the crystal. The molecular dynamics simulation of water at the interface of the perfluoro-n-eicosane crystal reveals not only the surface structuring enhances the hydrophobicity the hydrophobicity is also enhanced due to the chemistry of the crystal. The results in this chapter are mostly qualitative. The enhancement in the hydrophobicity of a perfluoro-n-eicosane crystal is discussed in terms of density distribution and the corresponding chemical potential of water as a function of distance from the surface. The lower density of water and a higher chemical potential of water at the interface shows an enhanced hydrophobicity at the interface. The number of contacts between water and surface carbons, which was successful, in deciding the hydrophobic nature/characteristic of an interface was not successful here, due to different surface geometries at the interface (refer chapter 5). A more quantitative treatment to discuss the comparison between the two different surface chemistries would require more sophisticated methods of finding surface free energies (with reliable error limits). The structuring of the dipole moment vectors reveal that the water molecules are more structured at the interface of the alkane crystal rather than at the interface of the perfluoro-n-alkane crystal which indicates that the water molecule has higher entropy at the interface of the perfluoro-n-alkane crystal than the alkane crystal. A higher entropy implies a lower surface free energy and a lower surface tension.

A systematic way to study absolute surface free energies of water/hydrophobic surface by molecular dynamics simulations is necessary. Note that there exist hardly any method, which could be used to study water/hydrophobic crystal surface free energies with acceptable error bars. The only method possible or has been employed in this past is the thermodynamic integration procedure, which in principle is possible however it suffers due to heavy error bars for system sizes of nanometre length scale. The complication regarding the calculation of absolute interfacial energies of

solid/liquid interfaces is the anisotropy of pressure inside the solids. The anisotropy of the pressure at the interface of the solid/liquid interface inhibits one to calculate the surface free energy by pressure anisotropy method, which is a common practice for liquid-liquid interfaces. Once the method of direct calculation of interfacial free energy of the solid/liquid interface is established there can be a direct comparison between experimental measurements and simulations regarding the water/hydrophobic surface free energy. Recently an interesting method termed as the moving wall method (already referenced in chapter two) has been in use to calculate the crystal/melt interface. It is interesting whether this method works for water/hydrophobic surface interface. Our group is actively working in this challenging project.

While it was not possible to calculate the absolute surface tension of the crystal/water interface in this thesis, however, we have investigated all other properties, which are indicators of enhanced hydrophobicity (relative surface tensions, contacts between water and surface carbons and the densities). All the properties support the fact that nano-structuring increases the hydrophobicity of an already hydrophobic surface.